

2006 SUMMER RESEARCH PROGRAM FOR HIGH SCHOOL JUNIORS
AT THE
UNIVERSITY OF ROCHESTER'S
LABORATORY FOR LASER ENERGETICS

STUDENT RESEARCH REPORTS

PROGRAM COORDINATOR

Dr. R. Stephen Craxton

March 2007

Lab Report 348

2006 SUMMER RESEARCH PROGRAM FOR HIGH SCHOOL JUNIORS

AT THE

UNIVERSITY OF ROCHESTER'S

LABORATORY FOR LASER ENERGETICS

STUDENT RESEARCH REPORTS

PROGRAM COORDINATOR

Dr. R. Stephen Craxton

LABORATORY FOR LASER ENERGETICS

University of Rochester

250 East River Road

Rochester, NY 14623-1299

During the summer of 2006, 13 students from Rochester-area high schools participated in the Laboratory for Laser Energetics' Summer High School Research Program. The goal of this program is to excite a group of high school students about careers in the areas of science and technology by exposing them to research in a state-of-the-art environment. Too often, students are exposed to "research" only through classroom laboratories, which have prescribed procedures and predictable results. In LLE's summer program, the students experience many of the trials, tribulations, and

rewards of scientific research. By participating in research in a real environment, the students often become more excited about careers in science and technology. In addition, LLE gains from the contributions of the many highly talented students who are attracted to the program.

The students spent most of their time working on their individual research projects with members of LLE's scientific staff. The projects were related to current research activities at LLE and covered a broad range of areas of interest including computational hydrodynamics modeling, materials science, laser-fusion diagnostic development, fiber optics, database development, computational chemistry, and the computational modeling of electron, neutron, and radiation transport. The students, their high schools, their LLE supervisors, and their project titles are listed in the table. Their written reports are collected in this volume.

The students attended weekly seminars on technical topics associated with LLE's research. Topics this year included laser physics, fusion, holographic optics, fiber optics, liquid crystals, atomic force microscopy, and the physics of music. The students also received safety training, learned how to give scientific presentations, and were introduced to LLE's resources, especially the computational facilities.

The program culminated on 30 August with the "High School Student Summer Research Symposium," at which the students presented the results of their research to an audience including parents, teachers, and LLE staff. Each student spoke for approximately ten minutes and answered questions. At the symposium the William D. Ryan Inspirational Teacher award was presented to Mr. Thomas Lewis, a former earth science teacher (currently retired) at Greece Arcadia High School. This annual award

honors a teacher, nominated by alumni of the LLE program, who has inspired outstanding students in the areas of science, mathematics, and technology. Mr. Lewis was nominated by Benjamin L. Schmitt, a participant in the 2003 Summer Program, with a letter co-signed by 13 other students.

A total of 204 high school students have participated in the program since it began in 1989. The students this year were selected from approximately 60 applicants. Each applicant submitted an essay describing their interests in science and technology, a copy of their transcript, and a letter of recommendation from a science or math teacher.

In the past, several participants of this program have gone on to become semifinalists and finalists in the prestigious, nationwide Intel Science Talent Search. This tradition of success continued this year with the selection of three students (Alexandra Cok, Zuzana Culakova, and Rui Wang) as among the 300 semifinalists nationwide in this competition. Wang was selected as a finalist—an honor bestowed upon only 40 of the 1700 participating students.

LLE plans to continue this program in future years. The program is strictly for students from Rochester-area high schools who have just completed their junior year. Applications are generally mailed out in early February with an application deadline near the end of March. Applications can also be obtained from the LLE website. For more information about the program, please contact Dr. R. Stephen Craxton at LLE.

This program was supported by the U.S. Department of Energy Office of Inertial Confinement Fusion under Cooperative Agreement No. DE-FC52-92SF19460.

High School Students and Projects (Summer 2006)			
Name	High School	Supervisor	Project Title
Deshpreet Bedi	Brighton	F. Marshall	X-Ray Diffraction Measurements of Laser-Generated Plasmas
Ryan Burakowski	Churchville-Chili	T. Kosc	PCLC Flakes for OMEGA Laser Applications
Alexandra Cok	Allendale Columbia	S. Craxton	Development of Polar Direct Drive Designs for Initial NIF Targets
Zuzana Culakova	Brighton	K. Marshall	Improved Laser Damage Resistance of Multi-Layer Diffraction Gratings Vapor-Treated with Organosilanes
Eric Dobson	Harley	J. Delettrez	Modeling Collisional Blooming and Straggling of the Electron Beam in the Fast-Ignition Scenario
Elizabeth Gregg	Naples Central	S. Mott/J. Zuegel	Fiber Optic Splice Optimization
Daniel Gresh	Wheatland-Chili	R. Kidder	Implementing a Knowledge Database for Scientific Control Systems
Matt Heavner	Fairport	C. Stoeckl	Realtime Focal Spot Characterization
Sean Lourette	Fairport	C. Stoeckl	Neutron Transport Calculations Using Monte-Carlo Methods
Ben Matthews	York Central	D. Lonobile/ G. Brent	Precision Flash Lamp Current Measurement—Thermal Sensitivity and Analytic Compensation Techniques
Ryan Menezes	Webster Schroeder	D. Harding	Evaluation of Confocal Microscopy for Measurement of the Roughness of Deuterium Ice
Rui Wang	Fairport	K. Marshall	Computational Modeling of Spectral Properties of Nickel Dithiolene Dyes
Nicholas Whiting	Bloomfield	R. Epstein	Dynamic Energy Grouping in Multigroup Radiation Transport Calculations

X-Ray Diffraction Measurements of Laser-Generated Plasmas

Deshpreet Bedi

X-ray Diffraction Measurements of Laser-Generated Plasmas

Deshpreet Singh Bedi
University of Rochester, Laboratory for Laser Energetics
2006 Summer High School Program

ABSTRACT

Plasmas generated by the implosion of targets by the OMEGA laser emit x rays. Diffraction gratings can spatially separate the different wavelengths of these x rays. Measurement of the resultant space-resolved, continuum x-ray emission spectrum can provide valuable information regarding the properties of the plasma, such as core temperature, surface flux density, and source size.

The plasma, however, has a spatial distribution which blurs the diffracted spectrum, especially near the high energy end. This blurring can be described by a mathematical operation called a convolution. To accurately measure parameters of the plasma in the presence of spatial blurring, the effect on the grating-dispersed spectrum must be taken into account. The method used in this work is to take a spectral shape such as an exponential, a shape expected from a hot plasma, or the spectrum predicted by simulation, include the instrument efficiency, and compute the grating-dispersed spectrum. This is then convolved with a Gaussian spatial distribution, producing a mathematical model of the observed spectrum. A best fit of this model to the measurements yields estimates of the plasma parameters.

INTRODUCTION

The OMEGA laser facility¹ at the University of Rochester's Laboratory for Laser Energetics is currently being used to pursue the goal of obtaining thermonuclear ignition in the laboratory. Thermonuclear ignition requires both high temperature (≥ 10 keV) and high density (≥ 100 g/cm³) conditions to exist in the plasma. The OMEGA laser facility is used to approach

these conditions, through the implosions of targets such as cryogenic deuterium-tritium (DT)-filled shells.² These shells become plasmas with central temperatures and densities comparable to those existing in the sun's interior (the sun's interior has a temperature of ~ 1.4 keV and a density of ~ 150 g/cm³).³ In the laser-generated plasma, the goal is to achieve much higher temperatures with more highly reactive fuel (DT) since, unlike the sun, the laboratory plasma exists in the hot dense phase for only about 10^{-10} seconds before expanding rapidly. In contrast, the sun is believed to burn its fuel for billions of years ($\sim 10^{17}$ sec).

The imploded interiors of the plasmas emit x rays.⁴ X rays range from wavelengths of 100 Å (soft) to 0.01 Å (hard) ($1 \text{ Å} = 10^{-10} \text{ m}$).⁵ X rays emitted from the core plasma are differentially absorbed by the cooler surrounding shell of plasma, with absorption a strong function of energy.⁴ The soft x rays are absorbed more strongly than the hard x rays. The x rays are imaged by a Kirkpatrick-Baez (KB) microscope⁶ in the experiments reported here. The x rays also pass through a diffraction grating, made at LLE by a process including photolithography and reactive ion etching.⁷ The emitted x rays are dispersed by wavelength upon passing through the diffraction grating. The diffracted images are recorded either by the time-integrated exposure of Kodak Biomax-MS film or by the absorption of photons by a solid-state, charge-injection device (CID).⁸ Measuring the resultant broadband continuum spectrum provides information about the compressed shell temperature and the areal density of the plasma.⁴

The finite size of the laser-generated plasma results in a spectrum of x rays after diffraction that is not completely separated by wavelength and is blurred by the spatial distribution of the source [Fig. 8(a)]. In this report, a method of accounting for the effect of spatial blurring on the determination of the plasma emission spectrum is described, the goal

being to accurately model the diffracted x-ray spectrum in order to best measure the plasma size, temperature, and density in the presence of this blurring.

METHOD

A. X ray Emission

X rays are produced when any electrically charged particle of sufficient kinetic energy decelerates. In the laboratory, x rays are produced by accelerating electrons emitted by a hot filament towards a metal target (anode).⁹ When the electrons strike the anode, they eject inner shell electrons off the anode, leaving a vacancy. These vacancies are filled by subsequent electron transitions from higher shells to lower ones, which result in the emission of x rays. The energy of these emitted x rays is characteristic of the electron transitions, which are dependent on the anode metal.

The x rays emitted from the anode have been found to consist of a mixture of different wavelengths, creating a continuous radiation, or Bremsstrahlung. This continuous spectrum results from the fact that not every electron decelerates in the same way. Some release all their energy at once, with one impact when they encounter the atoms of the metal target, while others deflect randomly many times, losing a fraction of their energy each time. When the voltage across the electrodes is raised above a certain level characteristic of the metal target, however, the characteristic line emission described above is observed superimposed on the continuous spectrum. Where large amounts of continuous radiation are desired in the laboratory, a heavy metal like tungsten and as high a voltage as possible should be used.¹⁰

B. Diffraction Gratings and Dispersion

At its simplest, diffraction involves a monochromatic beam of electromagnetic radiation (i.e. light) emitted from a point source encountering a single slit. Light is composed of wave

fronts of certain wavelength, which, upon impinging on the slit, emanate from each point in the slit as if they were point sources. The result of diffraction is an interference pattern, or a cyclic distribution of bright and dark spots. Bright spots result where the wave fronts arrive in phase, while dark spots result where the wave fronts arrive 180° out of phase. Increasing the number of slits sharpens the principal maxima (bright spots).

An increased number of slits also increases dispersion when dealing with radiation of many different wavelengths. Diffraction gratings are used to disperse light by wavelength and x rays are no exception. The diffraction gratings used at LLE are transmission gratings with 5000 lines/mm (Fig. 1) and are exactly like those designed for the Chandra X-Ray Observatory⁷ having been built at the same facility. The gold bars are nearly opaque to radiation, so principally the x rays that pass between the bars will be transmitted and diffracted.

The dispersion of x rays by wavelength is given by the grating equation¹¹

$$n\lambda = d_g \sin \theta, \quad (1)$$

where n is the diffraction order number, λ is the wavelength, d_g is the grating spacing, and θ is the diffraction angle. Because the x-ray emission from a laser-generated plasma source is not composed of just one wavelength and because the plasma is not a point source (i.e. it has a spatial distribution), there are no distinct peaks of maximum intensities at the various orders of diffraction. Rather, there is a continuum spectrum of all the x-ray wavelengths emitted from the plasma source [Fig. 8(a)]. There is also a zeroth-order image, which consists of undiffracted x rays, but in this study, only the first orders of diffraction (on either side of the zeroth-order image) are considered. Since diffraction angles are small,

$$\sin \theta \approx \frac{x}{D_i} \quad (2)$$

where x is the distance from the zeroth order image and D_i is the distance from the grating to the image plane (Fig. 2).

Substituting for $\sin\theta$ in the grating equation produces an equation relating position along the image plane (the x direction of Fig. 8) to the wavelengths of the diffracted x rays,

$$\lambda \approx \left(\frac{d_g}{D_i} \right) x \quad (3)$$

where d_g/D_i is the dispersion power of the grating ($\text{\AA}/\text{mm}$). The lower this value is, the more dispersed the diffracted spectrum is. For this study, the dispersion power is $0.9404 \text{ \AA}/\text{mm}$.

C. X-ray emission from a Plasma

X-ray emission from a plasma—whether a celestial source such as a supernova remnant¹² or the core of a laser-imploded shell target—differs from x-ray emission from the bombardment of a metal target with electrons. The emission from a hot, dense plasma has a spectrum that depends on the temperature of the plasma. Radiation from a plasma can be classified as continuous radiation, or Bremsstrahlung.¹³ A model of this radiation spectrum is given by an exponential,

$$\frac{ds}{dE} = j_o \exp\left(-\frac{E}{kT}\right), \quad (4)$$

where ds/dE is the surface emissivity of the target in $\text{keV}/\text{keV}/\text{cm}^2$, j_o is the surface energy flux density in $\text{keV}/\text{keV}/\text{cm}^2$, E is the energy of the x rays in keV, and kT is the core temperature of the target in keV.¹³

Since the KB microscope is used to obtain a magnified image of a portion of the laser-target emission, ds/dE is related to the flux detected at the image plane (df/dE) by⁴

$$\frac{df}{dE} = \frac{ds}{dE} \frac{\Delta\Omega}{4\pi} \frac{\varepsilon}{M^2}, \quad (5)$$

where $\Delta\Omega$ is the solid angle subtended by the microscope [equal to the cross-sectional area of the image detector divided by the square of the distance between the source and the detector], M is the magnification of the image (given by $M=D_i/D_s$), and ε is the throughput efficiency of the total system (a function of energy), given by,

$$\varepsilon(E) = \varepsilon_g(E) T_f(E) \quad (6a)$$

$$T_f(E) = e^{-\mu(E)\rho\Delta x}, \quad (6b)$$

where ε_g is the grating efficiency, T_f is the filter throughput efficiency, μ is the mass absorption coefficient of the filter in cm^2/g , ρ is the filter density in g/cm^3 , and Δx is the thickness in cm of the filter, typically composed of beryllium.

What is observed after dispersion by the grating (but before consideration of the spatial distribution of the plasma), however, is a spectrum varying with respect to position—the differential dispersed flux df/dx , a measurement of fluence values with respect to position on the spectrum. Df/dE is related to df/dx through multiplication with the differential dE/dx . By using the relationship $E=hc/\lambda$ in Eq. (3) and differentiating both sides, it is found that

$$\frac{dE}{dx} = -\frac{E^2}{hc} \frac{d_g}{D_i}, \quad (7)$$

the negative sign arising from the fact that increasing energy is in the direction of decreasing position (i.e. dispersion distance). Finally, the observed differential dispersed flux df/dx can be related to the target surface flux density ds/dE with the relationship

$$\frac{df}{dx} = -\frac{ds}{dE} \frac{E^2}{hc} \frac{d_g}{D_i} \frac{\Delta\Omega}{4\pi} \frac{\varepsilon}{M^2}. \quad (8)$$

Because of the limited resolution of the imaging device, however, the flux df (keV/cm²) cannot be measured for an infinitesimal length dx ; flux detectors at the image plane have finite-sized bins (pixels) into which all the flux in that area is added together. What is inferred as the dispersed spectrum from a point source (i.e. before taking into account the spatial distribution of the plasma source) is df , which is Eq. (8) multiplied by dx , which can be expressed as a finite length, Δx .

D. Convolution of Space and Spectrum

The laser-generated plasma, which emits x rays, is not a point source. X rays passing through the diffraction grating are blurred spatially. The dispersed image is spectrally blurred, resulting in an averaging of fluence values in space. This blurring can be described by a mathematical operation called a convolution. The convolution of two-dimensional functions is given by

$$C(x, y) = g(x', y') \otimes h(x, x', y, y') = \int_{space} g(x', y') h(x - x', y - y') dx' dy' \quad (9),$$

and can be described as an integral of a product of shifted copies of one function (h) with another (g).

The observed dispersed spectrum is a convolution of space and spectrum, where the spectrum is shifted and weighted by the values of a spatial distribution. This observed dispersed spectrum can be modeled by applying the convolution operation to the ideal exponential spectrum, df , with a normalized Gaussian source distribution (total area is 1) given by

$$g(x, y) = \frac{1}{\pi\sigma^2} e^{-(x^2+y^2)/\sigma^2}, \quad (10)$$

where σ is the standard deviation and calculated as ~ 0.6 times the full width at half maximum of the measured spectrum (allowing for the calculation of meaningful physical sizes for the spectrum and Gaussian distribution in relation to each other).

CALCULATIONS

The programming language PV-WAVE¹⁴ was used to facilitate the modeling of a dispersed convolution. First, the program *xray_spec* was written to generate a simple model exponential spectrum df before consideration of the spatial blurring of the plasma. A sample computed dispersed spectrum is shown in Fig. 3 for selected values of source temperature, kT , and surface energy flux density, j_0 [see Eq. (4)].

When the efficiency response of the diffraction grating and the filter transmission are included, the fluence values are reduced and features are added to the calculated flux density spectrum (Fig. 4), due to energy-dependent factors. Low-energy x rays (less than 2 keV, corresponding to dispersion positions greater than 6.6 mm on Figs. 3 and 4) were practically removed from the spectrum because of absorption in the beryllium filters (127 μm thick filter in this computation). The feature at 6 mm (corresponding to 2.2 keV) is due to a decrease in the diffraction efficiency of the gold bars in the diffraction grating.⁴

The program *gauss_gen* is used to generate a normalized two-dimensional Gaussian distribution [Eq. (10)], which is used to represent the spatial distribution of the plasma. Both the spectrum and Gaussian distribution are calculated on the same scale, corresponding to images with pixels of size 20 μm . This allows for an accurate convolution and dispersed spectrum that can be readily compared to grating dispersed images recorded on film. By entering a standard

deviation value σ as a parameter, a two-dimensional Gaussian of appropriate size is generated.

A lineout through the central pixel row of any of the convolved spectra, when compared to the point-source spectrum, shows the effects of convolution. The fluence values from a finite-sized plasma source are much lower than those from a point source (Fig. 5a), due to the fact that the blurring due to the spatial distribution has spread the energy flux density contained in one pixel over a width of many pixels. Adding up the values of fluence in a one-pixel-wide cross-section of the dispersed spectrum yields a result nearly equal to the fluence of the point-source spectrum at that same position. The minor loss can be accounted for by the spectral (horizontal) blurring (i.e. mixing of x rays of different energies). When compared on a normalized scale, it is clear that the features in the point-source spectrum due to the instrument responses have been blurred out, and the high-energy values (greater than 5 keV, corresponding to positions less than 2.6 mm) are greatly affected by the finite source size of the plasma (Fig. 5b).

MODELING OF EXPERIMENTAL SPECTRA

The spectra of dispersed x rays from two different cryogenic target implosions were modeled. Graphs of the spectral fluence (Figs. 6 and 7), $dE/d(h\nu)$ (ds/dE integrated over space), as a function of energy for OMEGA laser shots 44182 and 44602 allow for a straight line fit (in a semi-log plot) of a simple exponential to the measured data to be determined. The slope of the line is related to the source temperature, kT , by the relationship

$$kT = \frac{-(E_1 - E_2)}{\ln(I_1/I_2)} \quad , \quad (11)$$

where I_1 and I_2 are values of intensities in keV/keV at the energies E_1 and E_2 , respectively. I_0 , the surface intensity, is determined algebraically once kT is known. Division by the pixel area (in cm^2) gives j_0 , allowing for the calculation of space-resolved fluence. Each graph also contains

the LILAC-hydrocode-simulation predicted emission spectrum,² which takes into account absorption of the emitted lower-energy x rays by the cold outer fuel shell of the imploded plasma.

The dispersed x-ray spectra were computed using Eq. (8) from the surface fluence spectra for both the best-fit ideal exponential and the LILAC simulation, using a value of 3.63×10^{-9} steradians for the solid angle subtended by the microscope, 14.4 for the magnification, 0.9404 Å/mm for the dispersion constant, and 0.02 mm for the pixel size. Because the measured diffracted x-ray spectra are recorded on film, the spectra are measured in film density and have additional features due to the energy-dependent sensitivity of the film. In order to allow for the close approximation of the calculated spectra with the measured film spectrum, df was converted from units of keV/cm² to units of photons/μm², by dividing by the photon energy values (keV) and multiplying by 10^{-8} cm²/μm². A more exact treatment will need to take into account the exact dependence of film density on x-ray exposure.^{15,16}

In order to approximate the source size of the plasma used in calculating a Gaussian spatial distribution, a measurement of the full width at half maximum (FWHM) of the measured spectrum was made using PV-WAVE by creating a line-out through the width of the spectrum. A FWHM of 50 μm was measured, and using Eq. 10 a standard deviation of 30 μm was calculated for the Gaussian. The calculated spectra were then convolved with the 2-dimensional Gaussian using the CONVOL function in PV-WAVE.

For OMEGA shot 44182 (Fig. 8), both the ideal exponential and the LILAC spectrum show a dispersed spectrum with similar shape and size to that of the measured film-imaged spectrum. Though the ideal exponential did not take into account absorption of x rays below ~ 2 keV in the plasma and the LILAC simulation did, the two calculated spectra are almost identical,

due to the absorption of low-energy x rays by the beryllium filters. Both models, however, assume more absorption than what was measured, shown by the premature trailing off of the spectra in the direction of increasing x (i.e. decreasing energy).

For OMEGA shot 44602 (Fig. 9), while the ideal exponential still shows a similar shape and size to that of the measured spectrum, the LILAC simulation shows many differences. It calculates much more absorption than what was measured, and it assumed a hotter temperature for the plasma source, as seen by the closer proximity of the high-energy ends of the spectrum to the middle. This was to be expected, as the slope of the LILAC simulation in Fig. 7 deviated from the slope of the actual measurements and the ideal exponential.

CONCLUSION

Implosions of cryogenic fusion targets are diagnosed with a diagnostic that measures the spectrum of x rays from the hot, imploded core. Interpretation of the image data is complicated because it is affected by the spatial distribution of the x-ray emitting region. Accounting for the convolution of space and spectrum in the diffraction of x rays due to the plasma source not being a point source is important because the slope of the spectral fluence values is affected by the spatial distribution of the plasma, which affects the estimate of kT . In this investigation, a method for accurately modeling a measured x-ray spectrum has been introduced. Being able to model the spatially-dispersed spectrum allows for a minimization of differences between the measured and calculated spectra, enabling more accurate estimation of the plasma's core temperature and source size. Future work will improve on this optimization by converting the model spectra into film density so that the differences between the model and measured spectra are only due to the differences in plasma parameter values.

ACKNOWLEDGEMENTS

I would like to thank my advisor Dr. Frederick J. Marshall for all of his help, guidance, and support throughout this project. I would also like to thank Dr. Stephen Craxton for welcoming me into this program and the LLE staff for creating such a hospitable environment.

REFERENCES

1. T. R. Boehly, D. L. Brown, R. S. Craxton *et al.*, *Opt. Commun.* **133**, 495 (1997).
2. F. J. Marshall *et al.*, *Phys. Plasmas*, **12**, 056302 (2005).
3. Cox, Arthur N., Allen's Astrophysical Quantities (Fourth Edition). (The Estate of C.W. Allen/Springer-Verlag New York, Inc.: New York, NY, 2000), pp. 342.
4. F. J. Marshall *et al.*, "Diagnosis of laser-target implosions by space-resolved continuum absorption x-ray spectroscopy," *Phys. Rev.* **49**, 49 (1994).
5. Cullity, B. D., Elements of X-Ray Diffraction (Third Edition). (Prentice-Hall, Inc.: Upper Saddle River, NJ, 2001), pp. 1-3.
6. P. Kirkpatrick and A. Baez, *J. Opt. Soc. Am.* **38**, 766 (1948).
7. C. R. Canizares *et al.*, "The High Energy Transmission Grating Spectrometer for AXAF," *SPIE: X-Ray Instrumentation in Astronomy* **597**, 253 (1985).
8. F. J. Marshall *et al.*, "Imaging of laser-plasma x-ray emission with charge-injection devices," *Rev. Sci. Instrum.* **72**, 713 (2001).
9. Cullity, *ibid.*, pp. 4-19.
10. Cullity, *ibid.*, pp. 5-7.
11. Halliday, D. and R. Resnick, Fundamentals of Physics. (John Wiley and sons: New York, NY, 1970), pp. 744-746.
12. K. A. Flanagan *et al.*, "CHANDRA high-resolution x-ray spectrum of supernova remnant 1E 0102.2-7219," *The Astrophysical Journal* **605**, 230 (2004).
13. Lang, K. R., Astrophysical Formulae, Volume 1: Radiation, Gas Processes and High Energy Astrophysics. (Springer-Verlag: New York, NY, 1999), pp. 48-49.
14. Visual Numerics, Inc. Houston, TX 77042
15. F. J. Marshall *et al.*, "Absolute calibration of Kodak Biomax-MS film response to x rays in the 1.5- to 8-keV energy range," *Rev. Sci. Instrum.* **77**, 10F308 (2006).
16. J. P. Knauer *et al.*, *Rev. Sci. Instrum.* **77**, 10F331 (2006).

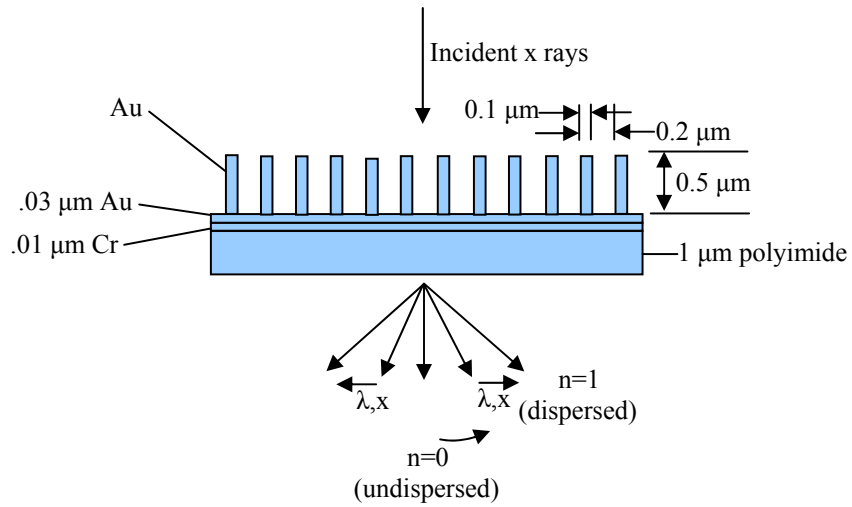


Fig. 1. Diagram of a transmission diffraction grating, showing undispersed ($n=0$) and dispersed ($n=1$) orders in the x direction.

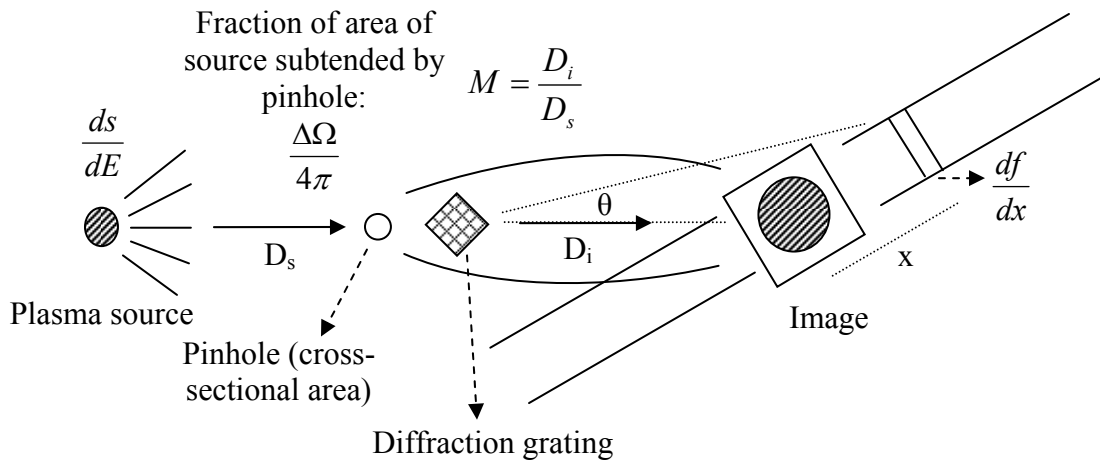


Fig. 2. Diagram of the imaging and diffraction of x rays emitted from a spatially-distributed plasma source. The image plane, shown schematically here, is perpendicular to the direction of x-ray propagation. For simplicity, the image is shown here as being formed by a pinhole rather than the functionally similar x-ray mirrors used by the KB microscope.

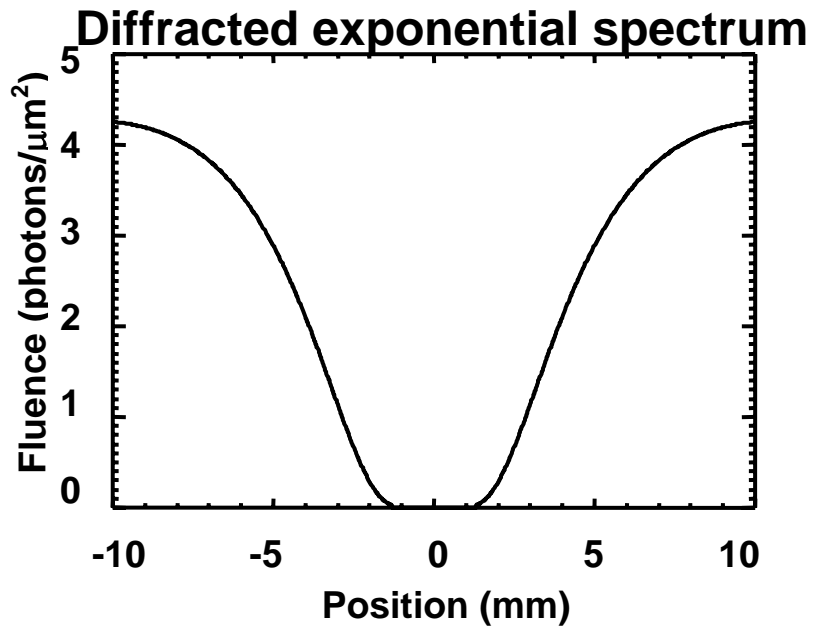


Fig. 3. An example of a dispersed exponential spectrum before consideration of the spatial blurring of the plasma. Position corresponds to the x direction of Fig. 8.

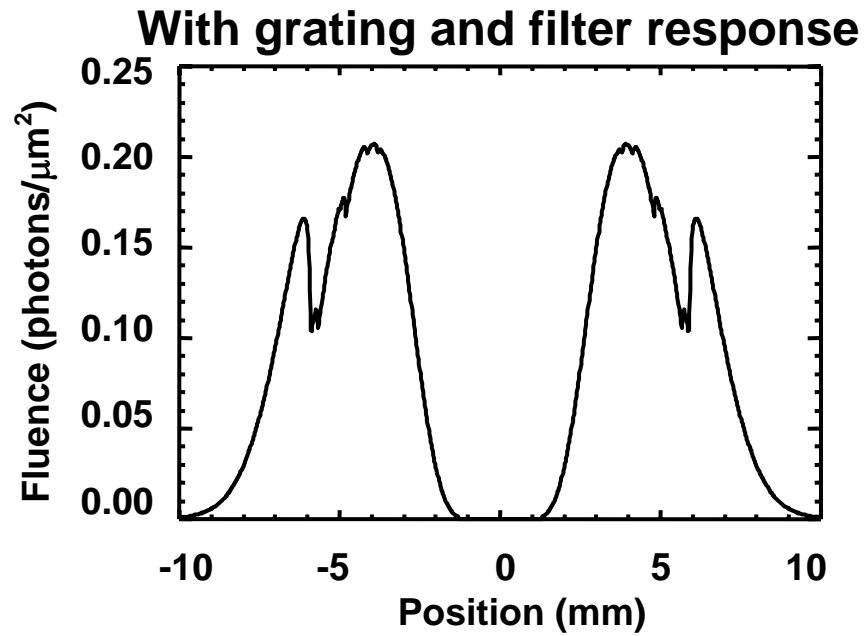


Fig. 4. The dispersed exponential spectrum of Fig. 3 after the addition of the efficiency response of the diffraction grating and the filter transmission.

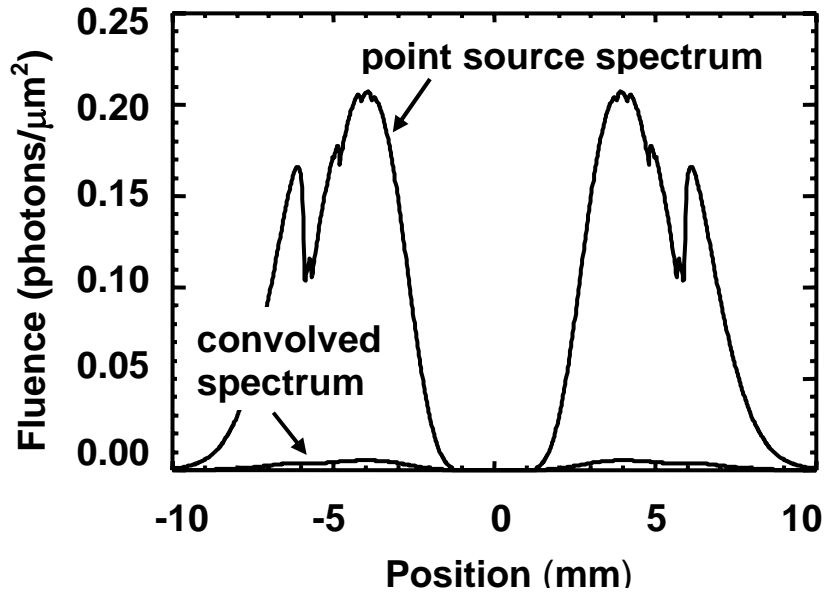


Fig. 5a. Comparison of the dispersed exponential spectra before and after consideration of the source's spatial distribution. The effect of having a finite-sized plasma source is to greatly reduce the fluence values contained in a line-out through the center row of the spectrum.

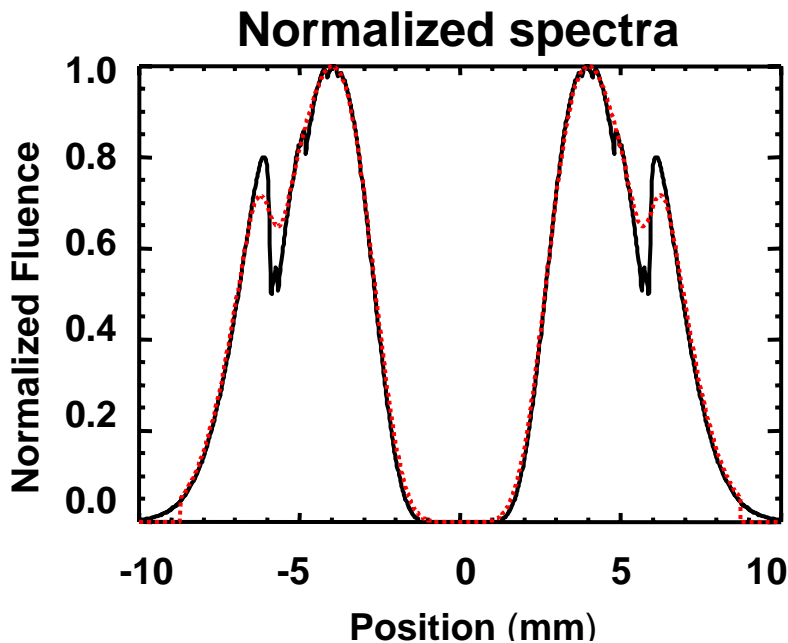


Fig. 5b. Same as Fig. 5a but with both spectra normalized. The red curve is the convolved spectrum. The effect of having a finite-sized source is also to blur out the features in the point-source spectrum due to the instrument responses.

Cryogenic target x-ray spectra OMEGA shot 44182

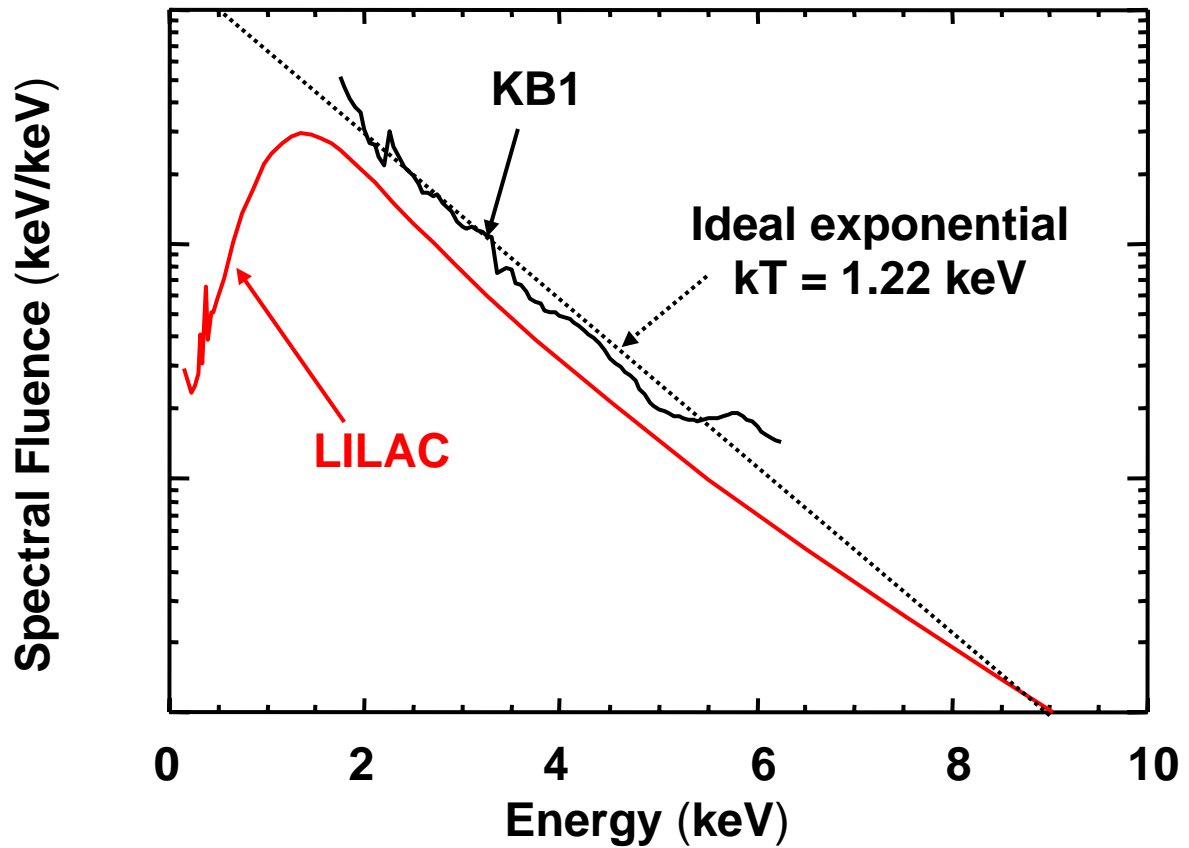


Fig. 6. Graphs of the spectral fluence, $dE/d(h\nu)$ (ds/dE integrated over space), as a function of energy. The KB1 curve is determined directly from the imaged spectrum using the KB microscope, while the LILAC curve is a hydrocode simulation. Graphing in a semi-log plot allows for a straight line fit of a simple exponential to the measured data to be determined. The slope of the line is related to the source temperature, kT .

Cryogenic target x-ray spectra OMEGA shot 44602

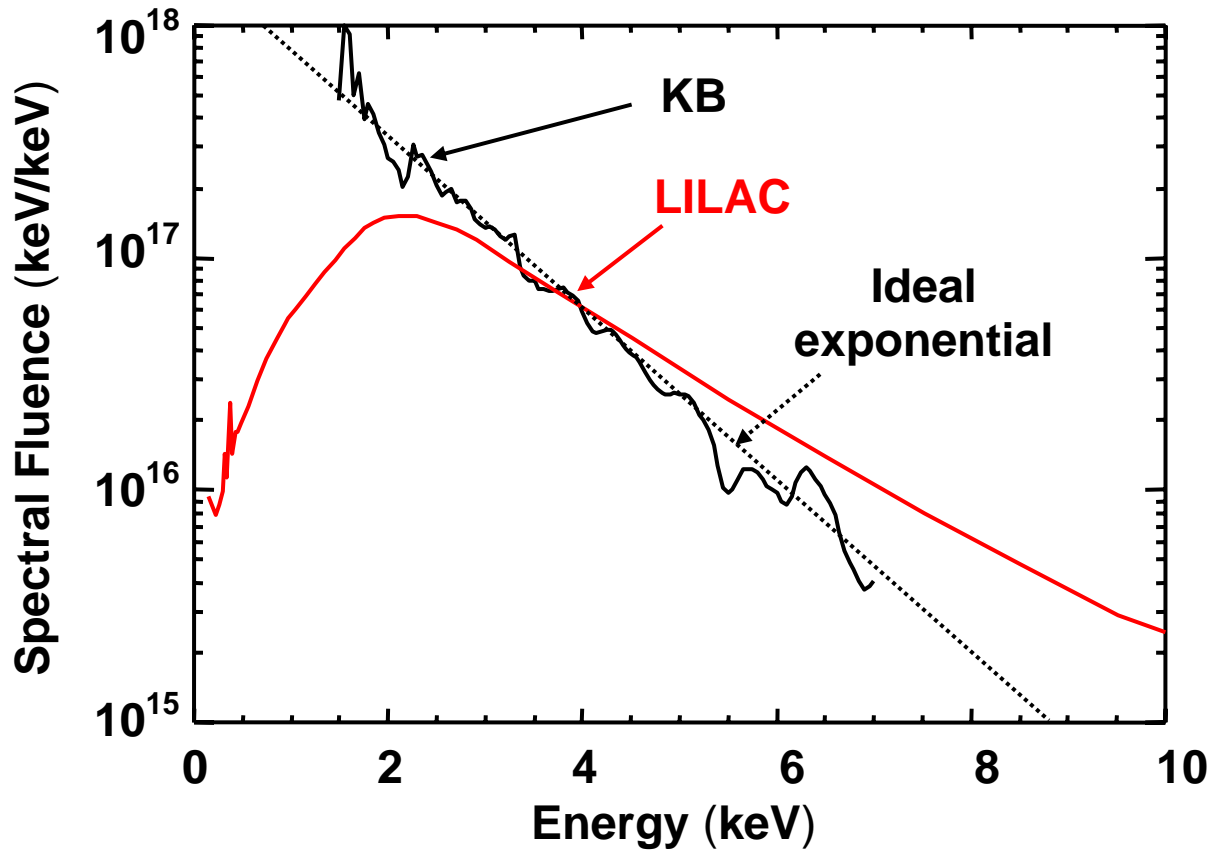


Fig. 7. Graphs of the measured, predicted, and exponentially-modeled spectral fluence of a second OMEGA laser shot.

OMEGA shot 44182

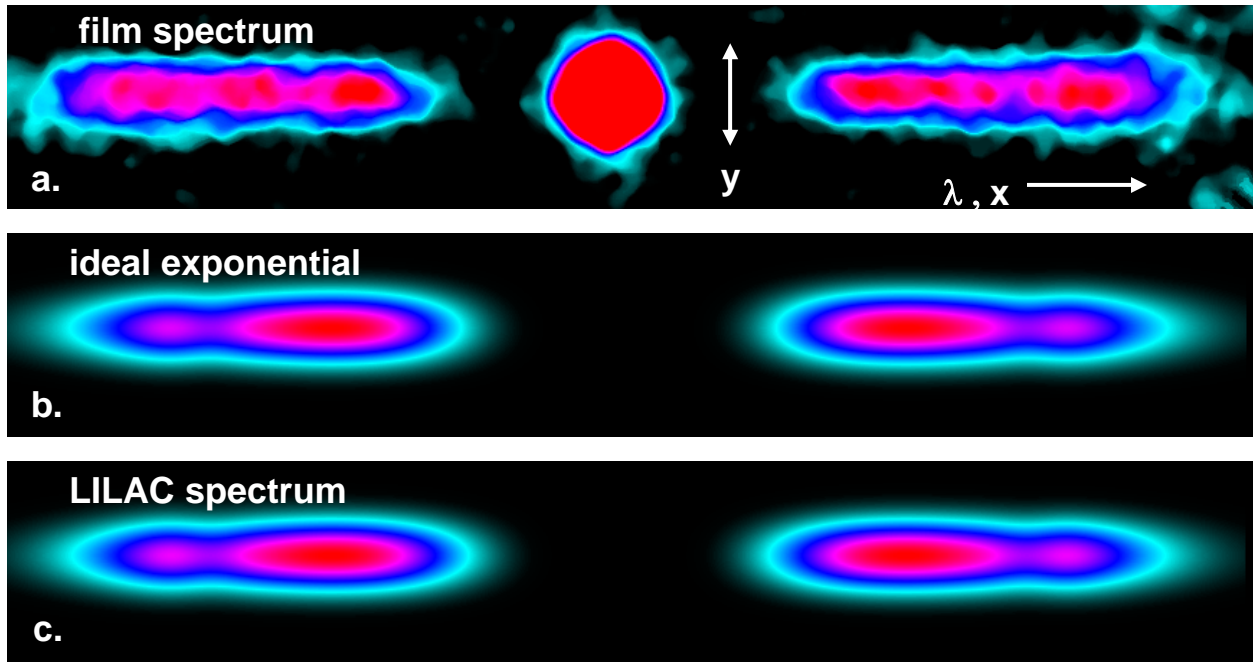


Fig. 8. Measured x-ray spectrum using a KB microscope (a), showing the zeroth and first diffraction orders. The finite size of the plasma source has blurred the first order spectra both spectrally (x direction) and spatially (y direction). Convolution of the x-ray flux df , determined from either given (LILAC) or calculated (exponential) spectral fluence values (Fig. 6), with a Gaussian source distribution results in model x-ray spectra (b & c) that can be compared with the imaged spectrum (a).

OMEGA shot 44602

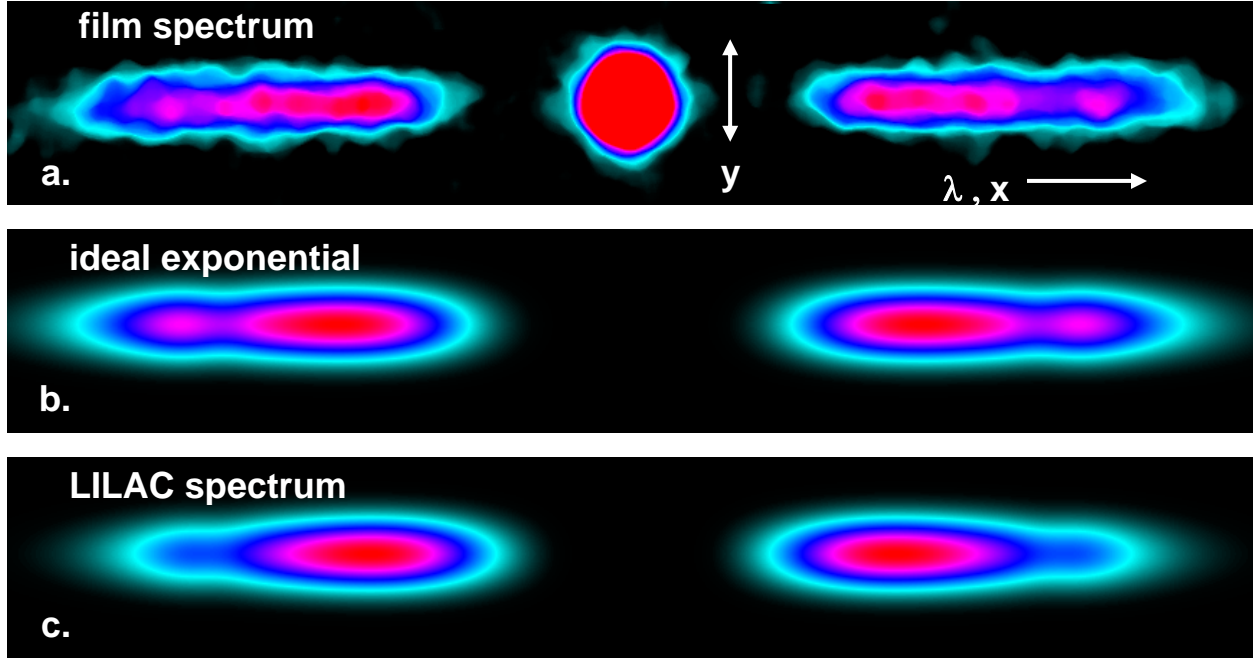


Fig. 9. Comparison of the convolved spectra from the spectral fluence values of Fig. 7 with the imaged spectrum for OMEGA laser shot 44602.

PCLC Flakes for OMEGA Laser Applications

Ryan Burakowski

PCLC Flakes for OMEGA Laser Applications

Ryan Burakowski

Churchville-Chili High School
Churchville, NY

Advisor: Tanya Kosc

Laboratory for Laser Energetics
University of Rochester
Rochester, NY

Abstract:

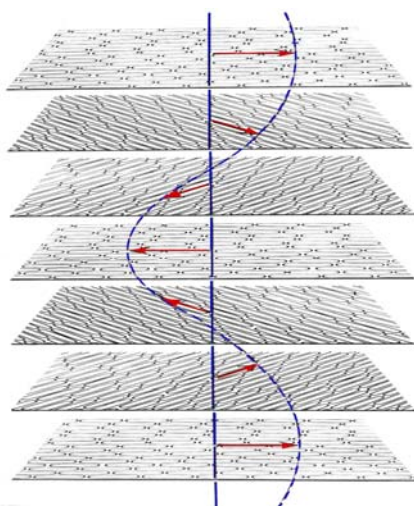
The OMEGA laser system uses over 300 liquid crystal (LC) optics to control the polarization of light. These optics are temperature sensitive and need thick, expensive glass substrates to contain the LC. Polymer liquid crystals (PLC) are much less temperature sensitive than low-molar-mass LC's and do not require thick substrates, but they are extremely difficult to align over a large area. After breaking up well-aligned small-area films of PLC's into particles called flakes, we are able to align them over large areas, potentially resulting in improved performance over the entire optic. This project studied the viability of using polymer cholesteric liquid crystal flakes for LC optics in the OMEGA laser system. This was achieved by experimenting with the concentration of flakes in a host fluid, the density and index of refraction of the host fluid, the size of the gap between the substrates, and the techniques used to assemble an optic.

1. Introduction

1.1 Liquid Crystals

Liquid crystal (LC) is a state of matter in between liquid and solid [1]. LC's flow like a liquid would, but they have more order to their molecular structure. Solids have both positional and orientational order, LC's have orientational order, and liquids have no molecular order. Some LC's have a rod-like molecular shape. The average direction in which the longest axis of the rod-like molecules is aligned is known as the director. LC's are anisotropic, meaning their properties change depending upon whether you observe them parallel or perpendicular to the director. One main property that changes is the LC's index of refraction. The difference in values in each direction for the index of refraction is called birefringence (Δn). Birefringence gives LC's some of their unique optical properties.

Substances that have an LC phase only stay in this phase over a specific temperature range. There are different types of LC's, and one especially interesting type



 Director

is the cholesteric LC (CLC). This is one of the more complex mesophases, having a large amount of organization. As the layers of molecules lay over each other, the direction of the director twists with respect to the layer above it. This forms a helical structure in the LC (figure 1.1). This molecular

Figure 1.1- Shows the twist of the director through layers of the cholesteric LC molecules. Notice the helical structure. The pitch length refers to the distance for the director to complete a 360-degree rotation.

order gives the CLC its special property of selective reflection. The wavelength of electromagnetic radiation that a specific cholesteric LC will reflect depends on the average index of refraction of the LC, the angle of incidence of the light, and the pitch length of the CLC. The range of wavelengths reflected is dependent upon the angle of incidence, pitch length, and the LC's birefringence [2] (figure 1.2).

When the selected wavelength of unpolarized light enters a cholesteric LC, the component of the light that is circularly polarized in the same direction as the spiral of the LC structure will pass through unaffected. The other half of the light, now circularly polarized in the direction opposite that of the LC structure, will be reflected back and not pass through the LC.

$$\lambda_r = \bar{n}_n P \cos \left\{ \frac{1}{2} \left[\sin^{-1} \left(\frac{\sin \theta_i}{\bar{n}_{ch}} \right) + \sin^{-1} \left(\frac{\sin \theta_r}{\bar{n}_{ch}} \right) \right] \right\}$$

Figure 1.2- Formula for determining the wavelength of maximum reflection in a CLC.

P = Pitch Length.

θ_i = Incidence angle.

θ_r = Observation angle in air.

\bar{n}_n = The average refractive index perpendicular to the helix.

λ_r = The wavelength at the center of the selective reflection band.

\bar{n}_{ch} = The approximate average cholesteric refractive index.

1.2 Polymer Cholesteric Liquid Crystal Flakes

LC's are extremely temperature sensitive. Very small temperature changes will change their properties, or even cause a phase transition to a solid or an isotropic liquid. When liquid crystal molecules, or mesogens, are incorporated into a polymer chain, the resulting polymer LC is not nearly as temperature sensitive.

One disadvantage of polymer LC's (PLC's) is that they can only be well aligned over small areas because of their extremely viscous nature. Since a PLC optic would require a large, uniform, well-aligned area they would be difficult to utilize for this application. Small areas of well-aligned PLC can be frozen with liquid nitrogen, then

broken into small solid flakes that preserve all of the important optical properties of LC's while remaining temperature insensitive (figure 1.3). These flakes vary in size, from tens to hundreds of microns. When cholesteric mesogens are used in this process it results in polymer cholesteric liquid crystal (PCLC) flakes [2].

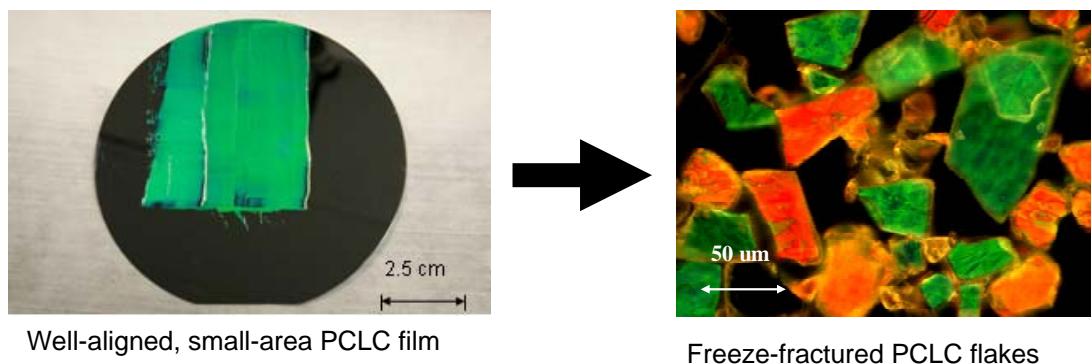


Figure 1.3- PCLC flakes

1.3 Applications

One application in which PCLC flakes could be used is to replace the circular polarizer LC optics already in the OMEGA laser system. The PCLC flakes require a much less stable environment, allowing them to be used in areas with less expensive climate control equipment (This is not an issue for Omega). The flakes devices can utilize much thinner substrates than low-molar-mass LC's, which require thick glass substrates to keep a uniform cell gap. The thicker the glass, the more distortion of the laser beam there is. Also, thinner substrates would be significantly cheaper.

A second application for the PCLC flakes would be to make a multi-wavelength filter [3]. By mixing multiple types of PCLC flakes in the same cell it is theoretically possible to make an optic that would selectively reflect multiple wavelengths. This would be useful for diagnostics purposes, such as for frequency tripling. An optic that reflects infrared and green light but transmits ultraviolet light could be used to reflect the

infrared and green light onto a sensor to measure how much of each unwanted wavelength is present after frequency tripling. This would allow the efficiency of the frequency-tripling crystals to be determined.

2. Experiment

2.1 Host Fluid

When the PCLC flakes are put into a cell they are suspended in a host fluid. There are several highly desirable traits for this fluid to have. First, it must have the same index of refraction as the PCLC flakes in use. Light is scattered at each interface between materials with different indexes of refraction (figure 2.1). When trying to build

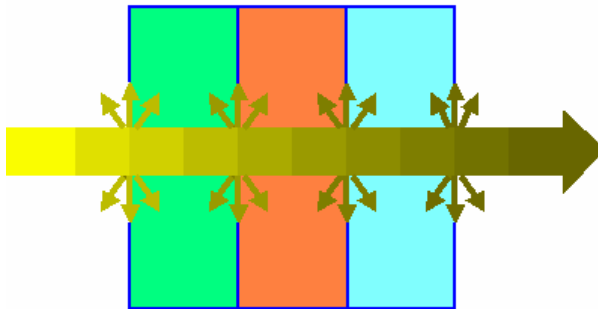


Figure 2.1- At each surface with a different index of refraction, light is scattered

a high-quality optic, scatter is a major problem. If light is scattered it is not transmitted down the laser path, decreasing the efficiency of the entire system. In order to get a fluid with the desired index of refraction and still be able to meet the other criteria necessary for a host fluid, different liquids were mixed together. This allowed a mixture to be produced with exactly the desired traits.

Second, the fluid should have the same density as the flakes. This will keep the flakes suspended in solution, allowing an optic to be turned at any angle while still giving

consistent results. Having matching densities is ideal, but not absolutely necessary. If the flakes have a different density than the fluid, they should align against one of the substrates. This may be a useful technique for encouraging alignment. The drawback to it would be that the optic could only be used in a perfectly horizontal position or with a thinner than optimal cell gap to keep the flakes from moving. I made several mixtures of fluids, some that had densities that matched the flakes and some that had different densities, to explore the relationship between mismatched densities and flake alignment.

Since the host fluid is a mixture of its component liquids, it is essential that the components are miscible with each other. To determine this, I conducted a series of miscibility tests using the liquids I planned to use in my host fluids. I took mixtures of liquids, put them into small bottles, and shook them. Only fluids that remained clear when shaken were miscible and could be used as host fluids for the PCLC flakes.

The third important requirement for the host fluid is that it must be chemically compatible with the flakes. Some fluids will dissolve the flakes, rendering them useless. In order to test for chemical compatibility, I took samples of all the fluid mixtures that met the previous standards and added a small amount of flakes to the fluids. The fluids that were chemically compatible shimmered with the light being reflected off the flakes. Since the angle of incidence partially determines the wavelength of light reflected, the bottle of fluid and flakes shimmered with many colors and was very bright. When fluids were not chemically compatible it was immediately obvious. When flakes were added the fluid turned the dark, murky brown color of muddy water. The flakes dissolved into the fluid and discolored it. Only solutions that shimmered with many colors could be used as possible host fluids.

2.2 Concentration of PCLC Flakes

An LC optic will tend to reflect all the light of one handedness (50% of the total for unpolarized incident light) at its selected wavelength while allowing all other wavelengths of light to pass through. In order for PCLC flakes to achieve this goal, there must be a large number of flakes that are all well-aligned in a cell. They must uniformly cover the entire aperture of the optic to produce a uniform beam of reflected light. One of the most important aspects of determining the viability of a PCLC circular polarizer is getting enough flakes into the cell gap. No matter how well aligned they are, if there are not enough flakes the device will not be efficient enough to be utilized. In order to test how many flakes an optic can hold effectively under a given set of parameters, I built small test cells to simulate the properties of an optic. I used microscope slides as substrates, and cut them to about 2/3 of their original length to make the area in which I had to align the flakes smaller. By mixing glass microspheres into UV epoxy, and then adhering two slides together by putting dabs of epoxy at each of the four corners, I created a test cell that had a uniform gap, the size of which depended upon the microspheres used (figure 2.2). By holding every variable the same except for flake

Side View of Test Cell

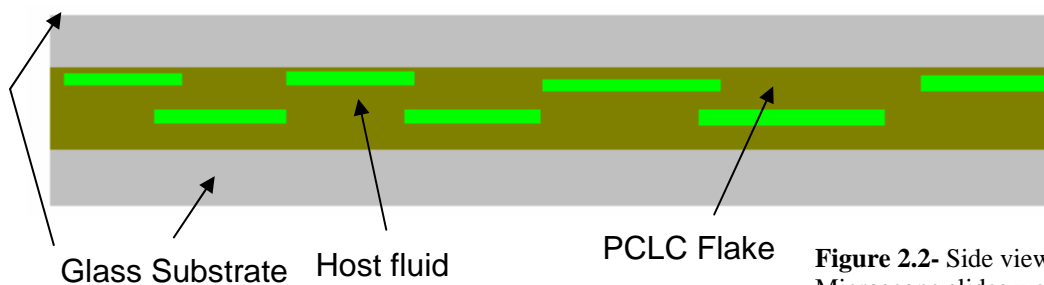


Figure 2.2- Side view of a test cell. Microscope slides were used as the glass substrate.

concentration in the host fluid, I was able to make a series of test cells that showed the relationship between concentration and maximum reflectance.

2.3 Alignment Techniques

The other important factor for determining the viability of a PCLC flake device is how well the flakes can be aligned. If they are not all lined up in the same plane, the flakes will target different wavelengths of light as the angle of incidence of the light affects the wavelength of light that will be reflected. Several different methods to force the PCLC flakes to align were tried. One was changing the characteristics of the host fluid, namely its density. Another was using different methods to construct the test cell. These methods should be able to be adapted to the construction of a full-size optic. By keeping all the variables the same except for the alignment technique I was testing, I developed cells to be used as controls and cells to experiment with alignment techniques. By comparing these cells against one another, I was able to tell whether the technique helped in flake alignment.

2.4 Cell Gap

The cell gap is a significant variable, but not directly related to the efficiency of the optic. The amount of flakes that can be fit into an optic (concentration) and how well they are aligned will ultimately determine whether PCLC-flake circular polarizers are feasible. The gap between the two substrates is important because it directly affects both the concentration limits of flakes in the host fluid and how well they are able to be aligned. In order to determine the best possible size for the cell gap, I first had to find the

best way to align the flakes and what the optimum concentration of flakes was. Then, using these parameters to build several test cells that were identical except for the gap between the substrates, I was able to compare the results from these test cells and determine the best possible size for the cell gap. The results from these experiments are given in section 3.4.

2.5 Multi-wavelength Filters

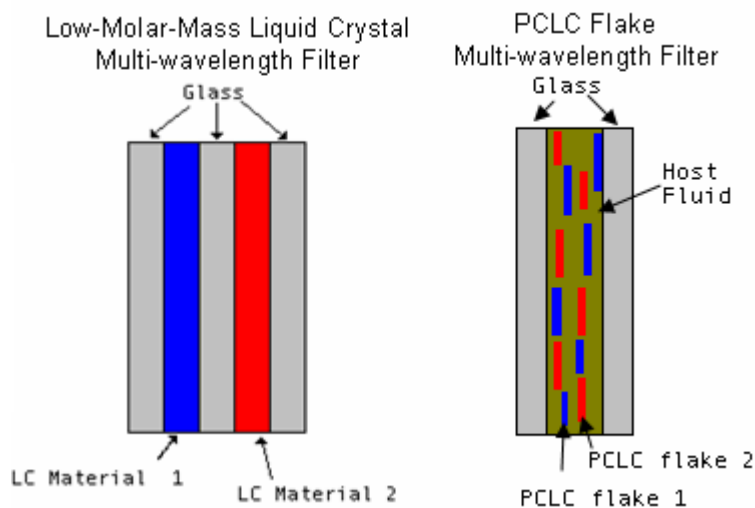
Multi-wavelength filters are an extension of circular polarizers. When constructed using low-molar-mass LC's, multi-wavelength filters are circular polarizers layered together into one larger optic. Each individual layer of LC reflects one wavelength of light, and the multiple layers of different LC result in a multi-wavelength circular polarizer. Because of the need to have layers of glass separating each type of liquid crystal, there is a large amount of scatter and specular reflection in these optics.

PCLC flakes can theoretically make more efficient multi-wavelength filters. Since different types of flakes that would reflect different wavelengths of light do not react with each other, it should be possible to put multiple types of flakes into the same cell gap. This type of optic would require much less glass than comparable low-molar-mass LC filters, meaning there would be less unwanted reflections and less scatter (figure 2.3).

All the challenges of making a PCLC flake circular polarizer would be magnified in a multi-wavelength filter. There would need to be a great amount of several different types of flakes, and they would all have to be well-aligned. In essence, if a device is built with two reflective wavelengths, the requirements in concentration and alignment for a

circular polarizer must be met twice over. The main goal of this project is to attempt to prove a single-wavelength polarizer viable. Testing on multi-wavelength filters shows that the scope of this project can be expanded upon.

Figure 2.3- A low-molar-mass liquid crystal multi-wavelength filter compared to a PCLC flake multi-wavelength filter. The PCLC flake filter uses much less glass, which is expensive and increases scatter.



3. Results

3.1 Host Fluid

Through the process described in section 2.1 I found a host fluid that matched all the desired criteria. The calculations for determining the index of refraction and density of a fluid made from two components are based upon a linear relationship to the percent composition of each liquid. In the search for the right host fluid I conducted tests using mixtures that included Bromonaphthaline, PDM-7050, propylene carbonate, DMS-T12, Mistie, and DMS-T31. I found the ideal fluid in the form of a mixture of 10.7% propylene carbonate and 89.3% PDM-7050. It had the same index of refraction, 1.57, as the flakes I was using, was chemically compatible with the flakes, and the components were miscible with each other. The density of the fluid was nearly ideal, too. The

density of the flakes I used was $\sim 1.10 \text{ g/cm}^3$, and the fluid's density was calculated to be 1.101 g/cm^3 .

3.2 Alignment Techniques

I tried several different techniques to align the PCLC flakes. The first was manipulating the host fluid. By having a fluid with a density that was different from that of the flakes, the flakes were forced to align against one of the substrates. An interesting finding was that when the density of the fluid was greater than that of the flakes, forcing them to rise to the surface, the cell reflected a higher percentage of light at its targeted wavelength, yet when the density of the fluid was less than that of the flakes, allowing them to sink to the bottom, the reflection at the targeted wavelength actually decreased. By using a host fluid that had a density 0.1 g/cm^3 greater than that of the flakes, maximum

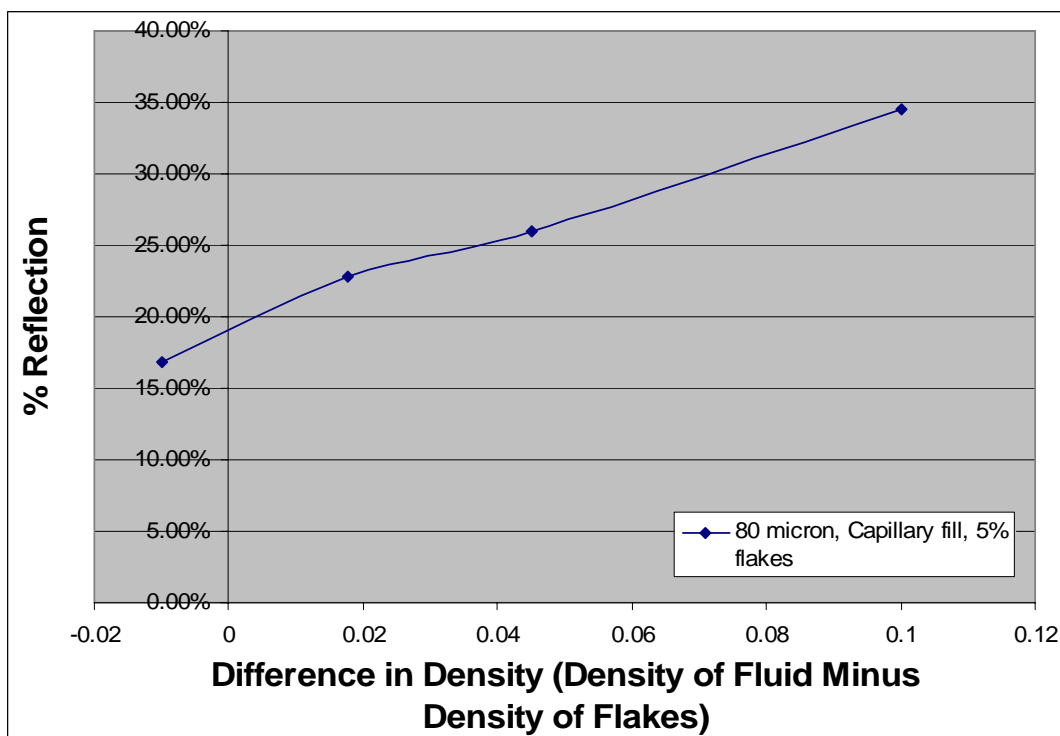


Figure 3.1- Dependence of the reflectivity on the density of the host fluid relative to the PCLC flakes. All factors except for the density of the host fluid were held constant. The relationship is nearly linear.

reflection was increased substantially from 22.8% to 34.6% (figure 3.1). The 34.6% reflectivity was the highest observed in any of the tests. This shows that a density difference could be an extremely effective alignment technique if the optic it was applied in could stay perfectly horizontal throughout its entire operating life. Since this is not the case in the OMEGA laser system at the moment, I had to find another method for aligning the PCLC flakes in my test cells.

The other method I used in an attempt to improve alignment was to alter the way the test cells were built. Traditionally, test cells were constructed by adhering the two substrates together and then filling the gap with the PCLC flakes in their host fluid by utilizing capillary action. I tried two new methods of construction of the cells. The first method was to put the PCLC flakes in the host fluid on the bottom substrate, and then put the top substrate on and shear the substrates against each other moving in the longer direction of the microscope slides (figure 3.2). This improved upon the results from the



Figure 3.2- The shear method. Arrows show which way the top substrate slides over the bottom substrate.

capillary fill method used previously, increasing reflection from the previous maximum of 22.8% to 28.5%. The second new construction method was the “twisting shear” method. It also started with putting the PCLC material on the bottom substrate, but then the top substrate was twisted back and forth across the bottom substrate (figure 3.3). This improved reflection even more than the first shearing method I experimented with (figure 3.4), reaching a maximum reflection of 30.18% at a concentration of 7.5% flakes by weight.

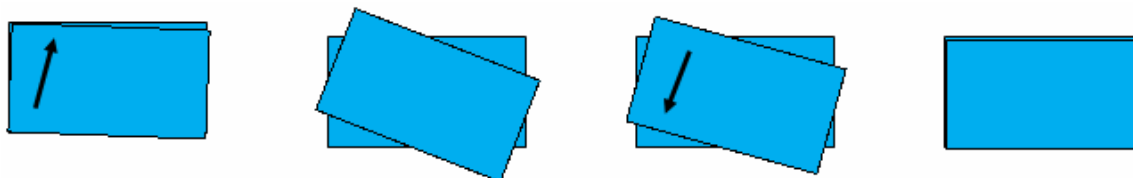


Figure 3.3- The “twisting shear” method. The arrows show which way the top substrate slides over the bottom substrate. This is the most effective method of aligning the flakes.

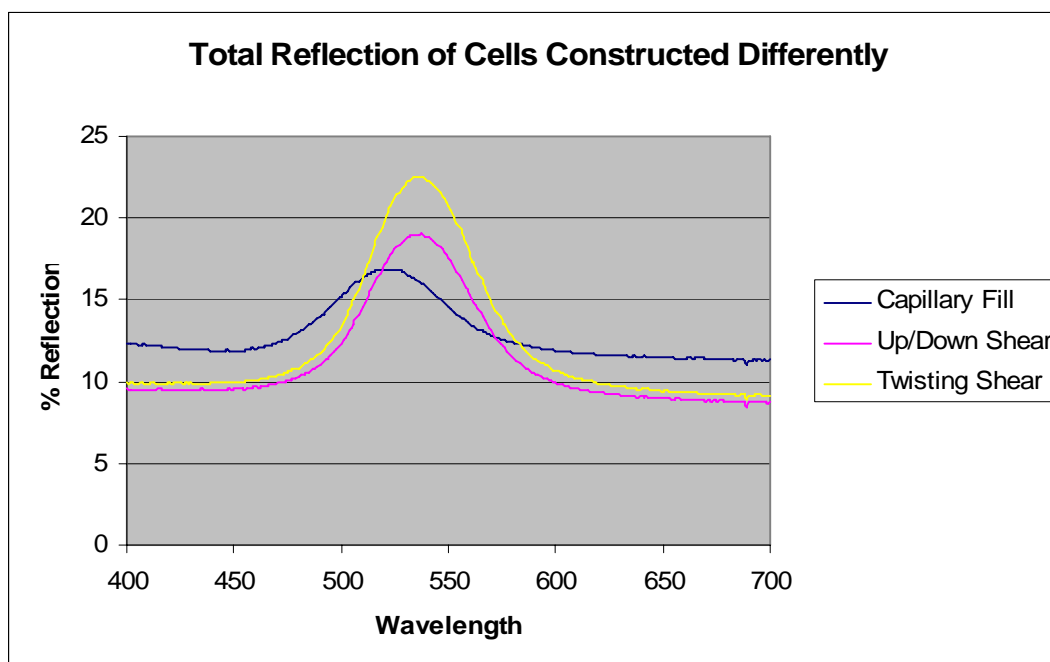


Figure 3.4- A graph showing the total reflection of cells constructed three different ways. All cells were built with an 80 um cell gap using 5% flakes by weight. The only differences between the cells are the methods used for construction. The twisting shear technique gives the highest reflection of any construction method. The differences in wavelength of maximum reflection and wavelength ranges are brought about by flakes that are not perfectly aligned, altering the angle of incidence of the light on the flakes. Note: These reflectivities are not the maximum values for the construction methods. The cells were made using less than optimal flake concentration.

3.3 PCLC Flake Concentration

From previous work done on PCLC flake concentration in an optic it was concluded that the optimum concentration of flakes in percent by mass was 5% [3]. This work used the typical construction method for test cells and relied upon capillary action

to fill the cell gap. With my new alignment technique of “twisting shear”, I was able to bolster the optimum concentration to 7.5% flakes by weight, an increase of 50% over the previous concentration achieved (figure 3.5).

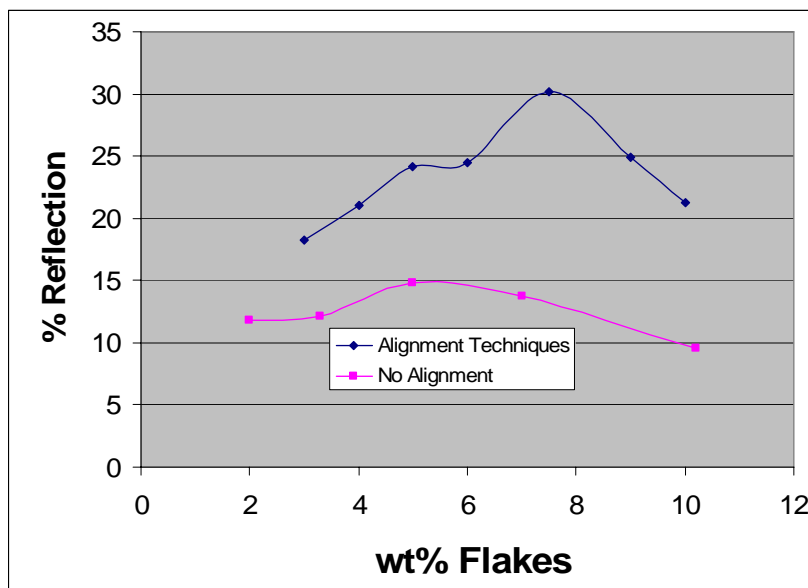


Figure 3.5- A graph showing the reflectivity of cells vs. the concentration of flakes in percent by weight for cells in this study (aligned) and for previously made cells (not aligned). The alignment techniques drastically increased the amount of flakes that can be effectively inserted into a device, thereby increasing reflectivity. The optimum amount of flakes was increased from 5% by weight to 7.5% by weight.

3.4 Cell Gap

In initial experiments, when finding out the optimized concentration of PCLC flakes in a test cell filled by capillary action, there was no variation in cell gap [3] [4]. It was not known how changing the cell gap would affect the concentration and alignment of flakes. Through my tests, regardless of what construction method was used, an 80 um cell gap yielded the highest consistent reflectivities. The reflectivity of my test cells drastically decreased when the cell gap decreased. The maximum reflection for a test cell made with an 80 um cell gap was 30.18%, while the maximum for a 40 um cell gap was only 22.49%. When the cell gap is increased to over 80 um, the reflectivity of the cell varied randomly. This shows that the flakes have too much room to float around in and are constantly changing their alignment. It seems that an 80 um cell gap allows for

the greatest number of flakes in the cell while keeping them well-aligned, yielding the highest consistent reflectivities.

3.5 Multi-wavelength Filters

I made a two-color filter with flakes reflecting in the red and flakes reflecting in the blue range. The reflectance measured by a spectrophotometer clearly showed two peaks, one in the red wavelength range and one in the blue range (figure 3.6). This proved that the concept of a multi-wavelength PCLC flake filter is viable. Using 5% by mass of each kind of flake for a total of 10% flakes, I was able to reach a maximum of 22% reflection at each peak, while still letting the same amount of untargeted light transmit through as in a single color PCLC circular polarizer. This is a very promising area for future study.

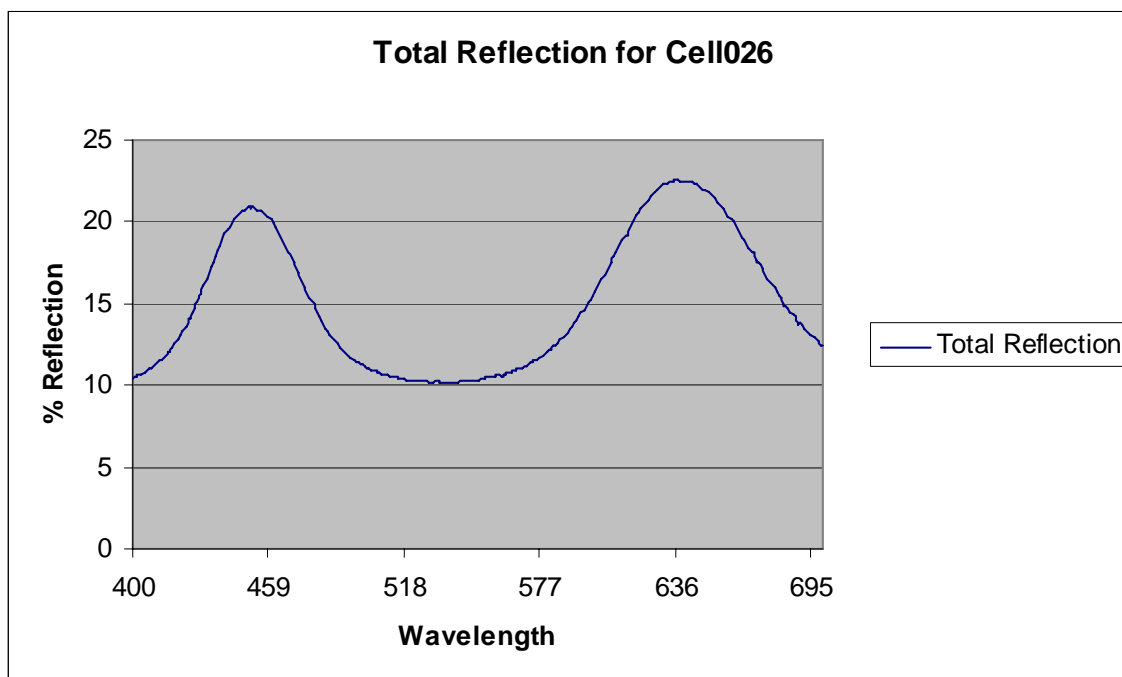


Figure 3.6- A graph showing reflectivity vs. wavelength in a two-color PCLC multi-wavelength filter. One PCLC flake type reflects light in the blue range and the other PCLC flake type reflects light in the red range. Notice the two distinct peaks in the graph. Each one represents the targeted wavelengths of one kind of PCLC flakes. Reflection went down to normal levels between the peaks, indicating that the two flake types did not interfere with each other.

4. Conclusion/ Future Work

4.1 PCLC Circular Polarizers

The goal of this work was to determine the viability of a PCLC flake circular polarizer. Even though significant advances were made in this work, it is likely that more improvement will be made in the future. Previously, the maximum reflectivity achieved with a PCLC-flake circular polarizer was 14.8%. Through the use of new construction techniques that facilitated flake alignment and increased the maximum amount of flakes that can be used in a cell, the reflectivity was increased to 30.18%, doubling the effectiveness of these cells (figure 4.1). There is still room for improving the reflective

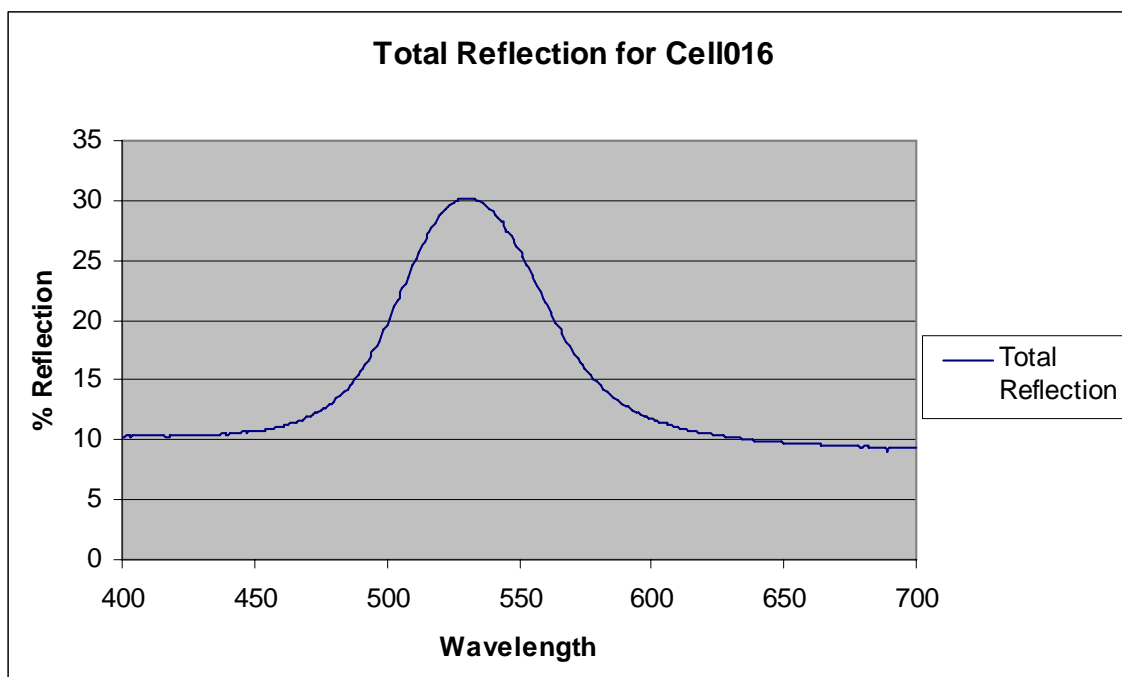


Figure 4.1- The graph of reflectivity vs. wavelength for a cell constructed using the twisting shear method, an 80 um cell gap, and an ideal host fluid with 7.5% flakes by weight suspended in it. The maximum reflectivity I was able to achieve was 30.18%. This is the highest reflectivity in this work that uses a density-matched fluid.

characteristics of these devices, such as using a UV curable polymer to lock well-aligned flakes into place while using only one substrate or wetting the base substrate, sprinkling

hydrophobic flakes onto the wet glass, then allowing the water to dry, leaving the flakes that had been on the surface of the water to lay flat on the substrate. With more experimentation and new methods for the alignment of the PCLC flakes, it could well be possible to use PCLC flake circular polarizers in the OMEGA laser system.

4.2 Multi-wavelength Filters

Multi-wavelength PCLC flake filters were tested to determine whether the theory behind them can be valid. The concept was demonstrated through reflectivity measurements taken on a test cell using multiple PCLC flakes that targeted different wavelengths. The graph of reflectivity vs. wavelength plotted for a two-colored circular polarizer clearly showed two distinct peaks characteristic of the selective reflection properties of the two types of PCLC flakes. The two types of flakes in the cell did not interfere with each other. Further work on this type of optic will be carried out to evaluate its potential for use in diagnostics in the OMEGA laser system because of the benefits that can be realized through this design.

5. Acknowledgments

First, I would like to thank Dr. R. Stephen Craxton for giving me the opportunity to pursue this project. I would also like to thank my advisor, Dr. Tanya Z. Kosci, for all the help she has willingly given me. Others who deserve special recognition are Dr. Stephen Jacobs, Mr. Ken Marshall, Christopher Coon, and Katherine Hasman.

6. References

- 1) P.J. Collings and M. Hird, *Introduction to Liquid Crystals: Chemistry and Physics* (Philadelphia, PA: Taylor and Francis, 1997).
- 2) E.M. Korenic, S.D. Jacobs, S.M. Faris, and L.Li, "Cholesteric liquid crystal flakes-a new form of domain," *Mol. Cryst. Liq. Cryst.* 317, 197-219_1998.
- 3) Kosc, Tanya Z., private communication.
- 4) Marshall, Ken, private communication.

Development of Polar Direct Drive Designs for Initial NIF Targets

Alexandra Cok

Development of Polar Direct Drive Designs for Initial NIF Targets

Alexandra M. Cok

Allendale Columbia School

Rochester, New York

Advisor: Dr. R. S. Craxton

Laboratory for Laser Energetics

University of Rochester

Rochester, New York

November 2006

Abstract

This work proposes a means by which the National Ignition Facility (NIF) laser system, being built for indirect-drive laser fusion, can be used for symmetric direct-drive implosions producing high fusion neutron yields as soon as the NIF is operational. It uses polar direct drive (PDD), which involves repointing the laser beams away from the center of the target in an attempt to maintain shell radius uniformity during the implosion. All PDD designs proposed to date need specially designed phase plates that will not be available for initial NIF experiments. However, this work shows that good uniformity can still be obtained without special phase plates by certain combinations of defocusing and pointing of the beams, including pointing offsets of individual beams within the NIF laser beam quads, which are easy to implement. Two designs have been developed using the two-dimensional hydrodynamic simulation code SAGE. The first design uses the elliptical phase plates that will be used for indirect drive on the NIF; the second design uses no phase plates. Both designs will make high-yield direct-drive implosions possible with the initial NIF setup.

1. Introduction

Nuclear fusion provides a possible source of clean, abundant energy. One approach to fusion uses laser beams to irradiate a spherical target containing fuel comprised of deuterium and tritium, two isotopes of hydrogen, inside a shell of a material such as plastic or glass. The outside of the shell ablates outwards and the inside is compressed inwards, compressing the fuel to high densities and temperatures. The extreme temperature of the fuel overcomes the Coulomb repulsion forces of the positively charged nuclei, and the extreme compression ensures a large number of fusion reactions before the fuel explodes. The deuterium and tritium fuse to form a helium nucleus, releasing an energetic neutron. Most of the energy released by fusion reactions is

in the form of energetic neutrons. The energy of the helium nucleus is redeposited in the compressed fuel if the density and radius of the fuel are great enough. This redeposition of energy is known as ignition. Ignition is the first step to gaining breakeven, when the energy released from fusion reactions exceeds that input by the laser. Laser fusion will not be a viable source of abundant energy unless breakeven is achieved.

There are two different approaches to laser fusion: direct drive¹ and indirect drive². With direct drive, laser beams hit the target pellet at normal incidence from all directions [Figure 1(a)]. This is the type of fusion for which the OMEGA laser system at the University of Rochester's Laboratory for Laser Energetics is configured. With indirect drive, the target pellet is surrounded by a “hohlraum”, a cylinder made of gold or another material with a large atomic number [Figure 1(b)]. Laser beams enter the hohlraum through openings cut into the top and bottom. When hit by the laser beams, the hohlraum emits x rays, which then irradiate the target pellet, providing the energy needed for compression. Almost all of the initial laser energy is absorbed by the gold and close to 80% is reemitted as x rays. However, only 20% is actually absorbed by the target pellet; the rest is absorbed by the walls of the hohlraum or lost through the openings in the hohlraum. The lower energy efficiency of indirect drive is made up for by the greater uniformity of x ray radiation of the target. The National Ignition Facility (NIF), currently being constructed at Lawrence Livermore National Laboratory, will be configured for indirect drive.

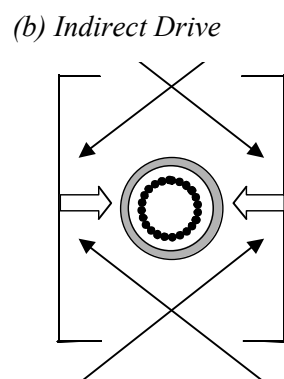
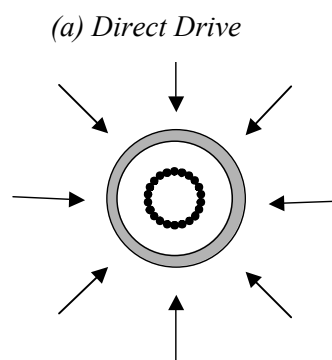


Figure 1. The two main approaches to laser fusion. (a) In direct drive, the laser beams irradiate the target pellet. Arrows represent laser beams and the dotted circle shows how the shell implodes. (b) In indirect drive, the target pellet is contained in a cylindrical hohlraum, which is hit by lasers entering through holes in the top and bottom of the hohlraum. The hohlraum produces x rays (open arrows), which irradiate the target.

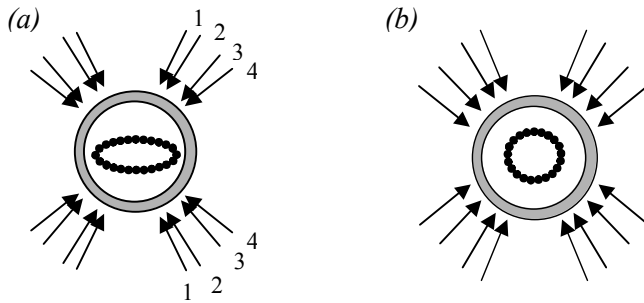


Figure 2. The possible ways in which the NIF laser beams, positioned for indirect drive, can irradiate a direct-drive target. (a) When the laser beams are aimed at the target center, the shell implodes nonuniformly. (b) Polar direct drive, in which the beams are repositioned away from the center of the target, causes a nearly uniform implosion. Rings 1-4 are indicated in (a).

The NIF is due for completion in 2010, at which point it will become the world's most powerful laser. The NIF has 192 beams designed to deliver a total of 1.8 MJ of energy to the target, theoretically enough energy to achieve ignition and breakeven. The NIF laser beams are incident from the top and bottom of the target pellet. The laser beam ports are arranged in four rings at angles of 23.5° , 30.0° , 44.5° , and 50.0° from the vertical in the upper hemisphere with four corresponding rings in the lower hemisphere. There are a total of 48 ports; laser beams are arranged in groups of four called quads, so there is one quad per port. Each beam is square, measuring 40 cm by 40 cm. Symmetric direct-drive experiments, with a configuration similar to that shown in Figure 1(a), are not planned until around 2016, as this will involve repositioning half of the beams to another ring at 77.45° , an expensive and time-consuming process. A scheme termed polar direct drive (PDD)³ has been proposed to enable earlier direct-drive experiments on the NIF. If the indirect-drive beams are simply aimed at the center of the target, as in Figure 2(a), the target shell receives significantly more drive on the poles than on the equator. As a result, the ratio of the shell velocity at the poles to the shell velocity at the equator is approximately two to one. Such distortion in the shell is not acceptable since shell radius uniformity is necessary to obtain high compression. The proposed PDD solution to this is to reposition the beams away from the center of the target, minimizing the differences in the amount of drive on all portions of the target shell [Figure 2(b)].

Prior to producing the energy required for ignition experiments (1.0 to 1.8 MJ), the NIF

laser system and diagnostic systems will be tested at an energy of 375 kJ to ensure that the laser optics are not damaged. In particular, the neutron diagnostic systems must be tested. Direct-drive fusion must be used to obtain the maximum number of neutrons at this energy, because at low energies indirect drive cannot provide sufficiently high temperatures and compression to yield as large a number of neutrons. Therefore, PDD designs maximizing the shell radius uniformity must be developed.

All previous PDD designs³⁻⁶ required special phase plates (see Section 2.2 below). Unfortunately, these will not be available initially on the NIF. This work has investigated alternate ways of developing PDD designs, involving certain combinations of beam defocusing and pointing that are straightforward to implement. This work has resulted in two designs that will make the desired initial experiments possible.

2. Parameters Available for Optimization

The key parameters available for developing the two-dimensional designs are specifications for shifting the beam pointings away from the center of the target and defocusing the beams (Section 2.1). The optimum combinations of shifting and defocusing depend on the availability of indirect-drive phase plates (Section 2.2). Section 2.3 describes “split quads” in which the four beams are shifted slightly differently so that they do not overlap exactly.

2.1 Shifting and Defocusing

Figure 3(a) shows the important optics near the end of the laser system that control the parameters described here. The beam pointing is shifted away from the center of the target by moving the mirror. The center of the beam then moves a specified distance in the direction perpendicular to its axis, so that the beam hits the target at a different spot [Figure 3(b)].

Defocusing the beam is done by moving the focus lens toward the target. The laser beam

spot on the target is then enlarged and the maximum intensity decreases. To gain the best uniformity and overlap of laser beams, the diameter of the beam spot should generally correspond to the diameter of the target shell. Defocusing can be used to change the relative intensities of the four rings of beams as well as to change the size of each beam spot.

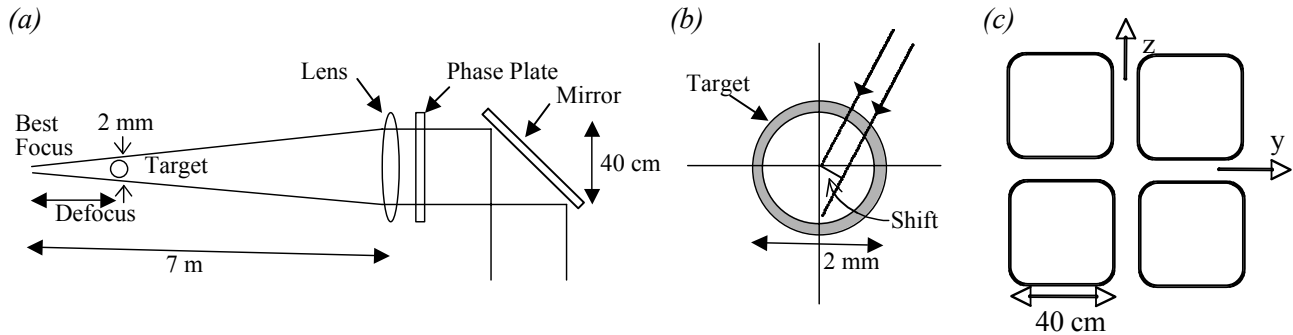


Figure 3. (a) Diagram (not to scale) showing the parts of the laser that control the parameters used in this work. Moving the lens along the beam axis controls the size of the beam at the target and tipping the mirror controls beam pointing. (b) Diagram showing how beam ring shifts are measured perpendicular to the beam direction. The angle of the beam from the vertical remains virtually constant. (c) Diagram showing the arrangement of four beams in a quad at the output of the laser system.

2.2 Phase Plates

Laser beams accumulate small irregularities in coherence after passing through the many amplification optics. These irregularities, if uncorrected, will imprint as hot spots on the target affecting the uniformity of the implosion. Phase plates^{7,8} are special optics through which the beams pass before they are focused. A phase plate spreads the energy of the beam slightly to give a more uniform beam after focusing. Different types of phase plates are used to produce different sizes of beam spots. For direct drive, the beam spots need to be large to cover the target. For indirect drive, the beams need to be small enough to pass through the openings in the hohlraum without hitting the edges of the openings and generating plasmas (see Figure 4). Such plasmas would cause the laser beam rays to refract and strike the hohlraum wall in the wrong place or even prevent the rays from entering the hohlraum. The NIF will have two different types of phase plates: those for inner beams (rings one and two, see Figure 4) and those for outer beams

(rings three and four). The phase plates that will be used on the NIF will produce small elliptical focal spots because of the angles at which the beams enter the hohlraum (see Figure 4). The size of the spot depends on the angle at which the beams pass through the openings in the hohlraum. Therefore, since the beams in rings three and four enter at much shallower angles, their spot sizes must be smaller than those produced for rings one and two. The small spot sizes produced by the NIF indirect-drive phase plates make them unsuitable for direct-drive experiments unless the beams are defocused. The development of two PDD designs in this work, one with phase plates and one without, allows for flexibility depending on the availability of the NIF indirect-drive phase plates.

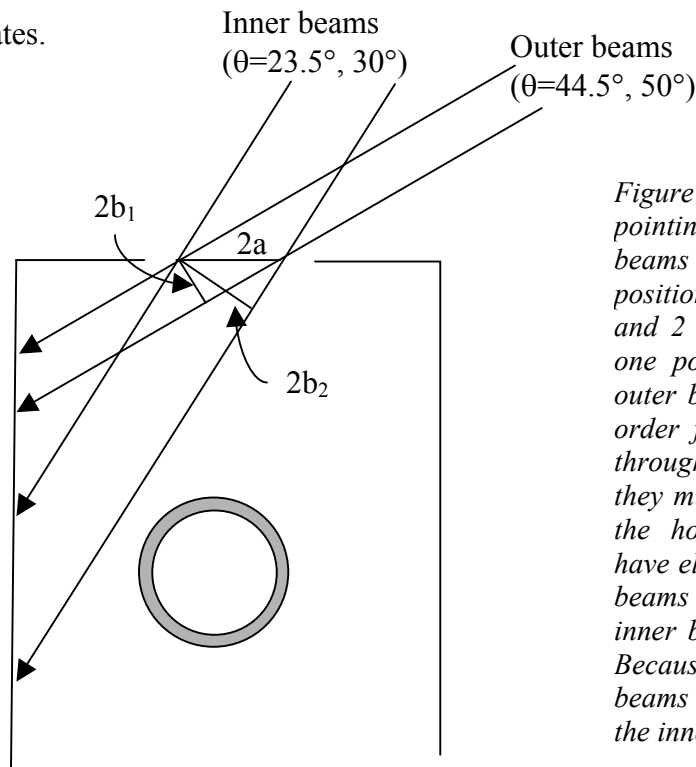
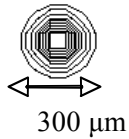


Figure 4. The proposed indirect drive pointings for the NIF. From each end, beams are aimed at two vertical positions on the hohlraum wall. Rings 1 and 2 (the inner beams) are aimed at one position and rings 3 and 4 (the outer beams) are aimed at another. In order for the beams to be able to fit through the openings in the hohlraum, they must be circular as they pass into the hohlraum. Therefore, the beams have elliptical cross sections. The outer beams have semi-axes (a , b_1) and the inner beams have semi-axes of (a , b_2). Because of the greater angle, the outer beams are much more elliptical than the inner beams.

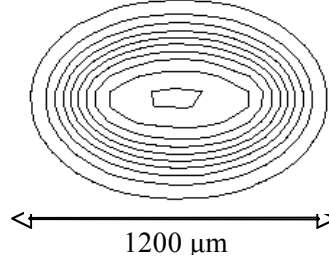
Figure 5 shows a comparison of beams in best focus and beams out of focus, with and without phase plates. Figure 5(a) shows the intensity contours of a small ring-four best-focus spot without a phase plate, whose size is determined by the optical aberrations in the laser. Each contour represents a 10% increase in intensity, starting at 10% of peak intensity. Figure 5(b) shows a ring four beam in best focus with a phase plate. Figures 5(c) and (d) show the intensity

contours of a ring-four beam out of focus (defocused by 1.7 cm) with and without a phase plate. Without a phase plate, the best-focus spot is round. As the beam is taken farther out of best focus, the spot becomes increasingly square, corresponding to the square beam shape at the output of the laser.

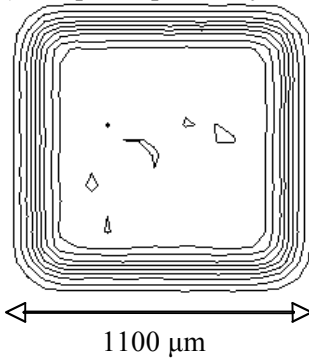
(a) No phase plate, best focus



(b) Phase plate, best focus



(c) No phase plate, defocused



(d) Phase plate, defocused

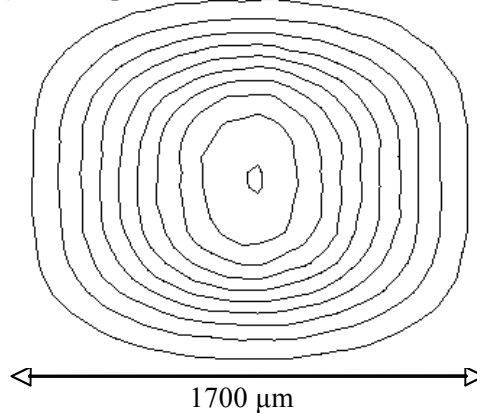


Figure 5. (a) The intensity contour plot of a ring 4 beam in best focus. (b) The intensity plot of a ring 4 beam with a phase plate in best focus. (c) A ring 4 beam without a phase plate, out of best focus with a defocus distance 1.7 cm. (d) A ring 4 beam with a phase plate, out of best focus with a defocus distance

2.3 Split Quads

The four beams of each quad, arranged at the output of the laser as shown in Figure 3(c), are usually focused down to a single focal spot. However, as each beam has an adjustable mirror, as shown in Figure 3(a), it is possible to adjust the pointings of the four beams so that they are focused to slightly different spots. This changes the overall shape of the intensity contours. Quads with pointings altered in this way will be referred to as “split quads.” Using split quads, it is possible to alter the shape of the beams from the elliptical spots created by the phase plates and

to alter the rate at which the intensity of the beam drops off away from the center of the beam.

Intensity contour plots of ring four beams using split quads are shown in Figure 6. These beams are the same as those shown in Figure 5, except that in Figure 6 the beams have split quads. In Figures 6(a) and (b) each beam is in best focus with and without a phase plate. In Figure 6(c) and (d) each beam is out of focus (defocused by 1.7 cm). Figures 6(c) and (d) also show the actual ring-four beam profiles used in the designs described later in this report. The rate at which the intensity of the beam drops off away from the center of the beam is much less steep when using a split quad [compare Figures 5(c) and 5(d) to Figures 6(c) and 6(d)]. The difference is especially notable when not using a phase plate. By using a combination of split quad shifting and defocusing, the NIF beams can be enlarged by a factor of two or even more if necessary.

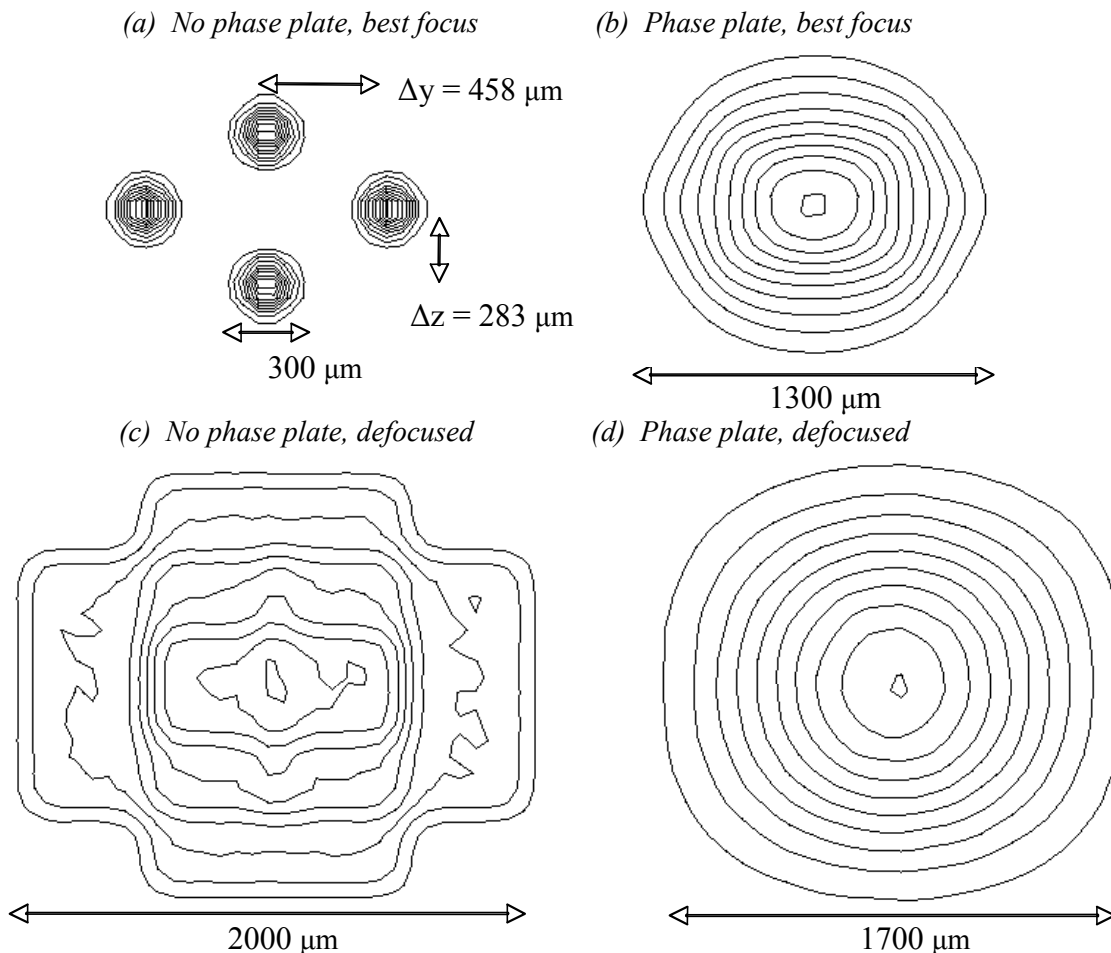


Figure 6. As in Figure 5, but each beam uses a split quad with shifts $(\Delta z, \Delta y) = (283 \mu\text{m}, 458 \mu\text{m})$ in (a) and (c) and $(\Delta z, \Delta y) = (247 \mu\text{m}, 155 \mu\text{m})$ in (b) and (d). (c) and (d) show the intensity contours of the ring 4 beams actually used in the designs discussed later in this report.

3. Target Design

The target designed to maximize the neutron yield at a total laser energy of 375 kJ is a shell of 8 μm of glass (SiO_2) with a radius of 1100 μm . The shell is filled with ten atmospheres of deuterium-tritium (DT) gas. The laser pulse used on this target is a Gaussian-shaped pulse shown in Figure 7(a). The pulse lasts a total of 5 ns with its peak power at 2.5 ns.⁹

When the laser pulse hits the target shell, the outer layers of the shell reach extreme temperatures and form a coronal plasma around the target. A plasma is a gaseous cloud of electrons and positively charged ions. The plasma expands outward and more layers are ablated as the laser power increases. The high pressure in the plasma causes the shell to accelerate inward. The motion of the center of mass of the shell, as predicted by the hydrodynamic code SAGE¹⁰, is shown in Figure 7(b) as the red curve. Peak compression of the gas inside the target shell occurs just after 3 ns. Figure 7(b) also shows a number of density contours including the critical density (n_c), the density past which the laser cannot penetrate. Most of the laser energy is deposited between critical density and quarter-critical density ($n_c/4$).

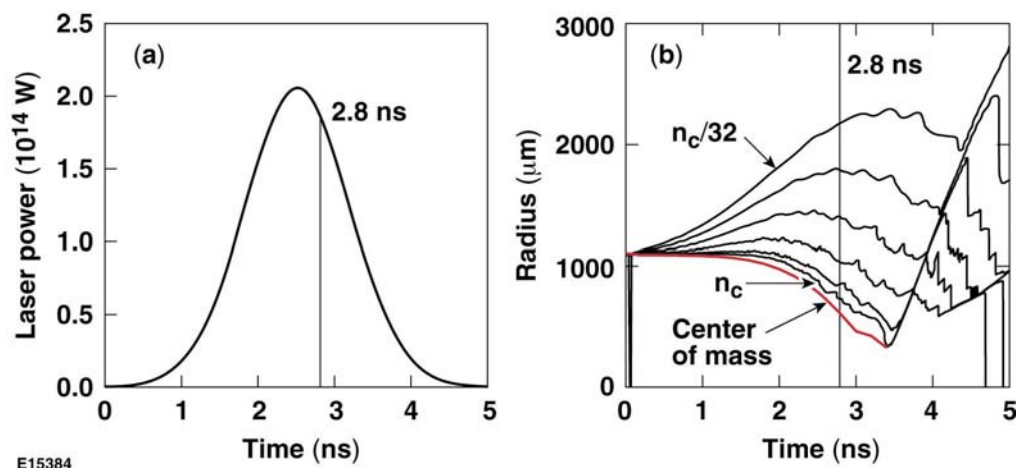


Figure 7. (a) Laser power versus time. This design used a Gaussian pulse. (b) Radius versus time of several density contours in the coronal plasma, including critical density (n_c). The outer layers of the shell ablate and expand outward, whereas the inner layers are compressed inwards. The center of mass of the imploding target shell is shown in red.

The implosion of the shell and the creation of a coronal plasma are shown in Figure 8. In Figure 8(a), a raytrace plot of the shell is shown near the start of the laser pulse when the shell is close to its starting position. The red lines represent the incoming rays from a ring-four laser beam. The black contours are density contours, and the green region shows the position of the shell. Figure 8(b) shows the shell at 2.8 ns, over halfway into the laser pulse. This plot shows the implosion of the optimum design with phase plates. The two plots provide a comparison between the starting shell and the shell when it has imploded halfway, and show that the shell has maintained its uniformity through 2.8 ns.

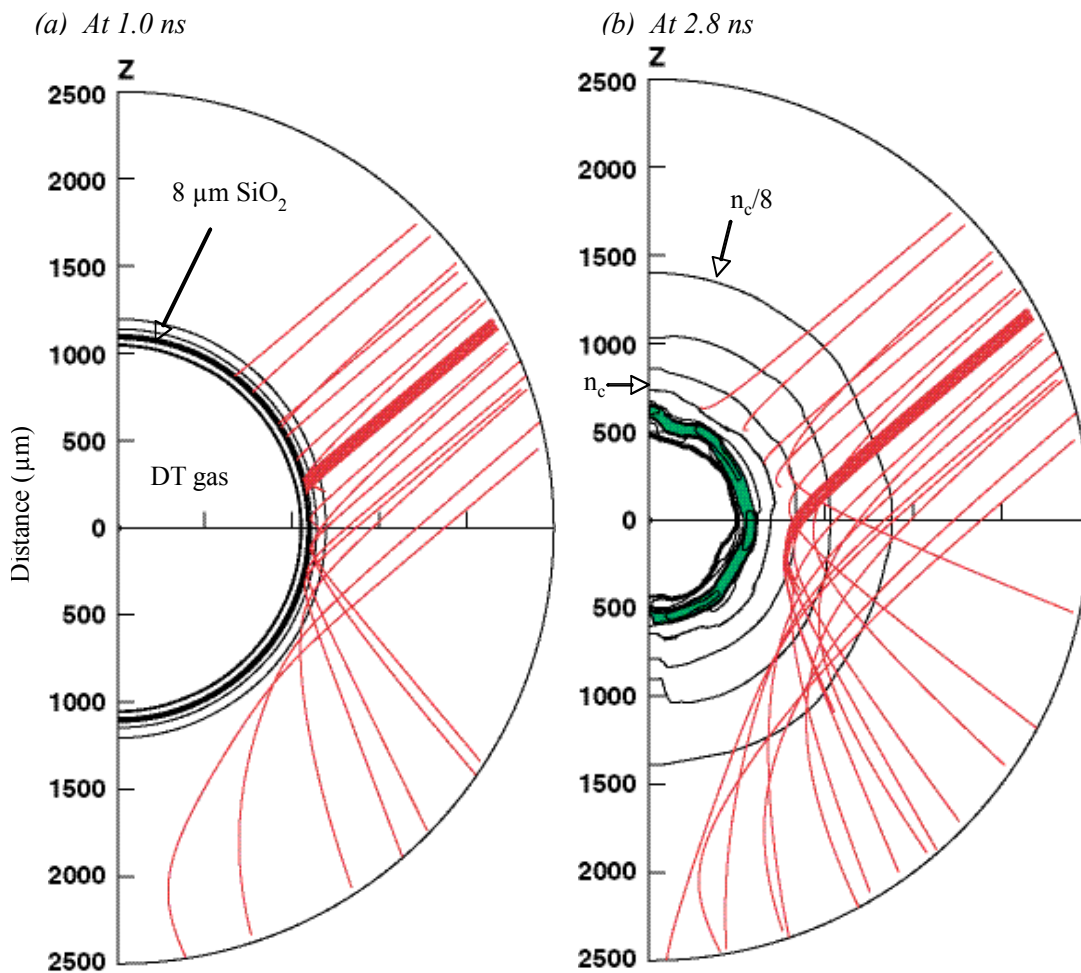


Figure 8. (a) A raytrace plot at 1.0 ns, near the start of the laser pulse. (b) A raytrace plot at 2.8 ns, when the shell (green) has imploded halfway. These plots show representative rays of ring 4 and some density contours. The design used for this simulation was the design with phase plates.

The importance of optimizing the designs is shown in Figure 9. In Figure 9(a), all of the beams are pointed to the center of the target and the defocus is 3.5 cm for all of the beams. The distortion in the shell at 2.8 ns is obvious as the shell forms an ellipse with semi-axes of $400\ \mu\text{m}$ and $750\ \mu\text{m}$. The ratio of velocities between the poles and the equator is 1.7 to 1 at 2.8 ns. Figure 9(b) shows the optimum design without phase plates at the same time. Raytrace plots such as Figures 8 and 9 show where each ring of beams hits the target, how well the shell maintains uniformity as it implodes, and where distortions in the shell occur.

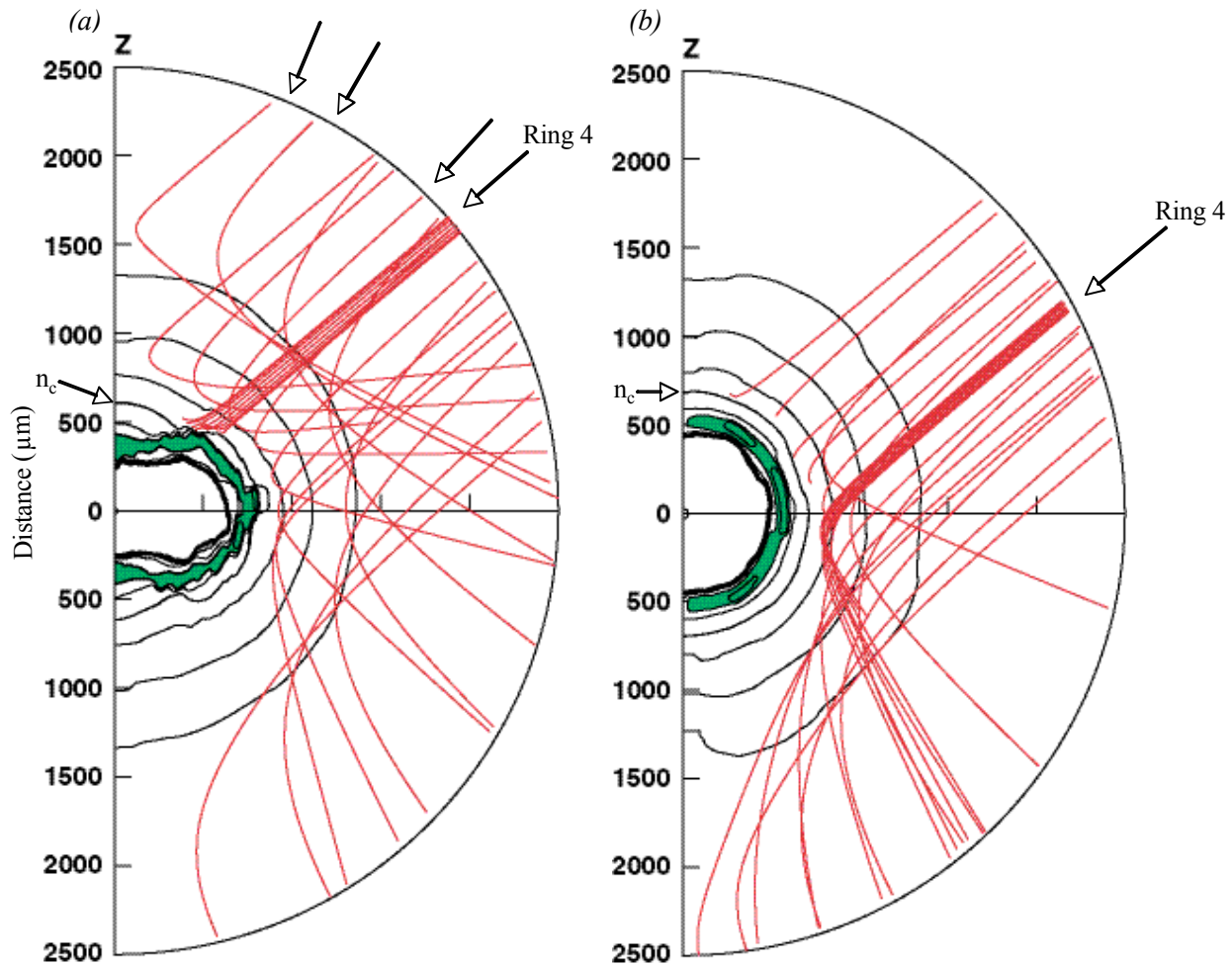


Figure 9. A comparison of two SAGE raytrace plots at 2.8 ns. (a) shows the implosion when the design has not been optimized, with all beams pointed to the center of the target. There is significant distortion in the shell. (b) shows the implosion when the design is highly optimized, and the shell maintains its uniformity. The optimized design used for (b) was the design without phase plates.

The two optimum designs, illustrated in Figures 8(b) and 9(b), were developed after numerous simulations using SAGE. SAGE provides parameters enabling the user to adjust the beam profiles. Although the accuracy to which SAGE calculates the out-of-focus beam profiles for NIF beams has not yet been experimentally determined, SAGE has accurately predicted the out-of-focus beam profiles for OMEGA beams. Figure 10 shows experimental data for the intensity of an OMEGA beam as a function of radius for best focus and two different defocus distances (5 mm and 10 mm). The theoretical calculations obtained from SAGE are plotted with the experimental data. The best focus was fit to a Gaussian of order $n=7$ [$I \propto \exp-(r/r_0)^n$ with $r_0=380 \mu\text{m}$], from which SAGE calculated the out-of-focus beam profiles. The accuracy to which SAGE calculates the out-of-focus profiles is excellent. It is reasonable to assume that SAGE will calculate the out-of-focus profiles of NIF beams to a similar degree of accuracy.

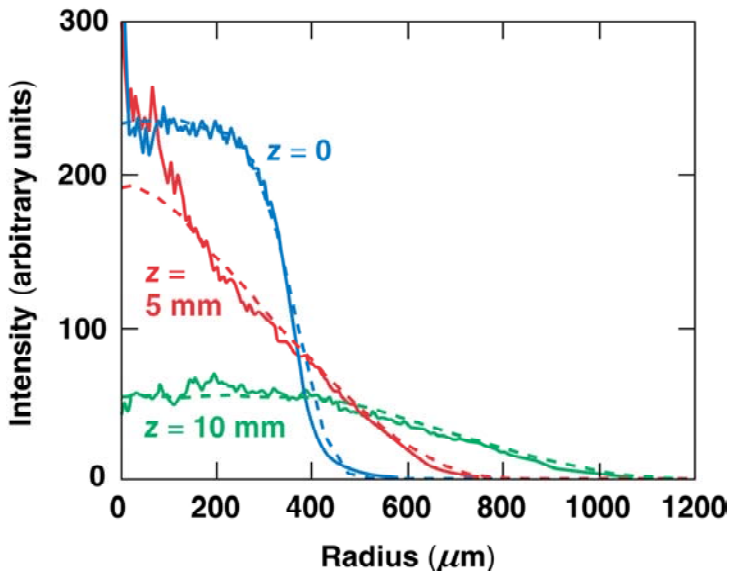


Figure 10. Graphs of intensity versus radius of an OMEGA beam at best focus ($z=0$) and for two defocus distances ($z=5$ mm and 10 mm). The solid lines correspond to experimental data and the dashed lines correspond to SAGE simulations.

4. Optimization Process and the Optimized Designs

The goal of the optimization process was to develop the design that would cause the shell to implode with the greatest degree of uniformity. Specifically, a design was sought that produced the lowest deviation of shell radius at a late time into the pulse (2.8 ns), just before the time of peak compression (see Figure 7). The optimization process involved running and

analyzing several hundred hydrodynamic simulations with different combinations of focusing and pointing parameters for each beam. The parameters that were varied included the shift, the defocusing distance, and the split-quad y -shift and z -shift for each ring of beams. The choice of run parameters came from analyzing the sensitivities to various parameters and from experimenting with the effects of varying different parameters. The main analysis was based upon plots of the center-of-mass radius versus angle from the vertical axis for different times (see Figure 11) with some guidance coming from raytrace plots. Plots of the center-of-mass radius show the areas of significant distortion. Figure 11(a) shows an example for an unoptimized design, which is to be compared with Figure 11(b) for the optimized design with phase plates. In Figure 11(a), the prominent bumps shown were typical of unoptimized designs. The level of uniformity decreases over time as slight distortions are magnified. In this example, the equator is particularly underdriven, resulting in a substantial bump there. The solution to this problem was a slightly tighter focus on the equator, to produce more equatorial drive. The other bumps are the results of beam profiles having relatively steep edges as in the top and bottom

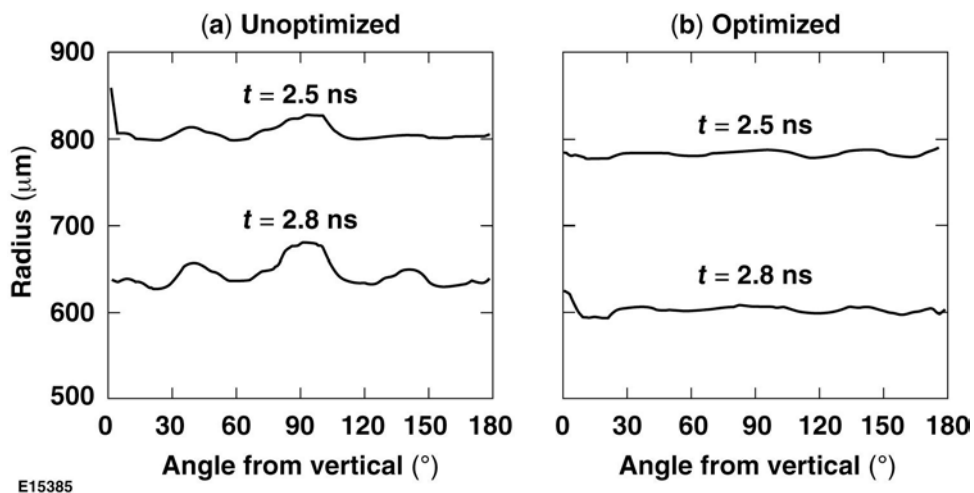


Figure 11. The center-of-mass radius plotted versus angle θ from the z -axis for unoptimized (a) and optimized (b) runs for the design with phase plates. These plots show which areas of the shell are receiving either too much drive or too little drive. In going from (a) to (b), the drive at the equator needed to be strengthened and the edges of rings three and four needed have a smoother overlap.

portions of Figure 5(d). When the edges of beams are steep, it is difficult to obtain equal amounts of drive at angles where the beams overlap. The solution to this was to increase the split-quad Δz shift on rings three and four slightly. Also, the simulation code sometimes produced some numerical noise such as the false peaks at $\theta=0^\circ$ at 2.5 ns in Figure 11(a) and at 2.8 ns in Figure 11(b), but these were easy to identify and did not affect the overall optimization process. Overall the simulations showed consistent behavior as laser parameters were varied.

The final set of parameters for the design with phase plates are shown in Table 1; the parameters for the design without phase plates are in Table 2. These tables contain all the specifications needed to implement these designs on the NIF. Parameters of particular interest are the defocus distances and the split-quad shifts. As is evident, the defocus distance varies for the four rings, with the smallest defocus distance on ring four. This is to provide the extra drive needed at the equator by increasing the intensity of those beams. In the design with phase plates, split quads are used on rings three and four. For ring four, this smoothes out the steeper drop-off of intensity that would otherwise be present from the smaller defocus [compare Figures 5(d) and 6(d)]. The parameters for the design without phase plates are very similar, with the exception of the split quads. For this design, rings two, three, and four all require split quads. Without phase plates to spread the beam energy, the intensity drops off very quickly at the edge of the beam. For the design without phase plates, the split quad shifts are significantly larger than for the previous design. This provides the needed shift to alter the steep drop-off in beam intensity to a more gradual rate of decrease of intensity. The more gradual rate of decrease makes it easier to overlap the individual beams to provide the most uniform irradiation of the target.

Table 1. Beam parameter specifications for the optimum design using indirect-drive phase plates.

	Angle	Pointing Shift	Defocus Distance	Phase Plate	Split Quad Z-Shift	Split Quad Y-Shift
Ring 1	23.5°	50 μm	3.0 cm	Inner	----	----
Ring 2	30.0°	159 μm	3.5 cm	Inner	----	----
Ring 3	44.5°	250 μm	3.5 cm	Outer	212 μm	141 μm
Ring 4	50.0°	494 μm	1.7 cm	Outer	247 μm	155 μm

Table 2. Beam parameter specifications for the optimum design without phase plates.

	Angle	Pointing Shift	Defocus Distance	Split Quad Z-Shift	Split Quad Y-Shift
Ring 1	23.5°	53 μm	3.0 cm	----	----
Ring 2	30.0°	165 μm	3.5 cm	283 μm	458 μm
Ring 3	44.5°	250 μm	3.5 cm	283 μm	458 μm
Ring 4	50.0°	494 μm	1.7 cm	283 μm	458 μm

Both of these designs produced excellent shell radius uniformity. The design using phase plates had a root-mean-square deviation of radius (ΔR_{rms}) of approximately 4 μm at 2.8 ns, when the shell has imploded to a radius of 600 μm , half of its initial radius. The design without phase plates performed nearly as well, giving a root-mean-square deviation of radius of approximately 6 μm at the same time. Uniformity of velocity is also necessary to produce good compression. These designs produce uniformity of velocity to approximately 2% (rms) for the phase plate design and 4% (rms) for the design without phase plates.

The sensitivity of the designs to pointing errors has been explored. Ring four is the ring most sensitive to pointing errors because of the tighter focusing. The sensitivity to mispointings of this ring is shown in Figure 12 for the two designs. These plots show the ΔR_{rms} of pointing error in the worst case scenario, where all of the ring 4 beams are mispointed in the same direction. The values on the x-axis are the pointing errors relative to the optimum shift for ring four (494 μm). Some short-scale structure resulting from numerical noise in the simulations is

apparent very close to the optimum pointings. However, the graphs clearly show only a slight reduction of uniformity for errors in the $\pm 50 \mu\text{m}$ range. The NIF pointing specification is $50 \mu\text{m}$ and pointings accurate to within $30 \mu\text{m}$ have been demonstrated¹¹. Therefore, the pointing on the NIF is more than adequate to produce good uniformity using these designs.

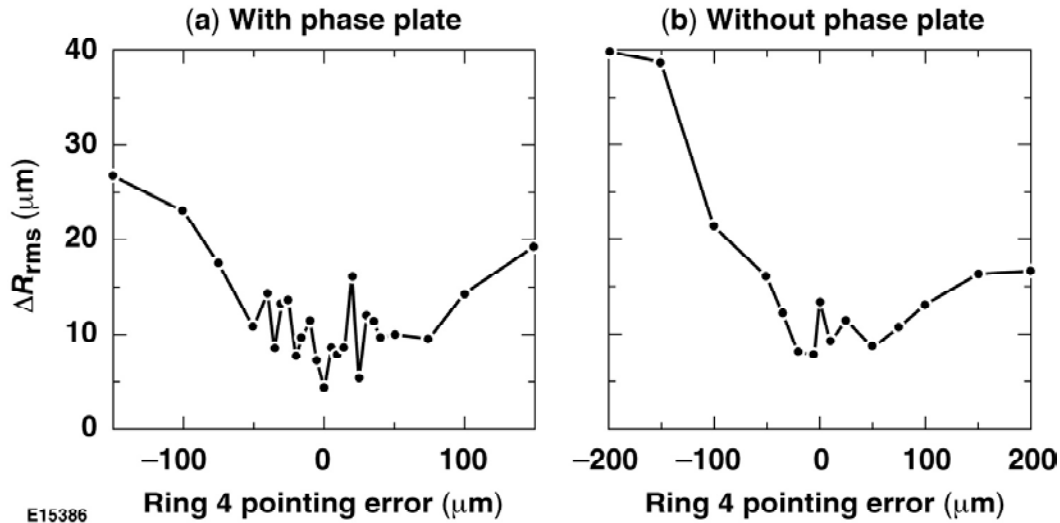


Figure 12. Sensitivity of the rms radius deviation at 2.8 ns to pointing errors of ring four from the optimum design in (a) the design with phase plates and (b) the design without phase plates.

5. Conclusion

Two experimental designs, including beam focus and pointing parameters, have been developed using hydrodynamic simulations to provide optimal implosion uniformity for directly-driven DT-gas-filled glass shells on the NIF. The development of these two designs makes it possible to carry out spherical implosions on the NIF as soon as all 192 beams are operational. In particular, high-neutron-yield implosions are possible on the NIF before the NIF is ready for ignition experiments. The availability of both a design using the NIF indirect-drive phase plates and a design using no phase plates allows for more flexibility according to what is available on the NIF at the time. These designs are necessary for initial experiments to test the NIF neutron diagnostic systems and will also enable direct-drive implosion experiments to be carried out much sooner than would otherwise be possible.

6. References

1. J. Nuckolls *et al.*, “Laser Compression of Matter to Super-High Densities: Thermonuclear (CTR) Applications,” *Nature* **239**, 139 (1972).
2. J. D. Lindl, “Development of the Indirect-Drive Approach to Inertial Confinement Fusion and the Target Basis for Ignition and Gain,” *Phys. Plasmas* **2**, 3933 (1995).
3. S. Skupsky *et al.*, “Polar Direct Drive on the National Ignition Facility,” *Phys. Plasmas* **11**, 2763 (2004).
4. R. S. Craxton *et al.*, “Polar Direct Drive: Proof-of-Principle Experiments on OMEGA and Prospects for Ignition on the National Ignition Facility,” *Phys. Plasmas* **12**, 056304 (2005).
5. J. A. Marozas *et al.*, “Polar-Direct-Drive Simulations and Experiments,” *Phys. Plasmas* **13**, 056311 (2006).
6. R. S. Craxton and D. W. Jacob-Perkins, “The Saturn Target for Polar Direct Drive on the National Ignition Facility,” *Phys. Rev. Lett.* **94**, 095002 (2005).
7. Y. Kato *et al.*, “Random Phasing of High-Power Lasers for Uniform Target Acceleration and Plasma Instability Suppression,” *Phys. Rev. Lett.* **53**, 1057 (1984).
8. T. J. Kessler *et al.*, “Phase Conversion of Lasers with Low-Loss Distributed Phase Plates,” in *Laser Coherence Control: Technology and Applications*, edited by H. T. Powell and T. J. Kessler (SPIE, Bellingham, WA, 1993), Vol. 1870, p. 95.
9. P. W. McKenty, Laboratory for Laser Energetics, private communication (2006).
10. R. S. Craxton and R. L. McCrory, “Hydrodynamics of Thermal Self-Focusing in Laser Plasmas,” *J. Appl. Physics.* **56**, 108 (1984).
11. R. A. Zacharias *et al.*, “National Ignition Facility Alignment and Wavefront Control,” in

Optical Engineering at the Lawrence Livermore National Laboratory II: The National Ignition Facility, edited by M. A. Lane and C. R. Wuest (SPIE, Bellingham, WA, 2004).

Vol. 5341, p. 168.

**Improved Laser Damage Resistance of Multi-Layer Diffraction Gratings
Vapor-Treated with Organosilanes**

Zuzana Culakova

**Improved Laser Damage Resistance of Multi-Layer Diffraction Gratings
Vapor-Treated with Organosilanes**

Zuzana Culakova

Brighton High School
Rochester NY, 14618

Advisor: Kenneth L. Marshall

Laboratory for Laser Energetics
University of Rochester
Rochester, NY
August 2006

Abstract

Multi-layer dielectric gratings are used in high power laser systems to compress laser energy pulses. The final power of these short pulse petawatt class systems is limited by the laser damage resistance of the optical components in the system, especially the diffraction gratings. This work was motivated by the previous discovery that vapor-treatment of gratings with hexamethyldisilazane (HMDS) can increase the damage threshold. Gratings were laser damage tested, and then a simple room temperature vapor-deposition technique was used to coat them with several different disilazane compounds. The gratings were then damage tested again to determine if an increase in damage threshold had occurred. The laser-induced damage threshold of an HMDS-treated grating increased by 4.5% in a 1-on-1 damage test, while that of a tetramethyldisilazane-treated grating increased by 16.5% in an N-on-1 damage test. Both the N-on-1 and 1-on-1 damage thresholds of a bis-(trifluoropropyl)tetramethyldisilazane-treated grating increased, by 4.8% and 5.3 % respectively. Such increases in laser damage threshold are unprecedented and counterintuitive because it is widely accepted that the presence of organic material or coatings on the surfaces of optical substrates decreases their laser damage resistance. The results are especially encouraging since they were obtained on samples of sub-optimal quality. The next logical step is to attempt to confirm this effect on high-quality, freshly cleaned grating samples.

1. Introduction

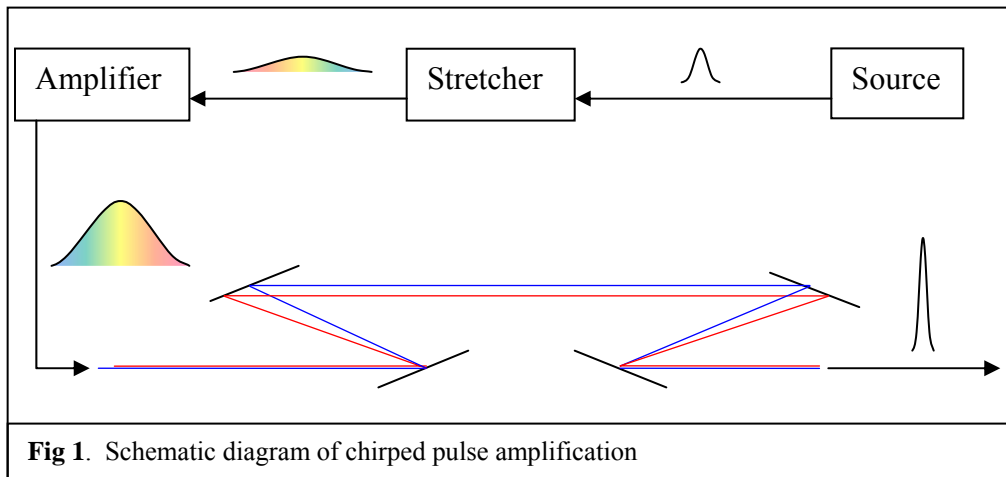
High energy petawatt (HEPW) laser systems are capable of producing beams of unprecedented intensities for high energy density physics experiments. In a number of

countries around the world, these systems are being built to develop laser fusion as an alternate energy source. Laser fusion uses lasers to compress and heat targets containing hydrogen isotopes, initiating fusion - the combination of nuclei to form helium and energetic neutrons. The current goal of laser fusion research is to reach and exceed “break even”- the point at which the amount of fusion energy produced equals the energy consumed by the laser. Two HEPW systems, Japan’s GEKKO Petawatt and the United Kingdom’s Vulcan Petawatt are currently in operation, while several more, including the OMEGA Extended Performance (EP) laser, are under construction or in planning¹.

OMEGA EP is an addition to the existing fusion laser system, OMEGA, at the University of Rochester Laboratory for Laser Energetics (LLE). The OMEGA EP system, expected to begin operation in 2008, will have two beamlines equipped with a short pulse (1 ps to 100 ps) capability at a wavelength of 1053 nm. These two beams can be directed into the OMEGA laser’s target chamber to be used for fast ignition experiments, which use a pulse of energetic electrons to heat the compressed fuel, thus igniting the fusion reaction², and to produce short pulses of x rays to “backlight” imploding fusion targets for diagnostic purposes. The short-pulse beams interacting with plasmas produced by longer pulses will also be used to study high energy density physics, such as high-intensity laser-matter interactions, in OMEGA EP’s target chamber^{3,4}.

The short pulses are created by chirped pulse amplification (CPA)⁵, as shown in Figure 1. To amplify the laser pulse without damaging the amplifier, a short pulse from the source is first chirped, or stretched into a longer, lower-power pulse in which the longer wavelengths travel at the front. The pulse is amplified and then compressed by a

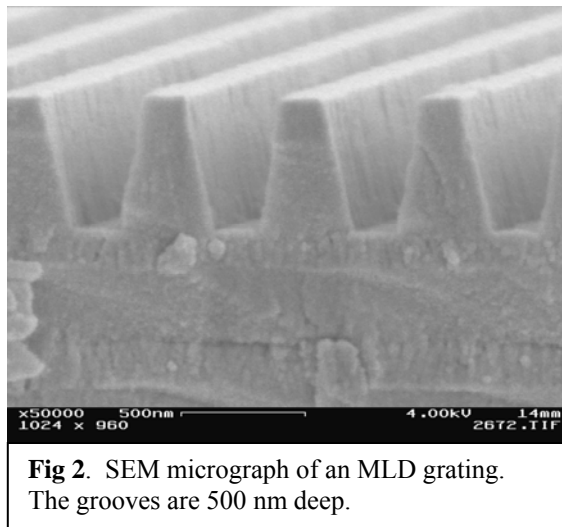
series of four diffraction gratings. The compression occurs as the longer wavelengths at the front of the amplified pulse are diffracted more and therefore forced to travel longer paths than the shorter ones, allowing all wavelengths in the pulse to arrive at the fourth grating at the same time. Because the fourth grating in the series experiences the shortest pulse length it subject to the highest fluence, or power per unit area. The damage resistance of this last grating is the limiting factor on the amount of energy that can be obtained in the compressed laser pulse. Consequently, this last grating must not only be of very high optical quality, but it must also have an exceedingly high laser damage threshold. The laser damage resistance of previous-generation gold diffraction gratings was around 0.5 J/cm^2 while the minimum requirement for the gratings to be used in OMEGA EP is around 2.7 J/cm^2 for a pulse length of 10 ps^4 .



Multi-layer dielectric (MLD) diffraction gratings (see Figure 2) are composed of reflective stacks of thin (subwavelength) SiO_2 and HfO_2 layers which differ in dielectric constant. Diffraction of light is caused by the grooves etched into the top SiO_2 layer. MLD gratings are currently used because of their much higher laser-induced damage thresholds in comparison to previous gratings⁶. However, because the damage resistance

of the last grating is the limiting factor on the energy of the laser, new ways to increase the damage threshold are desirable.

In preliminary experiments by the Optics and Imaging Sciences group at LLE, gratings were exposed overnight to the organosilane compound



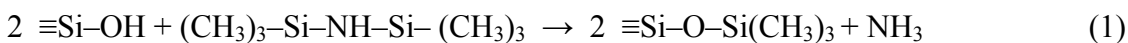
hexamethyldisilazane, (HMDS), which is used in the semiconductor industry as a coupling agent to increase the adhesion between a silica wafer and a photoresist. Organosilanes are compounds composed of silicon atoms carrying up to four different carbon-containing functional groups. MLD gratings that were vapor treated with HMDS reproducibly demonstrated increases of >20% in laser damage thresholds⁷. This increase in damage resistance, known as “laser hardening,” was unexpected and counterintuitive, because conventional wisdom dictates that the presence of organic materials on optical components will lead to reduced laser damage thresholds. The goal of this investigation was to assess the reproducibility of the phenomenon, find the necessary conditions for the reaction, and identify whether the laser hardening effect is unique to HMDS.

During this investigation, candidate organosilanes were used to vapor treat glass slides to assess their potential for treating diffraction gratings. The chemistry of the reaction of the compounds with silica surfaces is described in Section 2. Estimates of the necessary exposure time for a saturated coating were obtained by measuring the water contact angle on the surfaces, as summarized in Sections 3 and 4. Diffraction grating

samples were damage tested before and after treatment with the most promising organosilanes, as described in Section 5. Section 6 details improvements in the laser-induced damage thresholds that were found as a result of this treatment.

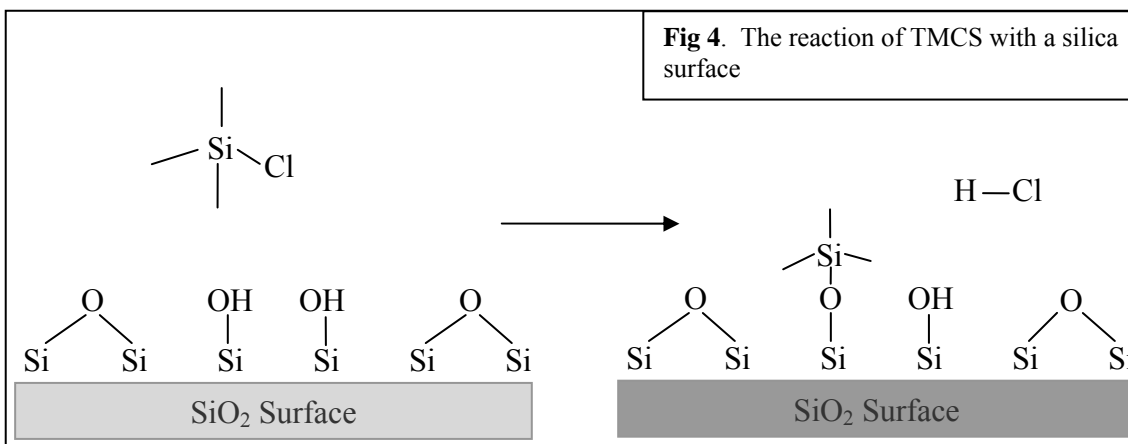
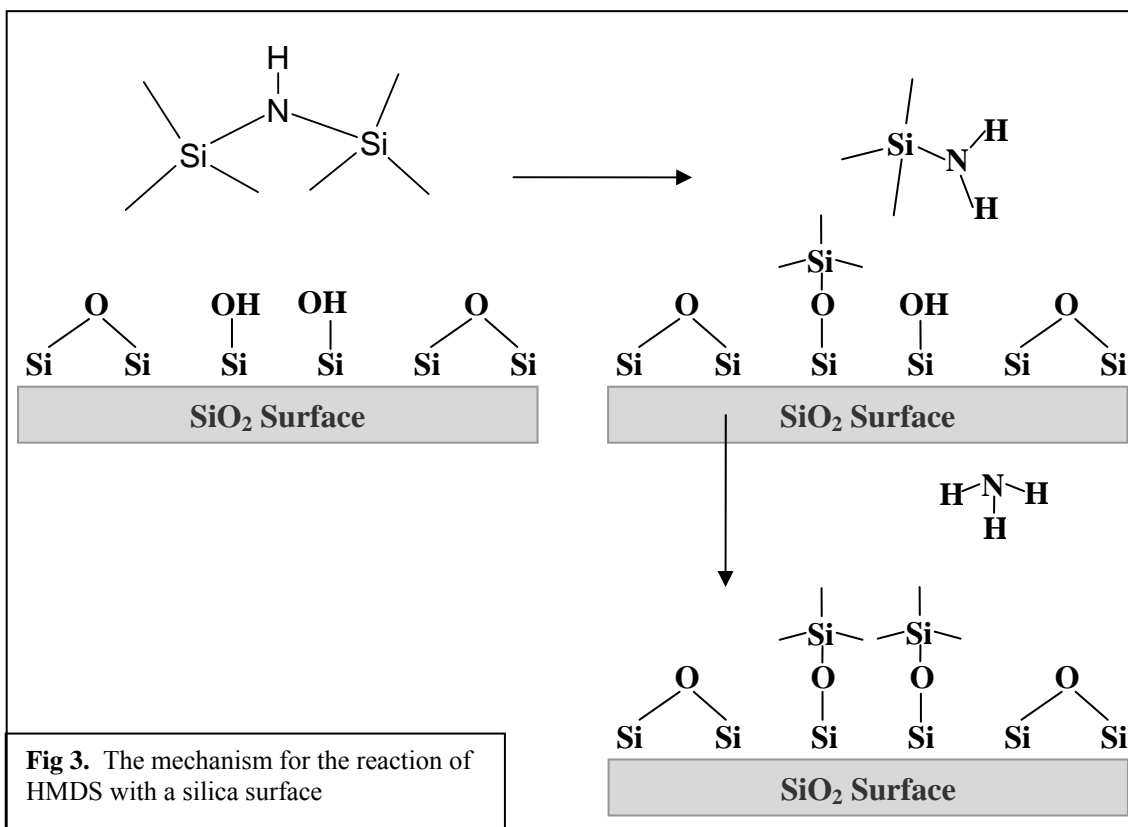
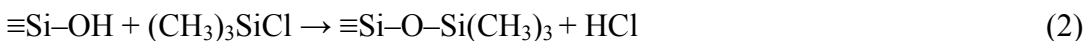
2. Chemistry of Organosilanes

Two different classes of organosilanes that bond easily to silica surfaces were identified. Both disilazane (silamine) and chlorosilane compounds are widely used to change the surface chemistry of silica capillary columns for gas chromatography by bonding organic functional groups with widely different polarities to the inner surface of the column⁸. Silylation occurs as the compounds react with and replace hydroxyl groups on the silica surface. The reaction utilizes the natural vapor pressure of the chemicals and proceeds in the vapor phase at room temperature and pressure. This feature makes vapor treatment with these chemicals simple, and because it does not require heat, it avoids the risk of shattering the sensitive MLD gratings by thermal shock. The disilazane compounds can react completely in a two-step mechanism with the surface silanols (see Figure 3). In this example, the HMDS first reacts with a surface hydroxide group to attach one trimethylsilane group to the substrate surface to form trimethylaminosilane, which further reacts with the surface to deposit a second trimethylsilane group, which forms ammonia as a byproduct. The overall reaction with HMDS can be written as⁹:



The chlorosilane compounds react via a simpler single step reaction shown in Figure 4.

For example, a trimethylchlorosilane (TMCS) molecule interacts with the surface silanols to deposit a single trimethylsilane group, forming hydrogen chloride gas as a byproduct as shown in the equation below¹⁰:



3. Silylation Experiments

Initial experiments investigating the reactivity of different compounds with a silica surface were performed with each candidate organosilane. Because of a very limited supply of grating substrates, initial silylation experiments were carried out on cleaned, baked dry microscope slides. The slides were treated with HMDS, tetramethyldisilazane (TMDS), 1,3-di-n-octyltetramethyldisilazane (OTMDS), bis(trifluoropropyl)tetramethyldisilazane (FTMDS) and TMCS. The HMDS was used to replicate the original experiment, the TMDS was of interest because of its close structural similarity to HMDS, and the OTMDS was chosen to investigate the effect of a longer hydrocarbon chain on the “hardening” effect. The effect of the trifluoropropyl groups in the FTMDS would show whether the laser hardening was unique to silanes with strictly hydrocarbon end groups. Finally, treatment with TMCS deposits the same trimethylsilyl groups on to the surface as does treatment with HMDS. Treatment with TMCS would therefore identify whether the silylation of the surface or the mechanism of the treatment is responsible for the increase in damage threshold. The effect of elevated temperature (50 C) on the silylation with HMDS was also investigated.

A simple chemical vapor deposition technique at room temperature was used to treat the slides with the silanes for different amounts of time. Samples were placed in a chamber with an open vial containing approximately 2

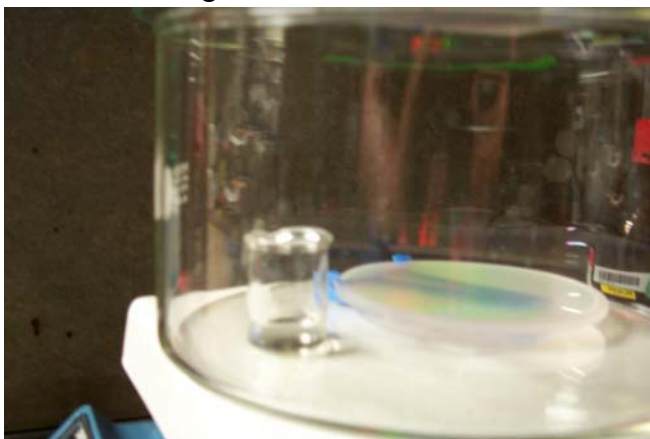
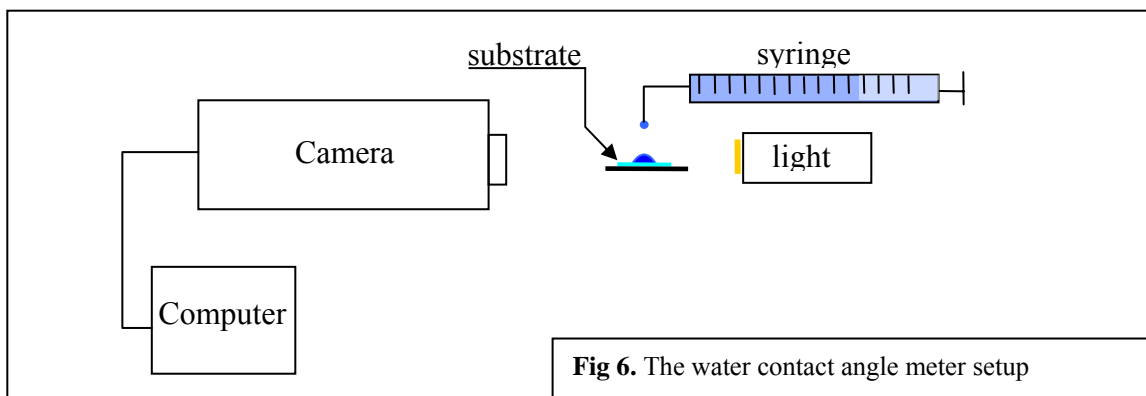


Fig 5. General silylation setup used for all experiments showing the treatment of a grating sample (flat, right) with FTMDS (beaker, left).

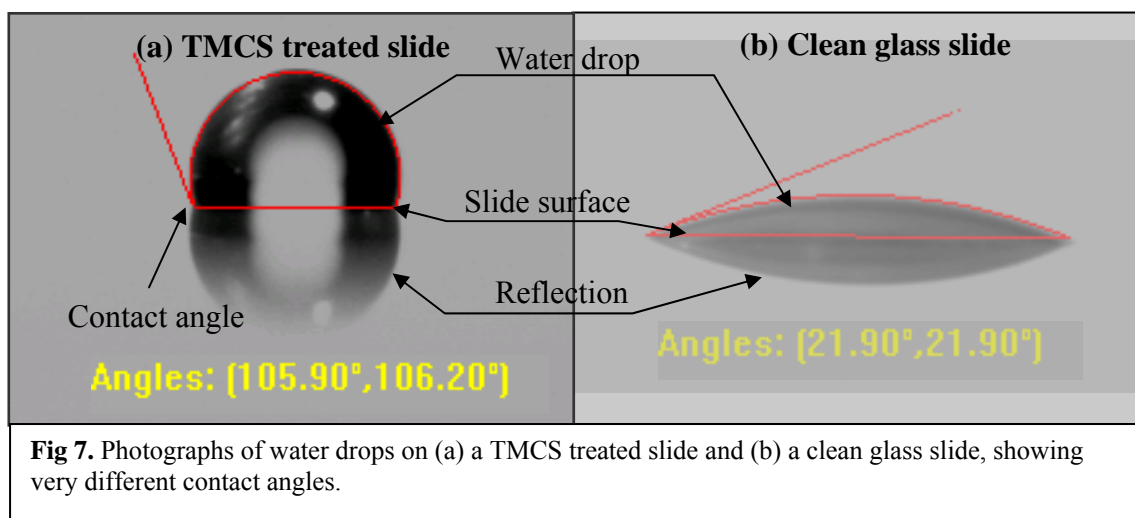
ml of each organosilane for 2, 4, 6, 22, and 30 hours, using the setup shown in Figure 5. Control samples consisted of both a clean, untreated glass slide and a slide assumed to be fully silylated, prepared by saturating the slide with the given compound. For the elevated temperature trials, the hotplate that was used as the work surface to support the substrates and the container holding the organosilane was turned on and regulated at 50°C.

The degree of silylation, or the amount of silane that had been deposited on the slide, was tracked by measuring the water contact angle using a VCA 2500XE contact angle instrument (AST Products, Inc), as shown schematically in Figure 6. The contact angle of a droplet of water on a surface is a measure of the hydrophobicity, or the free energy, of a surface. To measure the contact angle, a drop of water was deposited on to the substrate, and a digital photograph of the droplet profile was taken immediately.



Examples of two photographs with calculated angles, one for a TMCS treated slide and one for a clean glass slide, are shown in Figure 7. In the photographs, the droplet is outlined by the dark band, where light is refracted away from the camera. Software is used to calculate the angle between the tangent to the edge of the droplet touching the surface, and the surface. The clean glass slide exhibits a very low contact angle, because the hydrophilic hydroxyl groups on the surface cause the polar water drop

to spread and flatten across the slide. Nonpolar organosilane groups deposited onto a silica surface render it more hydrophobic, repelling the water droplet and making it bead up more, which increases the contact angle. Increased surface silylation (i.e. greater density of organosilane groups deposited) increases the contact angle along with the hydrophobicity. Each reported contact angle is the average of at least five measurements taken on separate areas of the substrate.



4. Slide Silylation Results

Figure 8 plots the contact angle against exposure time to show the level of silylation as a function of time. HMDS-treated samples were fully silylated after a 30 hour exposure, as were the samples exposed to TMDS. Due to their much lower vapor pressures, both OTMDS and FTMDS failed to fully silylate the slide during the 30 hour exposure period. However, the difference between 30 hour exposure FTMDS vapor treated sample and the fully silylated control was small. Because of the very low vapor pressure of OTMDS vapor treatment experiments will not be feasible unless an alternate method can be found to raise its vapor pressure (e.g., conducting vapor-phase exposure

under reduced pressure). Since developing such a method was beyond the scope of this work due to time constraints, only FTMDS was further evaluated.

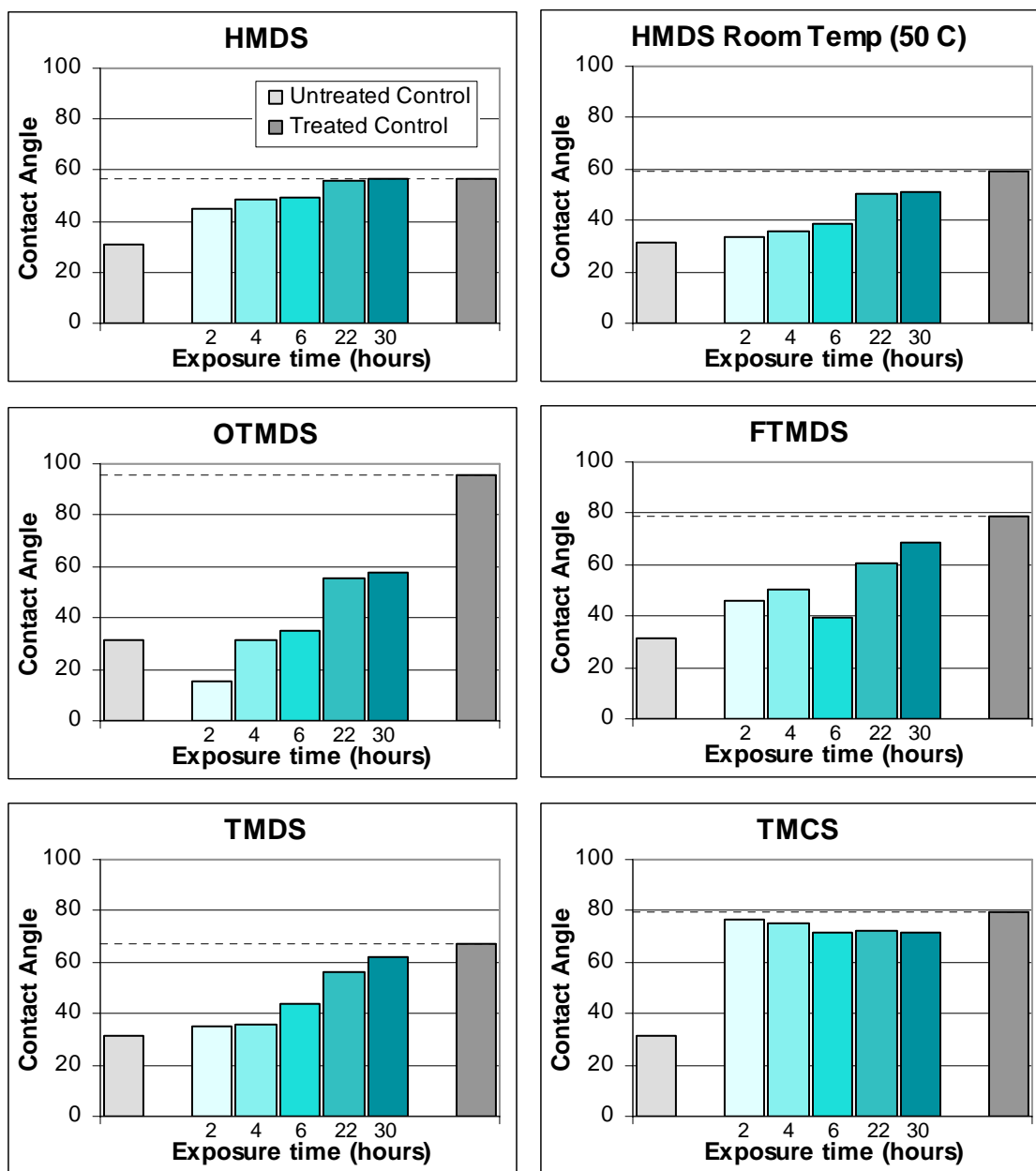
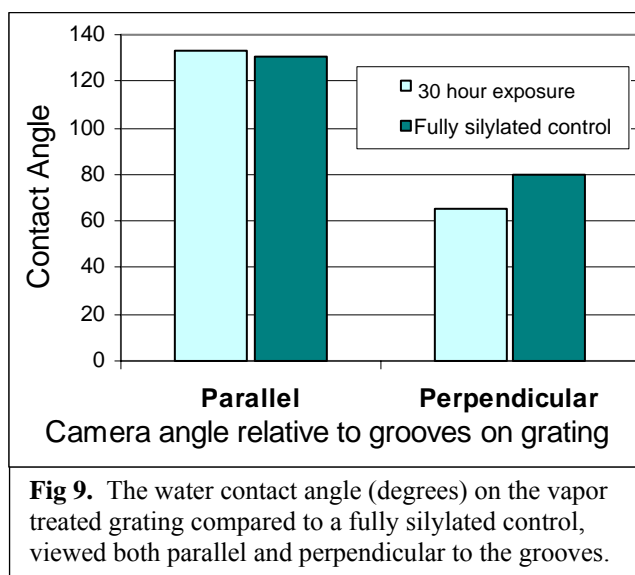


Fig 8. Contact angle as a function of exposure time for glass slides exposed to various silanes. Untreated controls are clean glass slides and treated controls are slides soaked in the silane. Because increased silylation increases surface hydrophobicity, the water contact angle is indicative of increased silylation.

The TMCS had by far the shortest silylation time of the compounds tested, reacting completely within two hours. This fast silylation rate was unsurprising because chlorine-containing organic compounds are associated with high reactivity. The resulting shorter silylation time would be more convenient as a treatment for the full-scale gratings. Treatment with TMCS also resulted in a higher contact angle than the HMDS, indicating that it was more effective at depositing a higher number of trimethylsilane groups per unit area, perhaps due to its smaller molecular size. However, treatment with TMCS proved to be somewhat impractical for use on the gratings. The reaction of TMDS with the substrate produces HCl vapor, which forms deposits on all exposed glass surfaces to produce a cloudy, frostlike layer. Upon removal from the chamber, the HCl quickly evaporates, but an oily sheen removable with a distilled water wash remained on the surface. Application of TMCS to the MLD gratings would require an extra process step, increasing the chance of damage to the delicate gratings. Because of this complication, the chlorosilane family was not investigated further.

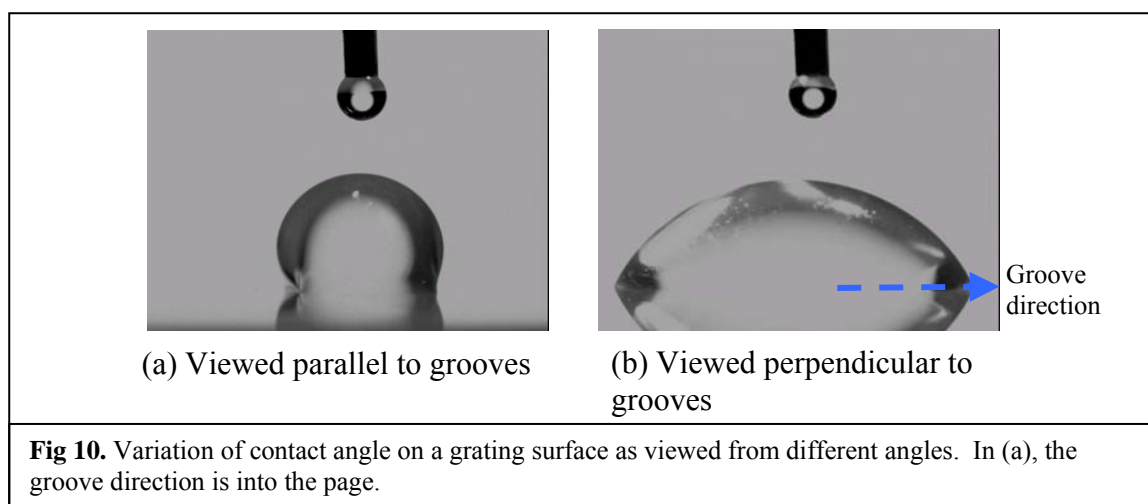
Water contact angle

measurements were then attempted on a clean, untreated grating, but could not be obtained because the water droplets ran down the grooves. The grating sample was exposed to HMDS for 30 hours, and the water contact angle was then measured successfully. Treatment of the



grating surface increased its hydrophobicity, which prevented the droplets from spreading into the grooves. This observation is a clear indication that silylation had occurred. As demonstrated in Figures 9 and 10, the contact angle measurements depend on the angle of the camera relative to the direction of propagation of the grooves on the grating.

Measurements obtained with the camera perpendicular to the grooves are much lower than when the image is taken parallel to the grooves. The measurements for water contact angle on the vapor-treated grating were similar to those obtained on a fully silylated grating, and indicated that as expected from the microscope slide experiments, silylation had occurred.



5. Damage Threshold Experiments

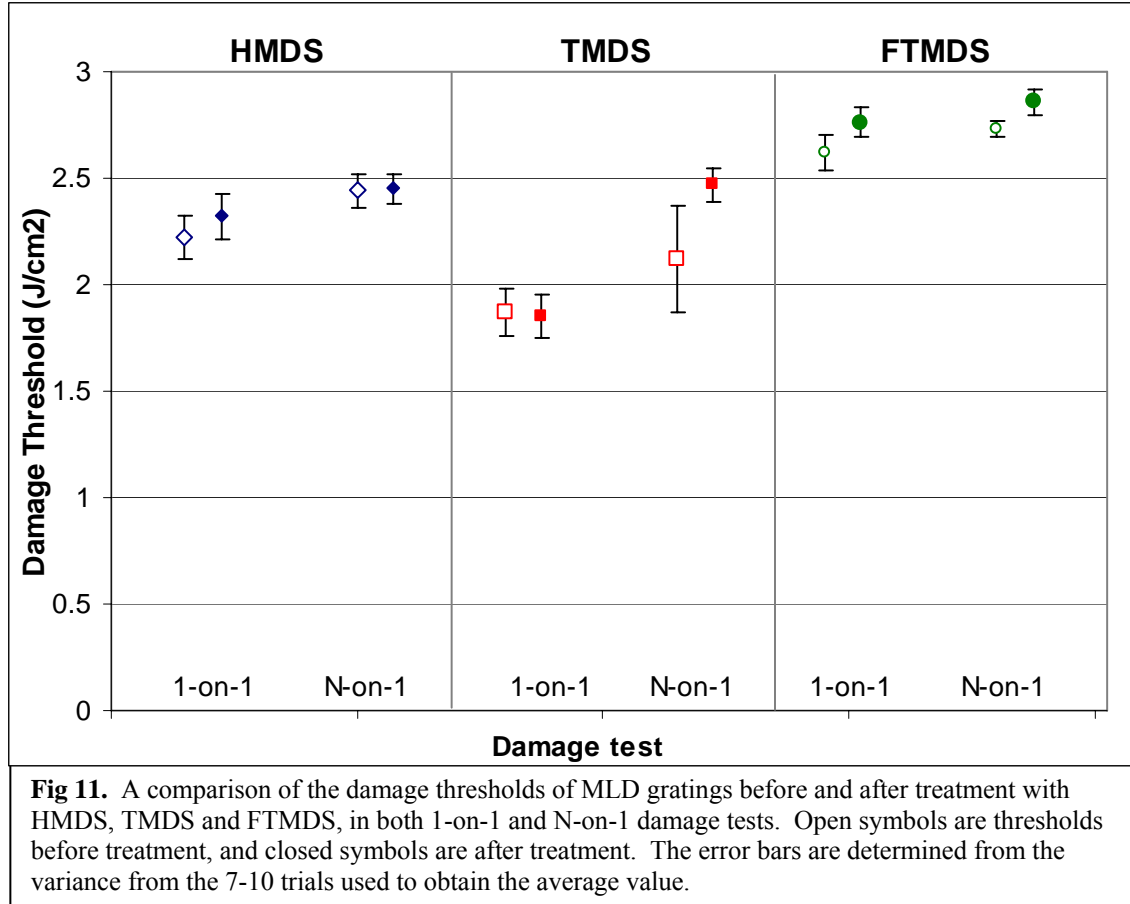
Untreated diffraction grating samples were damage tested prior to silylation. Because of limits on grating availability, the samples used were recycled from previous experiments, and had been cleaned months earlier and stored. The cleaning process uses high temperature immersion in acid piranha solution (H_2SO_4 and H_2O_2).

Both 1-on-1 and N-on-1 laser-induced damage tests were performed. A 1-on-1 damage test irradiates separate sites with increasing energies until visible damage occurs, while an N-on-1 damage test irradiates a single site at progressively greater intensities until damage occurs. The second test is important because of a phenomenon called “laser conditioning,” in which a higher laser damage threshold is obtained by successively irradiating the surface at increasing energies. The tests were performed at the LLE damage test facility, using a laser operating at 1054 nm with a pulse width of 10 ps and a spot size of 370 microns.

The samples were then vapor-treated for 30 hours with HMDS, TMDS, and FTMDS. Because of limitations in grating availability, time, and the availability of the damage test facility, the three organosilanes that were found to be the most promising from the initial silylation experiments were chosen to be tested. Based on both the microscope slide experiments and a trial exposure of one grating, 30 hours was the necessary time to obtain complete or almost complete silylation.

6. Damage Test Results

The results of the damage tests are shown in Figure 11. The TMDS treated sample showed the largest increase, 16.5%, from 2.12 to 2.57 J/cm² in the N-on-1 damage test, but the 1-on-1 damage threshold was virtually unaffected. Conversely, the 1-on-1 damage threshold of the HMDS treated sample increased 4.5 %, while the N-on-1 damage test remained almost constant. The FTMDS treated grating was the only one to show increases in both damage thresholds (approximately 5% for each) though the increase in the 1-on-1 test was within the margin of error.



7. Discussion

Vapor treatment with the organosilane compounds is preferable over other surface treatment options, such as spin-coating. Spin-coating is a commonly used physical deposition technique that involves spinning the substrate at up to several thousand rpm to evenly coat the substrate with a solution. The excessive handling required by this, and most other deposition processes, risks damaging the large, delicate optics; spinning such a substrate up to thousand rpm is risky at best. The vapor treatment reaction can be carried out with minimal equipment, minimal handling of the optics, and at room temperature and pressure. The process chemically bonds only a single monolayer to the surface of the substrate, eliminating the need to control the coating thickness, the coating

time, or the amount of chemical penetration into the porous surface. Because the vapor-deposition process inherently produces pure vapor that contacts the surface directly, the need to purify the chemicals before deposition is eliminated. Additionally, it would be relatively simple to implement because facilities exist to provide a similar vapor-treatment step (an ammonia hardening step of sol-gel anti-reflective optical coatings), although the toxicity and flammability of the organosilanes make them more difficult to work with.

Since Figure 11 shows that vapor treatment with all three chemicals caused increases in damage thresholds, it is now established that the “hardening” effect is not limited to HMDS. The increase in both damage thresholds obtained with the FTMDS treatment is also significant because it shows that the laser hardening phenomenon is not unique to disilazanes with only hydrocarbon groups, but applies to a wider class of compounds. An increase in both damage thresholds is desirable, because otherwise gratings would need to be conditioned before being exposed to peak intensities if the N-on-1 damage threshold were much higher than the 1-on-1 damage threshold. The large increase in the N-on-1 damage threshold obtained with the TMDS also makes it a good candidate for use.

Interestingly, this experiment did not reproduce the $> 20\%$ increases in damage threshold obtained in the preliminary trials. The reason for this is most likely due to the physical condition and cleanliness of the available gratings. Due to limited availability of gratings, only recycled samples from previous tests, of varying age and with different handling, etch, and cleaning processes were used. It is impossible to estimate magnitude of the effect of the condition of these “recycled” gratings on the results, and any increase

in damage threshold is therefore very encouraging. Since processing and cleaning methods are known to affect the damage thresholds of the gratings,¹¹ the history of the gratings used in further experiments should be as controlled as possible, and the gratings should be cleaned in acid piranha solution just prior to testing to make sure that all trace organic contamination has been removed. The effect of the history of the grating (such as the etch process used to make the grooves) on the hardening phenomenon should be investigated to see which processes have the greatest effect. Further study is needed to optimize treatment conditions such as time and temperature, and a wider range of organosilanes needs to be tested. In particular, TMCS should be tested because, despite the issue with the haze generated by the HCL byproducts, the faster exposure time and more complete silylation could ultimately make it more efficient to use than HMDS. The treatment would help determine whether the reaction mechanism of the disilazane family, or some other factor associated with the deposited organosilane groups, is responsible for the hardening effect.

A number of spectroscopy techniques, including Fourier transform infrared spectrometry and UV-visible-near IR spectroscopy, can be used to identify the mechanism responsible for the hardening. Surface studies of the gratings by electron microscopy or atomic force microscopy both before and after treatment, and after laser conditioning and damage testing could also provide information on maximizing the benefit of the treatment. Furthermore, the hardening effect can also be looked at as a way to revive gratings whose damage threshold is below acceptable levels, either immediately after fabrication or after use in the laser system. An increase of even $\sim 0.3 \text{ J/cm}^2$ in the

damage threshold, as was obtained with the TMDS, would be enough to make a marginal grating useable again, reducing the need for new gratings.

An additional benefit of the organosilane coatings studied here might be to protect the gratings of petawatt lasers against organic contamination. Trimethylsilylated MCM-41 capillary columns, used in gas chromatography, have demonstrated decreased adsorption of organic compounds in comparison to untreated columns¹². Because the chamber containing the gratings used for laser pulse compression is operated at very high vacuum, the volatility of organic materials that may be present in equipment and fixtures will be enhanced at the low operating pressure of the chamber (“outgassing”). These materials may redeposit on nearby optical elements subjected to petawatt peak power levels, including the gratings. This vapor-deposition process of residual volatile organic components is a major potential source of laser damage. If the gratings could be treated with a material that would either prevent deposition and absorption of volatile organics on the grating surfaces (or at least facilitate easy cleaning of the gratings), major cost savings could be realized in the operation of lasers such as OMEGA EP.

8. Conclusions

Hardening of multi-layer dielectric gratings used in high-energy petawatt class laser systems has been found to be possible by vapor-phase treatment of the gratings with a number of organosilane compounds. The process is relatively simple to implement, and could provide a way to increase the damage resistance of the gratings and ultimately allow for more powerful lasers. This work has shown an increase in damage resistance using three organosilane compounds. With further investigation on higher quality

samples and optimization of the process, it may be possible to implement the process on a larger scale.

9. Acknowledgments

I thank Mr. Marshall for the supervision and advice he provided me with throughout my project. I also thank the LLE damage test facility scientists and all other students and scientists in the Materials Lab and OIS for their help with using the facilities and equipment. I thank Dr. Craxton for choosing me to participate in this excellent program and for his interest and support. Finally, I thank the other program participants for making this summer amazing.

10. References

- ¹ J. D. Zuegel et al., *Laser Challenges for Fast Ignition*, Fusion Science and Technology, **49** Apr. 2006.
- ² M. Tabak et al., *Ignition and High Gain with Ultrapowerful Lasers*, Phys. Plasmas **1**, 1626 (1994).
- ³ C. Stoeckl et al., *High-energy Petawatt Project at the University of Rochester's Laboratory for Laser Energetics*, Fusion Science and Technology, **49**, Apr. 2006.
- ⁴ J. H. Kelly et al., *OMEGA EP: High Energy Petawatt Capability for the OMEGA Laser Facility*, J. Phys. IV France **133**, 75-80 (2006).
- ⁵ D. Strickland and G. Mourou, *Compression of Amplified Chirped Optical Pulses*, Opt. Commun. **56**, 219 (1985).
- ⁶ B. W. Shore et al., *Design of High-efficiency Dielectric Reflection Gratings*, J. Opt. Soc. Am. A/Vol. 14, No. 5/May 1997.
- ⁷ Marshall, Kenneth, Laboratory for Laser Energetics, personal communication (2006).
- ⁸ Reiner Anwender et al., *Surface Characterization and Functionalization of MCM-41 Silicas via Silazane Silylation*, J. Phys. Chem. B **104**, 3532-3544 (2000).

⁹ V. M. Gun'ko et al, *Mechanism and Kinetics of Hexamethyldisilazane Reaction with a Fumed Silica Surface*, Journal of Colloid and Interface Sciences **288**, (2000).

¹⁰ L. A. Belyakova and A. M. Varvarin, *Surface properties of silica gels modified with hydrophobic groups*, Colloids and Surfaces A: Physicochemical and Engineering Aspects **154**, 285-294 (1999).

¹¹ T. Kessler, *Damage-resistant Holographic Gratings* Unpublished report.

¹² X. S. Zhao and G. Q. Lu, *Modification of MCM-41 by Surface Silylation with Trimethylchlorosilane and Adsorption Studies*, J. Phys. Chem. B **102**, 1556-1561, (1998).

**Modeling Collisional Blooming and Straggling of the Electron Beam
in the Fast-Ignition Scenario**

Eric Dobson

Modeling Collisional Blooming and Straggling of the Electron Beam in the Fast Ignition Scenario

Eric Dobson
The Harley School
Advisor: Jacques Delettrez

Laboratory for Laser Energetics
University of Rochester
Summer High School Research Program
2006

Abstract

The motion and distribution of electrons in the plasma in the fast-ignition scenario are defined by three equations that describe the spread in the direction of motion (straggling), the spread in the direction perpendicular to the motion (blooming), and the amount of energy lost as the electron travels through the plasma. A program was written that models the distribution of the electrons in the plasma and tracks their energy deposition. This model treats the beam of electrons as many parallel beams of infinitesimal width that move in a straight line. When the blooming or straggling exceeds a certain value, each beam of electrons is split into multiple beams of different weights. The model was found to require exponentially more time and memory for greater degrees of accuracy and to be sensitive to small adjustments in the splitting algorithm. The results of this model applied to a test problem were found to be very similar to the analytic predictions, with errors ranging from ~2% to 11%.

Introduction

In conventional inertial confinement fusion, ignition occurs when one of the fusion products (alpha particles) created in a central hot-spot are stopped in the high density, cold fuel, causing a propagating burn. A proposed alternative ignition method, known as “fast ignition”, is to heat a part of the high density, cold fuel with a beam of relativistic electrons created by focusing a high-intensity laser into the target. The transport of these electrons is currently carried out with a straight-line model in which the electrons do not deviate from straight-line trajectories. In reality, the electrons undergo

straggling (different penetration depths) and blooming (spreading of the beam) because of collisions with the background plasma.

This report describes a mathematical model and how it is applied within the straight-line algorithm. The results are then compared to the predictions of the analytic computations done by Li and Petrasso.¹

Mathematical model

In this report we describe a method for accounting for straggling and blooming within the constraint of the existing straight-line model. As the electron beam travels through the target, the electrons collide with the plasma, depositing their energy, and changing their directions. This is described by the following expression², which is used in the existing model:

$$\frac{dE}{ds} = -\frac{2\pi_0^2 m_0 c^2 n_i Z}{\beta^2} \left[\ln \left(\frac{(\gamma-1)\lambda_D}{2\sqrt{2\gamma}r_0} \right)^2 + 1 + \frac{1}{8} \left(\frac{\gamma-1}{\gamma} \right)^2 - \left(\frac{2\gamma-1}{\gamma} \right) \ln 2 + \ln \left(\frac{1.123\beta}{\sqrt{2kT_e/m_0c^2}} \right)^2 \right], \quad (1)$$

where r_0 is the classical electron radius, m_0 , the electron mass, c , the speed of light, n_i , the background ion density, Z , the background average ion charge, T_e , the background electron temperature, k , the Boltzmann constant, γ , the relativistic energy divided by m_0c^2 and β , the relativistic velocity. This equation determines the amount of energy (dE) lost per distance the electron traveled (ds), but the distance traveled and distance penetrated are not the same because the electrons do not follow straight paths. Previous models have accounted for the discrepancy between the trajectory and the penetration distance by using the equation,

$$\frac{dE}{dx} = \langle \cos \theta \rangle^{-1} \frac{dE}{ds} \text{ where } dx \text{ is the penetration and } \langle \cos \theta \rangle \text{ is the average deviation angle from}$$

the straight line given by¹

$$\langle \cos \theta \rangle = \exp \left[- \int_{E_0}^E K(E') \left(\frac{dE'}{ds} \right)^{-1} dE' \right],$$

where

$$K = 4\pi n_i \left(\frac{r_0}{\gamma\beta^2} \right)^2 \left[Z^2 \ln \Lambda^{ei} + \frac{4(\gamma+1)^2}{(2^{\sqrt{(\gamma+1)/2}})^4} Z \ln \Lambda^{ei} \right]$$

and $\ln \Lambda^{ei}$ is the Coulomb logarithm.

Blooming and straggling have been added to the existing model using expressions from Ref. 1. Blooming is the deviation perpendicular to the initial direction of movement and is described by

$$\langle y^2 \rangle = \frac{2}{3} \int_{E_0}^E \langle P_1(\cos \theta) \rangle \left(\frac{dE'}{ds} \right)^{-1} \left(\int_{E_0}^{E'} \frac{1 + 2\langle P_2(\cos \theta) \rangle}{\langle P_1(\cos \theta) \rangle} \left(\frac{dE''}{ds} \right)^{-1} dE'' \right) dE'. \quad (2)$$

Straggling is the deviation parallel to the initial motion and is given by

$$\langle x^2 \rangle = \frac{2}{3} \int_{E_0}^E \langle P_1(\cos \theta) \rangle \left(\frac{dE'}{ds} \right)^{-1} \left(\int_{E_0}^{E'} \frac{1 - \langle P_2(\cos \theta) \rangle}{\langle P_1(\cos \theta) \rangle} \left(\frac{dE''}{ds} \right)^{-1} dE'' \right) dE', \quad (3)$$

where $\langle P_1(\cos \theta) \rangle$ and $\langle P_2(\cos \theta) \rangle$ are Legendre polynomials.

Procedure

A program was written to model the energy deposition of a beam of electrons into a target. While the program can model a target with non-uniform density and temperature, it was tested by modeling a uniform two-dimensional slab with a density of 300 g/cm³ and a temperature of 500 eV, for which an analytical solution is known¹. A

rectangular grid is used. The beam of electrons is modeled as many beamlets of infinitesimal width, which will be referred to as “beams” for simplicity. As each beam travels through the target, the energy deposited is calculated for each grid square it passes through. Thus, while the beams are treated as infinitesimal, the energy deposited is only accurate to the resolution of the grid. The spread of the beam is also calculated in both the blooming and straggling directions for each zone in the grid. That spread is summed over the trajectory and when it exceeds a certain level, which is a parameter of the model, the beam is split into multiple beams to represent the spread. The daughter beams have the same energy and direction, but represent different amounts of electrons. This method is illustrated in Figure 1.

The most efficient and accurate method was to split the electron beam into three daughter beams each time a split was required. Any more splitting produced too many beams, requiring too large a memory space, and having only two daughter beams required more splits, which again led to too many beams. The weights and distance between the beams were calculated so that the distribution of the beams stayed Gaussian with the correct standard deviation, obtained from Ref. 1. At each split the standard deviation of the set of beams was set so that it was halfway between the current deviation and what it would be next time the beams split. While this procedure leads to overestimation of the deviation right after the split, it averages out and does not consistently overestimate or underestimate the deviation for both straggling and blooming. The weights given to the beams were 57% of the electrons in the center daughter beam, and 21.5% for each of the off-center daughter beams, which were offset

by 1.325 standard deviations. This was found to keep the distribution relatively Gaussian without requiring too many splits.

These daughter beams were then transported into the target until their spread exceeded the maximum level, in which case they were again split. They were finally stopped when their energy was negligible compared to the temperature of the target, at which point their remaining energy was deposited in the current grid space.

Results

The results of this model are compared with those predicted by the analytic model of Li and Petrasso¹ in Fig. 2. Plotted are the differences between the two models in the average penetration distance (Fig. 2a) and in the final root-mean-square deviations in the x direction (straggling, Fig. 2b) and the y direction (blooming, Fig. 2c), for increasing source energy. The average distance is modeled very closely, with errors ranging from -2% to 1% over a range of energies. The problem was modeled with various sets of parameters (such as the distance moved between splits, the distance moved during the splits, and the width of the initial beam). The results for straggling and blooming, shown with yellow lines in Figs. 2b and 2c, are for the best set of parameters and show small deviations from the Li and Petrasso predictions (ranging from -8% to 11%). Depending on when the beams were split, the model could either overestimate or underestimate these values at the end of the simulation. An example is shown in the dark red lines for which the errors range from -23% to -8%.

The difference between the predictions of two different runs of the model for the energy deposited is shown in Fig. 3 for a 10- μm beam centered at 30 μm . Figure 3a

shows the difference when the blooming parameter is changed. Most of the differences are at the beam edges where the modeling of the blooming is more sensitive. The difference when the straggling parameter is changed is illustrated in Fig. 3b. In both cases the largest error is close to the source before the first split of the beamlets. In the bulk of the target the differences are about 10% or lower. These results show that the computational model provides a fairly accurate treatment of the propagation of the beam.

Future Work

The program could be improved upon in two different ways. Currently there is only one thread doing all the computations for the model, but the computations could be done in parallel. This could easily make the program many times faster. Another improvement to the program would be to reconsolidate the beams after a few splits. After about 6 splits there are 729 different beamlets; the calculation could be stopped at some stage and the beamlets in close spatial proximity could be combined. With recombining we could split more often than before, without having more beams at once. This is important because the number of beams is limited by the amount of available memory. Thus with recombining we could represent a smoother distribution with fewer beams, and not run out of memory. Using fewer beams would also speed up the model by requiring fewer computations.

Conclusions

An improved straight-line model, which includes straggling and blooming, has been developed to model the transport of relativistic electrons in the fast-ignition scheme.

In this model, after the electrons have accumulated a certain amount of straggling or blooming during their trajectory, they are split into three electrons. The direction and energy of each electron is chosen so as to provide the straggling and blooming predicted by analytic predictions such as those of Li and Petrosso. This model agrees with the analytic model within $\sim 10\%$ for the energy deposited, for a wide range of initial electron energies.

References.

1. C. K. Li and R. D. Petrosso, Phys. Rev. E **73**, 016402 (2006).
2. C. K. Li and R. D. Petrosso, Phys. Rev. E 70, 067401 (2004).

Acknowledgments

I would like to thank Dr. Jacques Delettrez, my advisor, for helping and assisting me on this project. I would also like to thank Dr. Stephen Craxton for directing the High School Research Program.

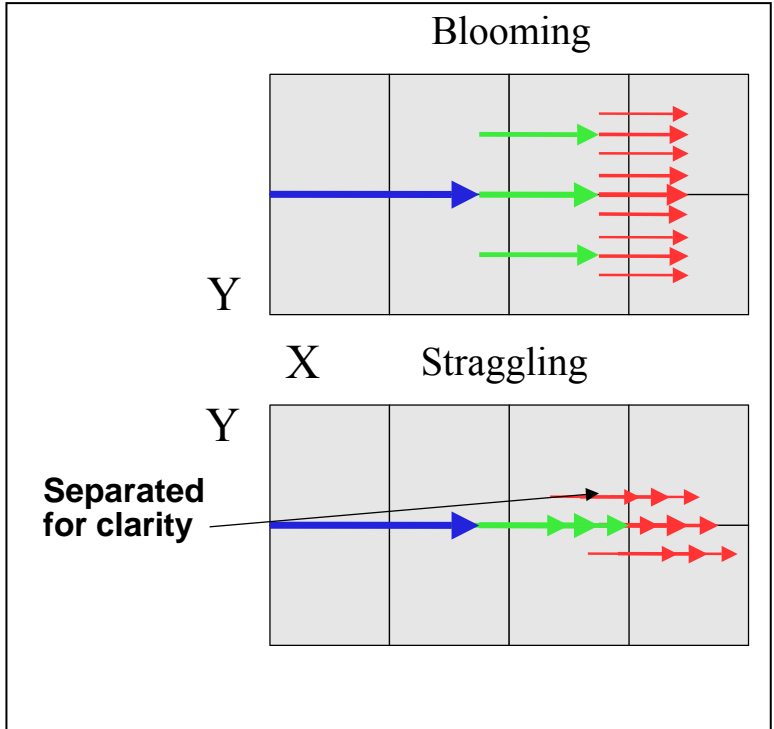


Figure 1. Diagram showing how an electron beamlet is split for blooming or straggling.

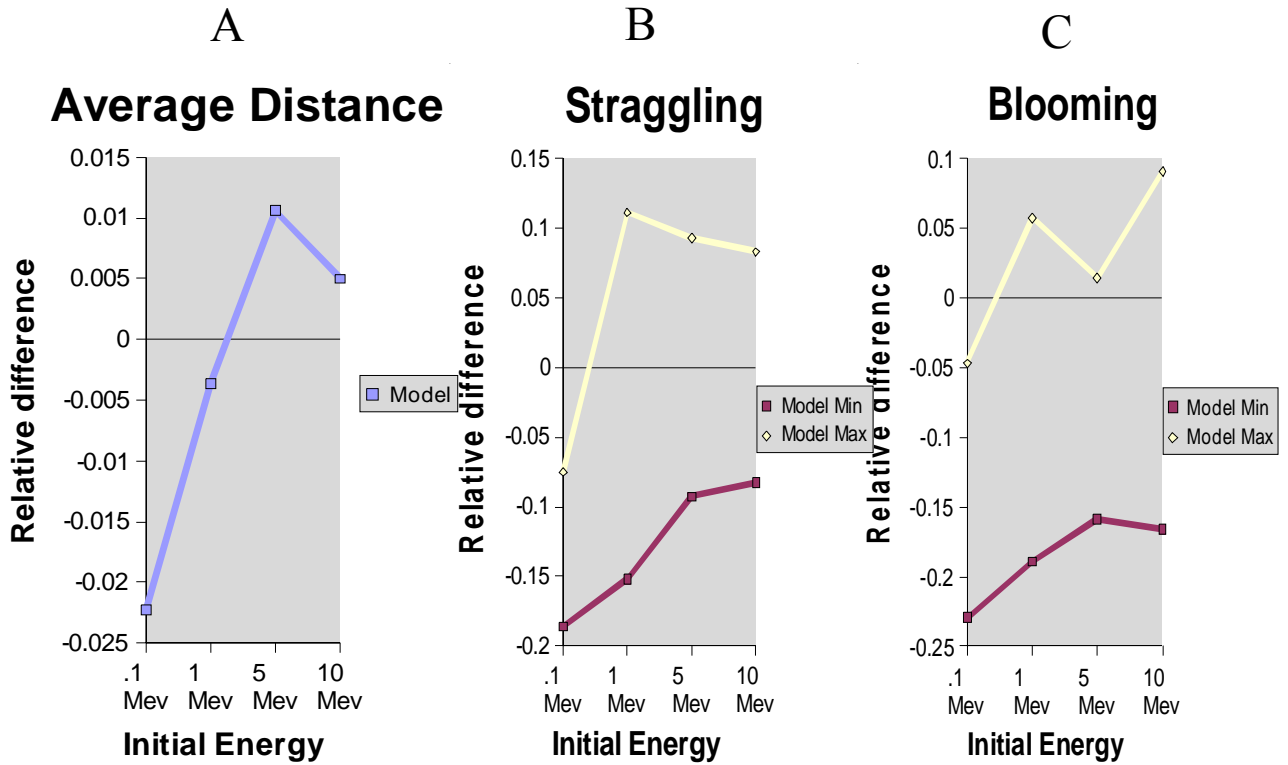


Figure 2. Differences between Li and Petrasso's predictions and those of the model for various source energies: a) average penetration; b) straggling; c) blooming. The yellow lines are for the best set of parameters; the dark red line is for another set.

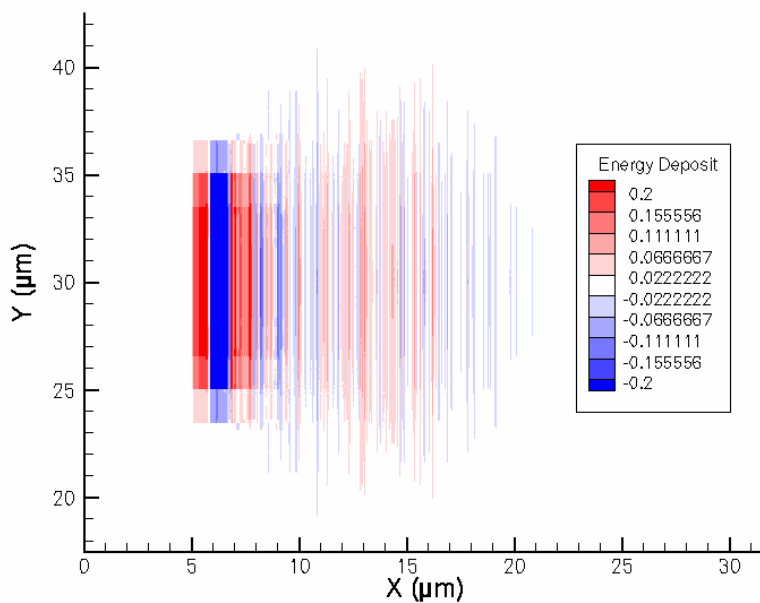
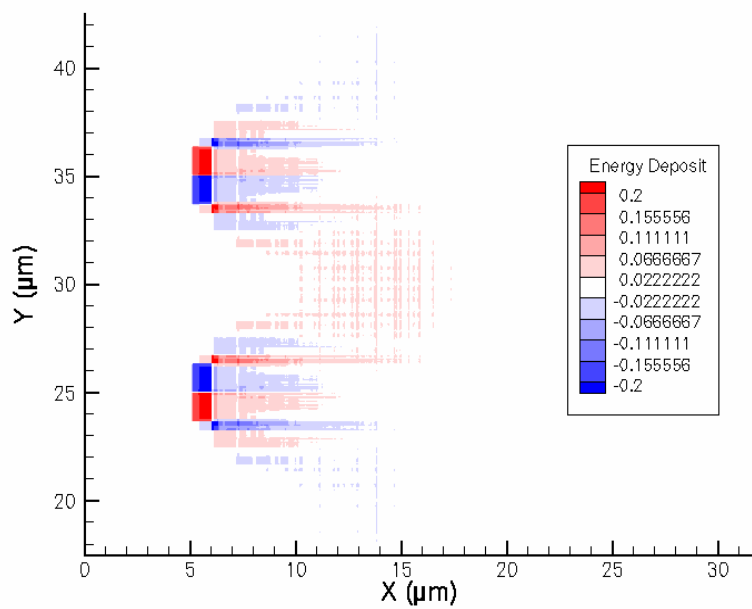


Figure 3. Fractional differences in energy deposition of the model for a 10- μm beam centered at 30 μm , between two different trials. In a) the two runs compared had different blooming parameters, and in b) they had different straggling parameters.

Fiber Optic Splice Optimization

Elizabeth Gregg

Fiber Optic Splice Optimization

Elizabeth Gregg

Naples Central

LLE Advisors: Shawn Mott, Jon Zuegel

Abstract

Optical fibers transmit data when light waves are propagated through them. Optical fibers have many applications at LLE, such as the fiber-optic switch module in the ROSS streak camera.¹ It is often necessary to splice two fibers together by a process called fiber-optic fusion splicing. There are two significant sources of optical power loss in a fiber: unoptimized splices and losses contributed by the connectorization of the fiber ends. In order to ensure that a splice is optimized it is necessary to have an apparatus that will measure just the loss of optical power caused by the splice, account for power fluctuations of the laser used to test the fiber, and do so accurately enough to measure low loss. A ratiometer was constructed that measures only the power loss induced from the splice and can measure losses as low as 0.5%. The ratiometer splits the beam into two paths. One path serves as the reference (reference fiber), and the other path contains the fiber being tested (fiber under test). Each fiber has a connector on both ends. Samples of power measurements are made before and after a fusion splice. This sampling process allows the energy loss contribution of the connectors to be eliminated. Using the ratiometer, an amended fusion-splicing program has been shown to reduce the loss in a splice from between 1.0 dB (20%) and 2.6 dB (45%) to 0.1 dB (~2%).

I. Introduction

Fiber splicing is a process by which the cut ends of two optical fibers can be attached together, resulting in one physical piece of fiber optic cable. Fusion splicing² involves aligning the fiber cores, heating the two ends, and pushing them together. There are some alternatives to fusion splicing. Mechanical splicing can be used; however, there is an alignment loss involved with the mechanical splice process. Fusion splicing, when optimized, is the best way of connecting two fibers because it minimizes optical power loss. The theoretical limit for an optimized fusion splice is a power loss of less than 0.01 dB (0.23%).

Some of the most common factors that contribute to a high-loss fusion splice are low arc power, excessive arc power, incorrect arc duration, uneven heating, and incorrect hot-push delay. Low arc power or incorrect arc duration will cause insufficient heating of the fiber. This causes a visible seam in the final splice. This seam acts as a reflective and refractive surface which in turn creates a high-loss splice. Excessive arc power will cause deformation in the core of the fibers. Deformation of the core changes the refractive index at the splice, which can also cause a high-loss splice. Uneven heating occurs when one fiber is heated and the other is not. This will cause the fiber to fail during the tension test, i.e. a brittle splice joint. Incorrect hot-push delay settings can cause the fibers to continue being heated when they are pushed together. This will cause the fiber to deform at the splice joint. The diameter of the fiber at the splice often changes under this condition, again leading to a high-loss splice.

The current fusion-splice program used at LLE for multimode fibers was designed for single-mode fibers of smaller core diameters. When applied to multimode fibers, where the core diameter is larger, the splice process caused a visible and often warped

seam. The appearance of this seam indicated low arc power, incorrect hot push settings, or possibly both. In order to optimize the fusion splicing process, the program must be modified, and a ratiometer is needed to test the results. This project involved the construction of a ratiometer to measure the optical power loss from fusion splices and its preliminary use to test an improved fusion-splice program.

II. Procedure

A Fitel³ S183PM fusion splicer was used for the fiber-optic fusion splicing. The splice process starts with precision alignment of the cores of the fibers. The S183PM does this by passing light orthogonally through the fiber core and recording the output with a CCD camera installed on the fusion splice machine. Light that passes through the center of the core will be un-refracted and the resultant output light intensity will have a Gaussian type distribution with the peak of the distribution curve corresponding to the center of the fiber core. The core location is then calculated and aligned appropriately. The aligned fiber ends are then heated by an electrode arc shot across the ends of the fibers. The hot push brings the fibers together while the fiber ends are in the molten state. Improperly heated fibers will not bond well during the hot push. An optimized splice will have no visible seam through the core; i.e., the splice joint will look homogeneous.

The ratiometer illustrated in the block diagram of Fig. 1 was developed in order to test the loss from the splice and not from the connectors or any other source of potential error. The apparatus starts with a green laser (532 nm) as the light source, followed by a lens used as a fiber launcher to fill the fiber with higher order modes. Filling the fiber with higher order modes replicates how the fiber would be used in a

typical application at LLE. The splitter is used to split the beam into two paths. Both sides are followed by a photodiode, so that the light is turned into measurable voltage. The ratiometer measures the ratio between a reference fiber, which is not moved or spliced for the duration of the experiment, and the fiber being tested. The other side of the ratiometer holds the test fiber. The light transmitted across the fiber is sampled twenty times. The fiber is then cut and spliced and sampled again another twenty times. By using sample statistics, the mean loss due to connector misalignment can be calculated. Subtracting this loss from the overall power loss of the spliced fiber will yield the loss component due to the splice.

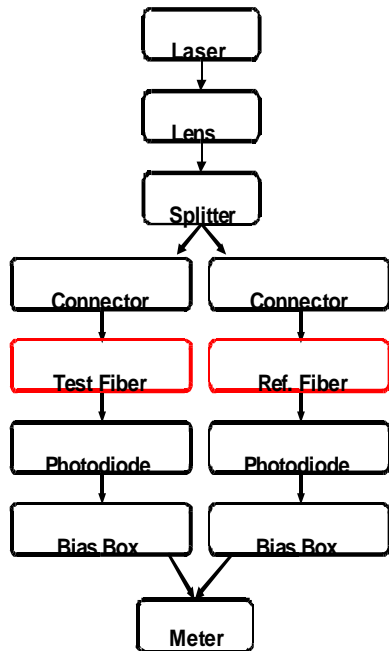


Fig. 1. Block diagram of the ratiometer used to test fiber splices.

III. Results

Results from twenty samples of an un-spliced fiber using FC connectors are shown in Fig. 2. An oscilloscope and meter were both used for simultaneous data collection. Statistics of the 20 samples from the scope and meter should yield similar results, i.e. they should track each other. This eliminates the possibility of one measuring

device being “bad”. Data from the reference fiber was also collected and used for the final data comparison. The reference data were recorded every time that sample data were taken. Statistics were also applied to the reference samples in order to calculate mean laser power. The distribution of the reference samples was very narrow and 20 samples resulted in a mean calculation that was equal to the true laser power to a high accuracy. The very small variations in the signal obtained using the meter and scope show that the transmission through the fiber can be measured to an accuracy of better than 0.5%. This allows the loss due to the splice to be measured to an accuracy of 0.5%.

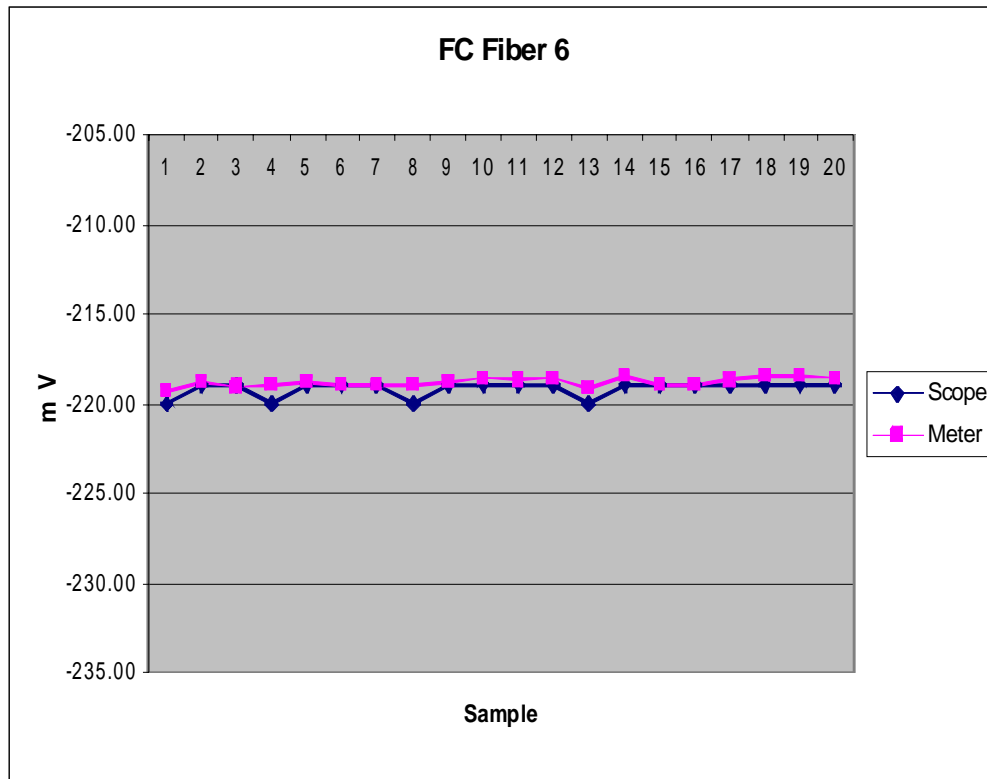


Fig. 2. Signal representing the light transmitted through an optical fiber measured on 20 consecutive samples. The fiber was disconnected and reconnected between samples. The fiber used FC connectors. The consistency of the meter reading allows the fiber transmission to be measured with a 0.5% accuracy.

In contrast, results for an un-spliced fiber using SMA connectors are shown in Fig. 3. Here the large variations between samples (up to 10%) demonstrate that the transmission through fibers with these connectors cannot be measured with the desired accuracy.

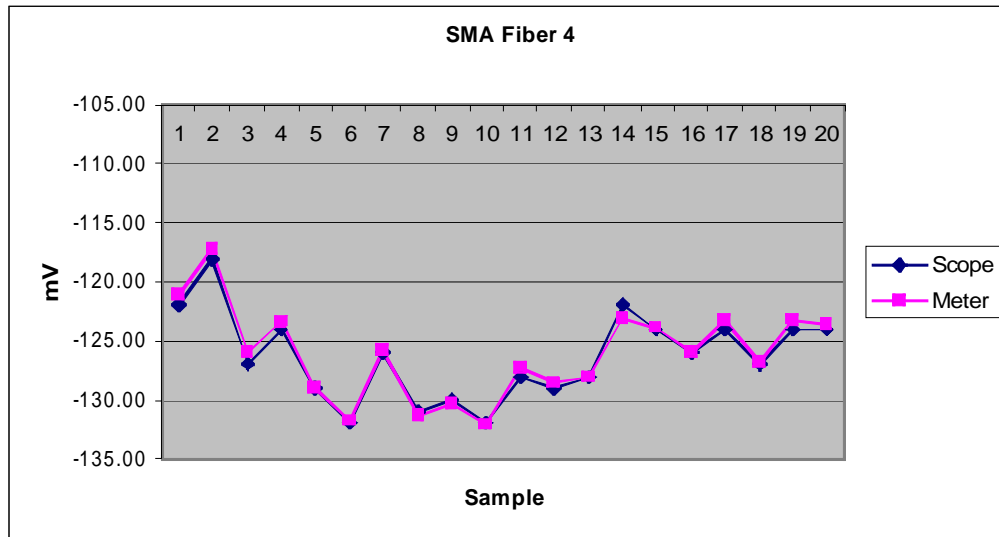


Fig. 3. As Fig. 2, but for a fiber using SMA connectors for accurate measurements of fiber transmission.

The FC connectors are keyed, meaning that they align to approximately the same position every time they are connected, unlike the SMA connectors. The FC connectors were therefore used in subsequent experiments to optimize the fusion splicer program.

The program was modified by increasing the end power setting of the arc from 100 to 175. The arc duration was also increased from 3000 ms to 3200 ms. Overall, the average normalized arc power was raised from 300 to 440. Results for a test fiber are shown in Fig. 4. The navy blue and yellow plots are for the reference fiber, pre and post splice respectively. The pink and light blue plots are for the test fiber, pre and post splice respectively. The overall loss of this optimized splice was measured to be 0.117 dB. Since the previous fusion splicer program resulted in a loss of 20% – 45%, the

modifications to the program resulted in a decrease in loss from the splice by about a factor of 10, a large improvement.

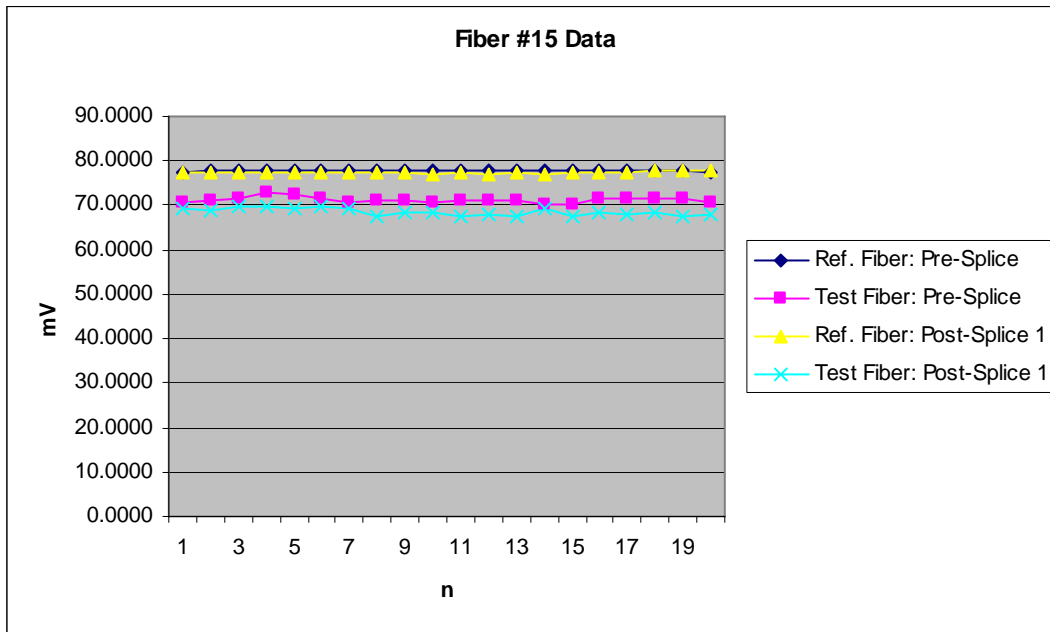


Fig. 4. – Data plots of reference and test fiber pre and post splice. N = 20 sample points. The overall optimized splice loss is calculated as 0.117 dB.

IV. Conclusions

A ratiometer was constructed to accurately measure the transmission loss in a fiber due to a fusion splice. Initial tests found that it was impossible to obtain consistent results from fibers using SMA connectors, so FC connectors were used instead. It was found that the transmission through a fiber with FC connectors could be measured to an accuracy of 0.5%.

The ratiometer was then used to evaluate changes to the fusion splice program by measuring the transmission before and after the splice. The modified program showed significant improvement, reducing the loss due to the splice by a factor of 10. The

process is still not fully optimized and more improvements need to be made for the splices to have the minimum loss possible.

IV. References

1. P.A. Jaanimagi, R.Boni, D. Butler, S. Ghosh, W.R. Donaldson, and R.L. Keck, "The Streak Camera Development Program at LLE," in *26th International Congress on High-Speed Photography and Photonics*, edited by D.L. Paisley, S. Kleinfelder, D.R. Snyder, and B.J. Thompson (SPIE, Bellingham, WA, 2005), Vol. 5580, p. 408.
2. A.D. Yablon, "Optical Fiber Fusion Splicing", Springer 2005
3. Fitel Inc., 200 Westpark Drive, Suite 190 Peachtree City, GA, 30269 USA

Implementing a Knowledge Database for Scientific Control Systems

Daniel Gresh

Implementing a Knowledge Database for Scientific Control Systems

Daniel Gresh

Wheatland-Chili High School
LLE Advisor: Richard Kidder
Summer 2006

Abstract

A knowledge database for scientific control systems is a powerful tool that allows users to obtain comprehensive information from a single source. A Semantic Web implementation of a knowledge database is intelligent enough to recognize what the user wants to know and present the correct information back to the user. A solid foundation for such a Semantic Web database has been built using the Java programming language, as well as the XML, RDF, OWL, and SPARQL languages. Using this database, a user may already obtain specific, detailed information regarding any aspect of the OMEGA EP Control Systems in an efficient manner from a single source, as opposed to searching through numerous technical and design documents. This foundation of the Semantic Web implementation covers Oracle/SQL, as well as the XML/RDF/OWL/SPARQL aspect.

The potential for such a database implementation is substantial. Upon completion, the database will automatically gather information concerning scientific control systems, organize it in an intelligent manner, and present intelligent results back to a user when he or she asks the database a question. Further research into the concept of this Semantic Web implementation will lead to automation of data-gathering; a basic form of artificial intelligence; a single repository for important subject data; and the ability for users to input their own information to expand the database.

Introduction

The Semantic Web

The Semantic Web is a vision for the future of the Web and for the future of information exchange. Rather than simply having information presented to humans, information will be processed in a way that makes it easier and more efficient to find.

In the Semantic Web, metadata, or "data about data", is very useful, as it allows machines to process information rather than present information. By processing information, a machine

is able to gather enough useful information to solve problems, which greatly assists any users of such a system.

Due to this ideal, a Semantic Web implementation of a knowledge database will allow a user to find exactly what he or she is looking for with minimal effort and high efficiency, as the information in the database will be processed so the database can present the user with the correct information.

Background

LLE has gathered an enormous amount of data and documentation since the start of operations. This data is currently spread over a number of different repositories. Currently there are several hundred active control subsystems, all of which gather and record subject data, which is documented in many ways and stored in one of the data repositories.

The current data repositories include the Product Data Management (PDM) system, word documents, spreadsheets, databases, images, schematics, and events in onboard control memory.

The current PDM system consists of a few general subtopics for the included documents, and then displays links to all the documents, which a user can click on to view a certain document. The PDM system also includes a simple Google search box in which a user can search for certain keywords, and a Google search will be performed on the numerous documents, returning the most relevant documents to the user.

The Oracle database is simply a store for all the data and image information related to OMEGA and OMEGA EP shot operations.

Spreadsheets and other documents are often isolated on personal office workstations.

Purpose of the research project

Easily retrieving data from one or any current LLE documentation requires expert knowledge of LLE infrastructure and of the subsystem. For a user to retrieve data using the current system, he or she must follow a number of steps.

For example: the user must determine which data source to browse for the information. The user must already know if the data he or she is looking for is located in the PDM system, or if the data is located in the Oracle database. If a user does not know which one of these sources the data is located in, he or she will have to browse through both databases, which is very tedious.

Second, the user must know where to find the data in a certain data source. If using the Oracle database, the user will

need to know which table he or she wants to pull information from. If using the PDM system, the user will need to know which document the information is located in. Otherwise, more tedious searching is required.

Third, the user must parse through the document or table he or she selected, and retrieve the correct data. While this is not a big problem with the Oracle database, it can be very problematic when using the PDM system. Not only does the user need to wade through numerous technical and design documents, he or she must parse the documents manually and extract the correct information. This may lead to even more tedious searching, as a document may not have the specific information a user is looking for, and he or she will have to parse through another document.

Purpose of a knowledge database

A Semantic Web implementation of a knowledge database helps solve this problem by organizing data into a hierarchical structure in which data is organized conceptually and is related to other data through conceptual means. This is also known as an ontology.

After organizing the data in this fashion, the data is stored in a single repository, from where it can be extracted easily. Important data from all sources -- e-logs, technical journals, requirements documents, etc. -- is stored in one location in an organized manner, rather than having the data spread over multiple data sources in which the data is loosely organized.

Furthermore, the data is easily extractable. Rather than manually parsing through numerous documents or tables in a database, a user is able to easily navigate to whatever concept he or she is interested in and view all the related data pertaining to that concept. Also, the Semantic Web implementation enables the user to search the knowledge database using freeform text, or natural language.

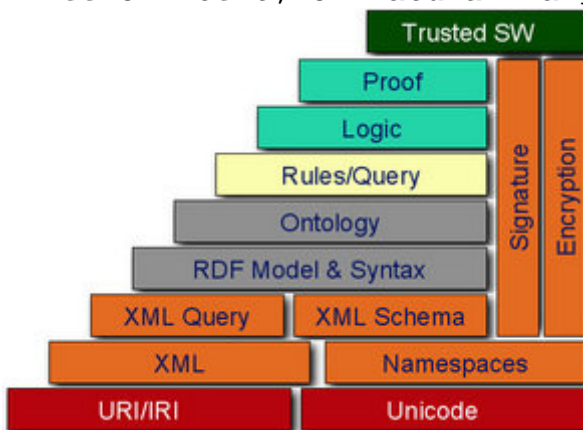


Figure1: The World Wide Web Consortium Semantic Web Framework (<http://www.w3.org/2001/sw/>)

As seen in Figure 1, the Semantic Web has many different building blocks. The basis of the Semantic Web is formed with URI/IRI, or resources. The resources are then structured in a certain way using XML and XML namespaces so the resources can be processed by machines. Then, XML Query and XML schema allow the data to be further refined and queried by providing a slightly more rigid structure; this rigid structure assists XML Query to find information. Finally, using RDF and OWL, which refine the data into an ontological structure, logic and proof are established, which allows machines to draw inferences from the resources, leading to a trusted, stable Semantic Web.

The knowledge database also lets users input their own information. The knowledge database receives manual input, and recognizes when an update to a document or e-log has been made, and reacts accordingly. For example, if a technician makes an entry into an e-log, or an engineer creates a new design document, the knowledge database recognizes this event, obtains the important information from the entry or document, and stores it in the database accordingly.

A Semantic Web implementation is a universal system for processing information. One of the many advantages a knowledge database of this structure has is the ability to connect to other knowledge databases and incorporate that knowledge into useful information. A database of this structure is able to not only contain important subject information from local sources, such as LLE control systems, but also gather and use data and information from external, related sources, further improving efficiency.

A knowledge database of this fashion has unlimited potential for expansion and upgrades. It is a universal repository for important information; this information can be easily extracted due to the data being stored in a machine-readable format.

Furthermore, the tools required to build a knowledge database of this fashion are very easy to acquire and easy to use. Also, the majority of the tools used for this work are open-source tools (free for anyone to use and develop). One of the tools used for this work was not open-source; however it is possible to create a knowledge database with an open-source tool that provides the same features.

The goal of this project was to build a strong, working foundation for a Semantic Web implementation of a knowledge database. This goal was accomplished; an RDF/OWL database was created using Java and the Jena development package for Java, and it is queried using SPARQL through Java and Jena.

Research and Analysis

Researching the implementation of a knowledge database that would store the data in a single repository required choosing a small subset of controls. A few diagnostic and control subsystems were chosen for the test case. Much of the implementation used the Calorimeter system.

Preliminary research and analysis

One of the goals of this project was to analyze methods for creating a knowledge database, and decide which method would work best for the project. Then, the appropriate techniques and tools would be used to create a strong foundation for the knowledge database. Furthermore, the research and analysis was to be done independently. Any tools and/or methods could be chosen that would create a knowledge database in the most efficient manner.

Initially, fourteen different languages were investigated. Eleven of them are listed in Table 1, together with their purpose, and the reason why they were or were not selected for use.

Many different tools and software packages were analyzed that might be useful, including Altova SemanticWorks, Protégé OWL, Jena, Lixto, Inxight, Evermap, Adobe Online Tools, KAON, JTP, Twinkle, Metadata Miner, Pellet, Omnipage, PDF Extraction, PDF to all, PDF Extractor API, pOWL, OWL API, PDF Metadata, VortexXML, and XML Army Knife. Tools were looked at for writing RDF/OWL, for performing SPARQL queries, for writing PHP, and for extracting data from documents.

Developing a data mining tool was a large concern. In order for quality, reliable data to be extracted from the numerous documents and sources that exist at LLE, some type of extraction tool would have to be developed. To determine how to create such a tool, the field of data mining and extraction was investigated. Studies of data mining and extraction methods led to one conclusion: the tool would have to be custom developed specifically for LLE; a pre-existing data mining tool would not work. This tool will be the subject of future work.

The World Wide Web Consortium (W3C) Web site proved to be a very valuable source of information,¹ in particular on the languages of RDF, OWL, XML, and SPARQL. Work related to this project is found in Refs. 9-12.

Language	Used?	Purpose	Reason
XML	Yes	Structure basic elements and resources	XML is the basis for RDF/OWL
XPATH	No	Navigate through XML documents	Navigating through XML with XPATH is not needed
XSL/XSLT	No	Transform XML into XHTML for readability	Presenting readable XML is not needed
XHTML	No	Design web pages with a stricter syntax than HTML	Database foundation was built in a Java GUI; no web page was needed
PHP	No	Server-side scripting language	Java has more resources for writing RDF/OWL
RDQL	No	Querying RDF data	Replaced by SPARQL
DAML/OIL	No	Designing ontology structures	Replaced by OWL
XQUERY	No	Querying XML documents	Not needed; SPARQL was used to query RDF/OWL
RDF	Yes	Describing resources	Provides basic structure for ontology
OWL	Yes	Relating resources to each other	Defines relationships between resources in ontology
SPARQL	Yes	Querying RDF/OWL	Queries RDF/OWL ontologies and extracts data

Table 1: Analysis of languages considered in this work

RDF/OWL and the Semantic Web

Using the languages of eXtensible Markup Language (XML), Resource Definition Framework (RDF), and Web Ontology Language (OWL), information and data in the Semantic Web will be organized in a structured manner in formats called ontologies. Ontologies have the ability to organize data and present it in a manner so that machines can draw conclusions and inferences from the data.

The Semantic Web is not pure artificial intelligence. Rather, as previously stated, it will use data that can be processed by machines to solve questions and perform tasks.

The three "main" languages that the Semantic Web concepts are based upon are XML, RDF, and OWL. These languages work together to describe resources and relate them to each other so that machines can process the information. These languages do not exist to provide information to humans, but rather to provide information to machines, so the machines can then determine what information is useful to provide to humans.

By structuring the resources using RDF/OWL and creating an ontology, numerous resources can be related to each other so they can easily be processed by a machine. An example of such a use is shown in Figure 2, which represents a small subset of OMEGA EP control systems. "IR Cal System" forms the base for the subtopics under it. These subtopics branch off into many different subtopics. However, due to the reasoning capabilities of RDF/OWL ontologies, although a subtopic such as "TSF Cal 1" may be a direct subtopic of "TSF Cals", a machine can reason that "TSF Cal 1" is also a subtopic of "IR Cal System".

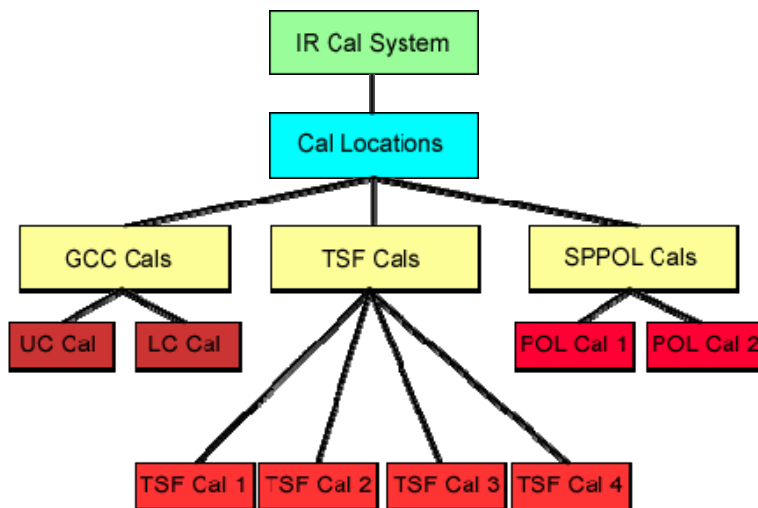


Figure 2: Structure of resources.³ Cal: Calorimeter; GCC: Grating Compression Chamber; UC: Upper Compressor; LC: Lower Compressor; TSF: Transport Spatial Filter; SPPOL: Short-Pulse Polarizer; POL: Polarizer

RDF is structured as a series of graphs called "triple graphs". These triple graphs, or triples, are what make it possible for machines to process RDF. A triple is a basic description that is read in the form: subject, predicate, object. For example, one could use RDF to specify the title and author of a certain book, by creating a triple with subject Example Book; predicate author; and object John Smith. This would then be read: the **author** of Example Book is **John Smith**.

Triples are instrumental in creating a database structure for LLE data. By using the triple format, data is stored in RDF where it can easily be extracted with SPARQL. For example, by creating a triple with subject "SPPOL Calorimeter Location"; predicate "information"; and object "The SPPOL Calorimeter is located between beamlines 1 and 2", one could read: the **information of SPPOL Calorimeter Location is, "The SPPOL Calorimeter is located between beamlines 1 and 2"**.

Planning and Design

Preliminary design

Java was chosen as the language to program the database. The database had to be flexible, easily modifiable, and transportable across the Web to a variety of operating systems for easy access.

Java is an object-oriented programming language. In other words, an application is a series of individuals, or objects, rather than simple commands to the computer.³ Using Java it is relatively simple to keep a database structure organized and functional.

Java provides a simple, object-oriented structure, whereas PHP does not. PHP is a server-side scripting language. There are tools available that allow RDF/OWL ontologies to be built using PHP, but Java's object-oriented nature allows the RDF/OWL to be built in a more efficient, modifiable manner.

Furthermore, there are more resources available to assist in building RDF/OWL ontologies with Java than there are with PHP. RAP, the most common PHP development kit for writing RDF/OWL, has far less support and usage than Jena, the most common Java development kit for writing RDF/OWL. Because of this, using Java allows the programmer to learn the structure and functions faster, resulting in greater efficiency.

Tools

To develop an RDF/OWL database in Java, the Jena development package was used⁹. This is an external library for Java that allows for the programming and development of RDF/OWL databases. Jena also has support for the SPARQL querying language in its Application Programming Interface (API), which greatly assists when performing SPARQL queries against the RDF/OWL database.

Furthermore, some free tools were downloaded that would allow for the easier development of a Java application to create an RDF/OWL ontology. These include the Eclipse and Netbeans

Integrated Development Environment (IDE), as well as the Pellet OWL DL syntax checker/reasoner. A reasoner for OWL is a tool that determines how many inferences can be made from the ontology.

Current Design

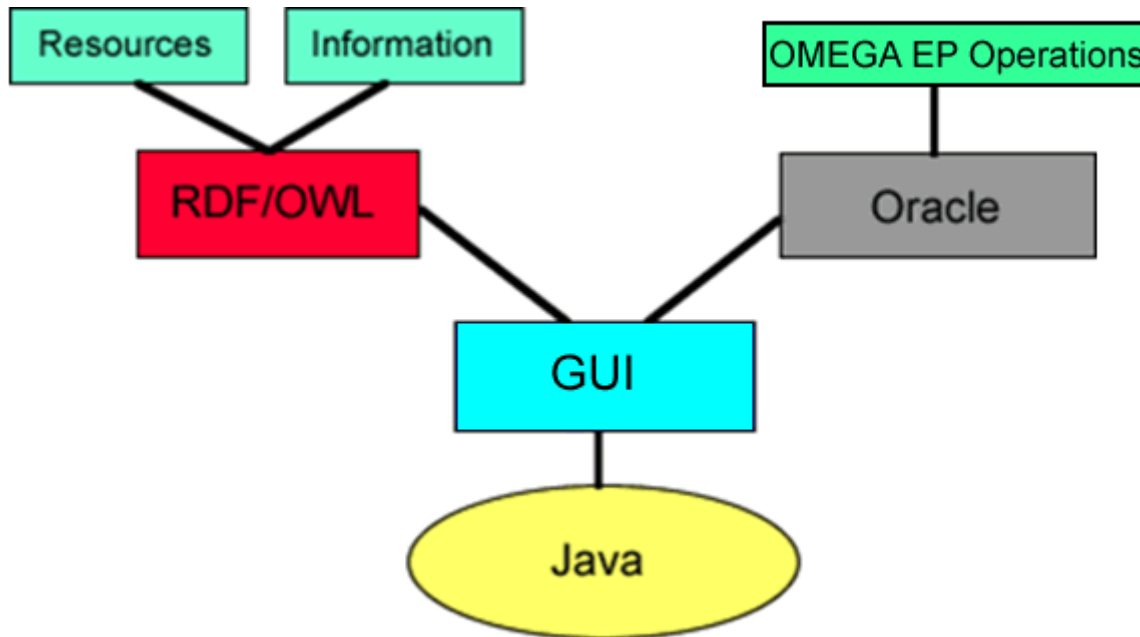


Figure 3: Database Design³

Figure 3 depicts the structure of the Semantic Web implementation. Java acts as the backbone for the knowledge database. From Java, a Graphical User Interface (GUI) is displayed, which contains access to the RDF/OWL and Oracle portions of the database. From there, resources and information pertaining to control systems, and resources and information related to OMEGA EP operations, are respectively displayed.

To create a solid structure, numerous Java classes were created. Java classes allow for simple portability and ease of coding. Having the entire application divided into a number of classes will also assist future programmers in learning the code and structure.

There are a few basic classes. One class creates the RDF/OWL ontology. Another class performs queries against the database, and another creates a GUI to display the information. In the future, many classes will be added, and the current classes will be refined into easier-to-use classes.

Current Status

Currently, a strong foundation for the database has been created, and a working, functional prototype of the database was successfully demonstrated. The database is currently a simple Java Archive (JAR) file for ease of use, and will be uploaded to the local intranet.

Figure 4 shows the structure of the graphical user interface for the Semantic Web Knowledge Database. A simple tree diagram is contained on the left side that allows a user to select the topic he or she desires. When the user clicks on a certain topic in the tree diagram, the information associated with that topic is displayed, as shown in Figure 4.

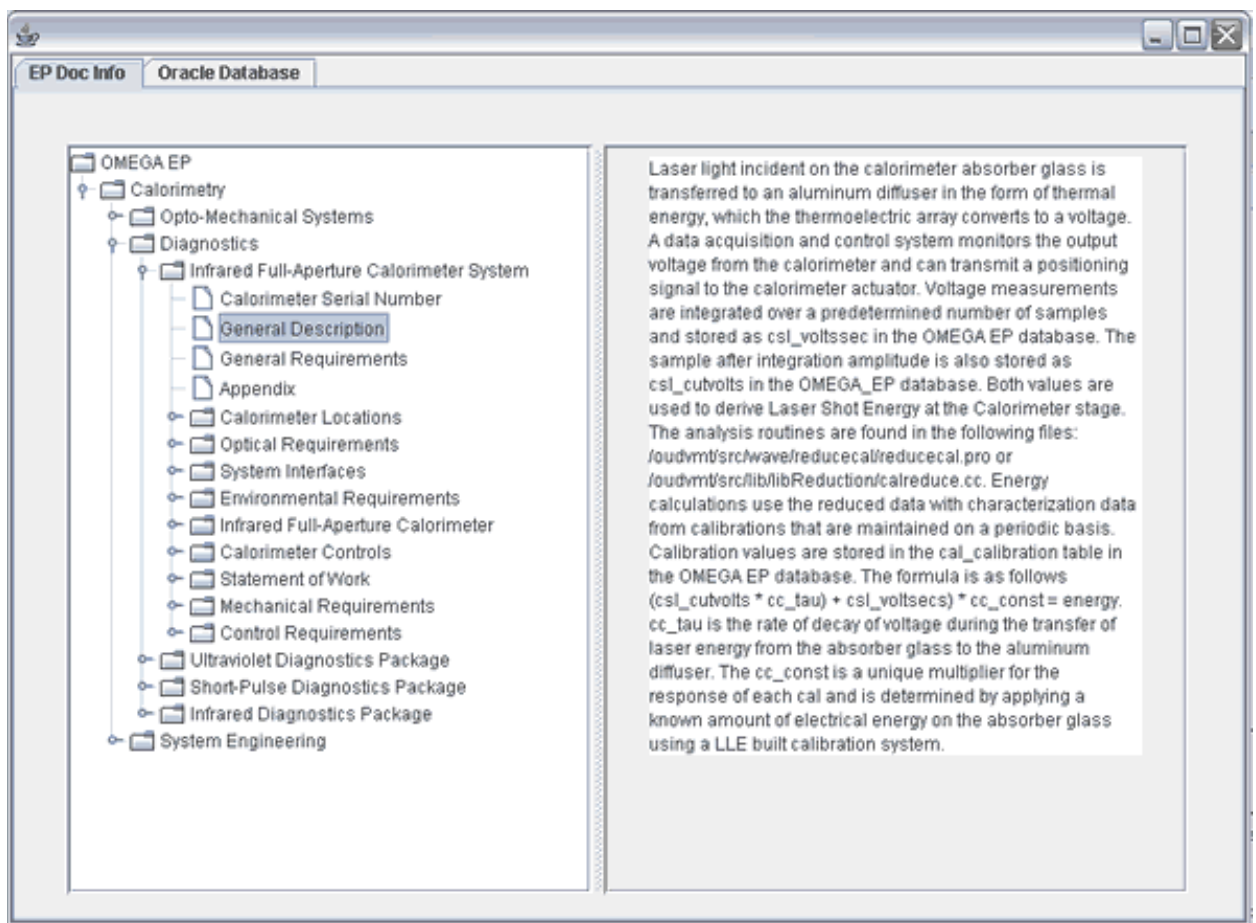


Figure 4: The Semantic Web knowledge database GUI

The Java code for the database has been created in such a way that it will be very easy to modify and expand upon. The code for the database has unlimited potential to evolve and expand, allowing multitudes of new features (see next section).

An ontology in OWL Full, for maximum ease of use, has been created that stores data about a small section of control systems: calorimetry. A GUI has been created that allows for easy searching of that database. Functionality has been added to the database that allows it to search the Oracle database about OMEGA EP operations.

The user currently browses through the information in the ontology by using a tree diagram. When the user selects a certain node on the tree, a SPARQL query is executed against the RDF/OWL ontology, which returns the necessary information and presents it to the user. The tree diagram allows the user to easily specify the information he or she is looking for, and view it in a simple, efficient manner.

Future Features

As the project moves forward, additional features will be designed and implemented. Further research into the field of artificial intelligence and the Semantic Web will lead to more advanced features that can be implemented at LLE. Much of this research may take place at MIT's Computer Science and Artificial Intelligence Laboratory, where extensive research is already being done.

In the coming year, a user will be able to enter freeform text questions into the database and receive the correct answer, rather than using a tree diagram. The database will gather all information automatically and will eliminate redundant information. Also, it will organize the gathered information in an ontology, where it can be structured in an intelligent manner. There will also be the ability for users to enter their own information into the database, expanding it with important information. The database will be able to recognize what information is important or not, and take action accordingly.

The database will be a single repository for important information. Rather than having numerous sources for data, all data will be stored in one central location where it can be easily and efficiently extracted. The database will have the ability to be expanded and upgraded to fit any reasonable need, and ultimately improve our knowledge of control systems and other important areas.

Acknowledgements

I'm excited to continue this fascinating project during my senior year at Wheatland-Chili High School. I thank LLE - in particular, Richard Kidder, Robert McCrory, and Stephen Craxton - for giving me this wonderful opportunity. I would also like to

thank Ivan Herman, the director of W3C's Semantic Web Activity, and Jim Hendler, a professor at the University of Maryland, who is a chair on W3C's Semantic Web Activity, for their assistance during the course of the summer.

References

1. <http://www.w3.org/>
2. http://en.wikipedia.org/wiki/Object-oriented_programming
3. PowerPoint presentation on the summer research project:
<http://www.seas.rochester.edu/~gresh/dangresh/DGreshRev3.ppt>
4. <http://www.w3.org/2001/sw/>
5. NASA ScienceDesk white paper:
<http://ti.arc.nasa.gov/publications/pdf/ISWC-04%20SemanticOrganizer%20Paper%20pub.pdf>
6. Additional notes and design ideas from notes taken over the summer: http://www.seas.rochester.edu/~gresh/dangresh/LLE_Semantic_Web.pdf
7. MIT's CSAIL Decentralized Information Group Semantic Web Projects: <http://dig.csail.mit.edu/>
8. Jena: <http://jena.sourceforge.net/>
9. Personal Publication Reader: <http://www.personal-reader.de/semwebchallenge/sw-challenge.html>
10. NASA ScienceDesk: <http://sciencedesk.arc.nasa.gov/>
11. Platypus Wiki: <http://platypuswiki.sourceforge.net/>
12. Swoogle: <http://challenge.semanticweb.org/>

Realtime Focal Spot Characterization

Matt Heavner

Realtime Focal Spot Characterization

M. Heavner

Advised by Dr. Christian Stoeckl

Laboratory for Laser Energetics

University of Rochester

250 East River Road

Rochester, NY 14623

March 13, 2007

Abstract

Short-pulse laser-plasma interaction experiments are carried out at the University of Rochester's Laboratory for Laser Energetics (LLE). In these experiments a short (< 1 ps) laser pulse is focused to a small (< 4 μm) spot on a solid target, rapidly creating a plasma. During alignment, the focal spot has to be located and characterized. A CCD camera provides high-resolution image data of the focal spot in analog format that is converted into a digital signal with a framegrabber, allowing it to be used by software. A program has been developed using the C and Java programming languages that accesses the framegrabber, acquires images, and interprets acquired data. It is able to locate the focal spot from the CCD data, graph the data, zoom into and autoscale the image, and infer the size of the focal spot.

1 Introduction

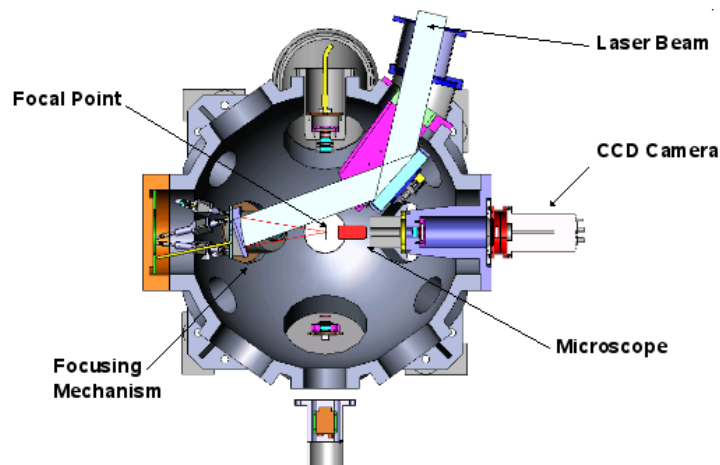


Figure 1.1: LLE's MTW Experimental Setup

In the University of Rochester's Laboratory for Laser Energetics (LLE), short pulse laser-plasma interaction experiments are carried out. In LLE's experimental setup (shown in **Figure 1.1**), a laser beam is sent into a chamber, reflected off a flat mirror and an off-axis parabolic mirror, and focused by a focusing mechanism on a small target. In the alignment of this setup, a requirement to locate and characterize laser focus points arises. Charge-coupled device (CCD) cameras, connected to microscopes, are used to provide real time, high-resolution image data of these points.

CCD cameras are used extensively within LLE experimental setups. CCDs provide high-resolution images and are up to 70% more photosensitive to incident light than photographic film. A CCD is composed of an array of photosensitive capacitors. During exposure, charge is transferred to non-photosensitive cells that are located in between active rows. The charge in these storage cells is shifted along the row one row at a time to form a video signal. This occurs while the active cells are being exposed to produce the next frame.

To access and interpret image data, a framegrabber must be installed in the client computer that is accessing the CCD camera. A framegrabber converts the analog video signal from the CCD to a digital signal, as shown in **Figure 1.2**, that is usable by a computer. The framegrabber used in the development of this program was a DT3155, created by Data Translation, Inc.¹ The DT3155

provides four multiplexed monochrome inputs, 8-bit digitization, programmable black and white levels, real-time image thresholding and image scaling and clipping.¹



Figure 1.2: A CCD camera, DT3155 framegrabber and DTControl in use^{2,3,4}

A program has been developed to actively locate and characterize a laser focal point using data acquired from a framegrabber that is attached to a CCD camera. It uses both the Java and C programming languages and the open-source Linux DT3155 driver⁵, modified to fit LLE needs. This program (DTControl) has been designed to be as self-intuitive as possible, allowing a scientist to start using it without previous knowledge of its inner workings and to still acquire necessary and useful information. Tools and features have also been added to allow the program to adapt to different experimental environments. The program has been designed to accommodate future upgrades.

2 Programming Technologies

Many operating systems are in use within LLE. Because of this, program code must be portable so that it may be used on different platforms. This program was designed and tested on a Linux machine. The GNU/Linux operating system⁶ has proven to be very successful and stable, and is used frequently within LLE because it allows code to be portable. The Java and C programming languages, along with the Java Native Interface, were utilized in the creation of this program. Java, which began as a Sun Microsystems project termed Oak that sought to provide an alternative to C/C++⁷, allows for the creation of code that can be used on many platforms. This is possible through the use of the Java Virtual Machine (JVM), which itself is platform-specific. Java code is created

and, when run, is interpreted by the JVM and executed on the desired platform. Methods to access hardware were intentionally left out of the Java programming language in order to provide portability across varying hardware. The C programming language, developed in 1972 in the Bell Telephone Laboratories by Dennis Ritchie for use on the Unix operating system⁸, is known as a lower-level programming language that provides direct access to computer memory and other intricacies. Code developed in C is platform-specific and is often more efficient than code written in other languages, such as Java, as it doesn't have overhead code, such as Java's JVM. It is useful when interfacing hardware or operating systems directly.

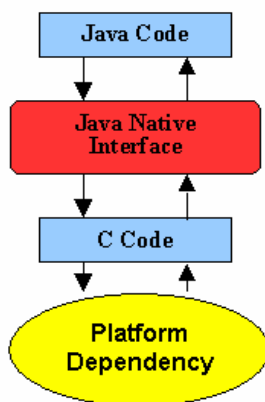


Figure 2.1: The Java Native Interface allows native languages to communicate with Java

In the event that a Java program must access platform-specific features, or code written in a lower-level language, the Java Native Interface must be used (see **Figure 2.1**). The Java Native Interface provides a way for Java code to utilize software libraries written in a native language, e.g., C or C++⁹. In the case of DTControl, it was used to provide the Java code with access to the DT3155 framegrabber.

3 Program Requirements

Requirements of the program needed by the user (LLE scientists) include the ability to locate and track a laser focal point, to measure and characterize such a point via graphing and interpretation

of data, to save and load images, and to adjust to various environments. The user must also be given the option of changing the accuracy of these features. Internally, the program must be robust and accurate, as many other process and tools are used concurrently on LLE computers.

4 Algorithm Design and Analysis

Algorithms were developed to allow for zooming, the location of a laser focal point, the measurement of a laser focal point, and auto-scaling of the image intensities to allow for better contrast.

4.1 Digital Zoom Algorithm

Upon a request from a user to zoom into a certain portion of an image, a boxed area of data surrounding the clicked point is partitioned. Pixels found within this area are expanded so that the selected portion of the image fills the entire viewing area. This may only be done a certain maximum amount of times, as zooming into a portion of the image too far will make it appear overly pixelated.

4.2 Focus-location Algorithm

Other algorithms and program aspects are dependent upon an accurate focal-spot center being found. This algorithm must be efficient because it is run very frequently (defaulted at every five frames). The process of finding the center involves two stages. First, an approximate center is located. This result is used in the second step that narrows the given information into an accurate result.

The first stage, location of the approximate center, works as follows: First, every n^{th} line (an undersampling rate of n) is checked for pixels of intensities greater than a certain value. These values are stored in an ArrayList, a dynamic storage structure. Second, the surrounding intensity (defined as the average over a six by six pixel area) of each previously found pixel is calculated. The

pixel with the greatest surrounding intensity is the approximate center.

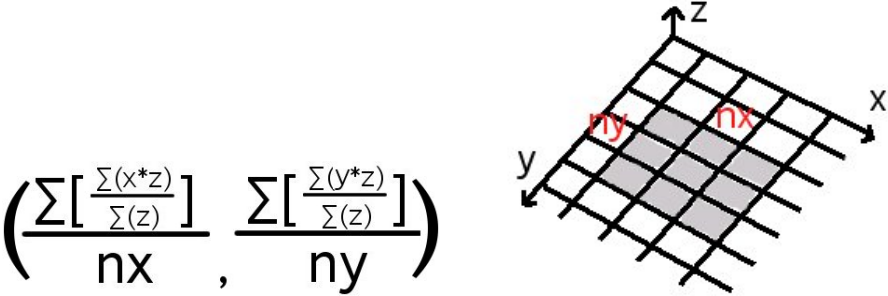


Figure 4.1: Second stage of the focus location algorithm

The location of this approximate center is then sent to the second stage of the process, which uses the formula shown in **Figure 4.1** to obtain the spot center (x,y) as the centroid (weighted average) over a region of nx by ny pixels. Here, x represents the X coordinate, y the Y coordinate, z the pixel intensity, and nx and ny the number of rows and columns checked, respectively. This method has been found to be highly accurate.

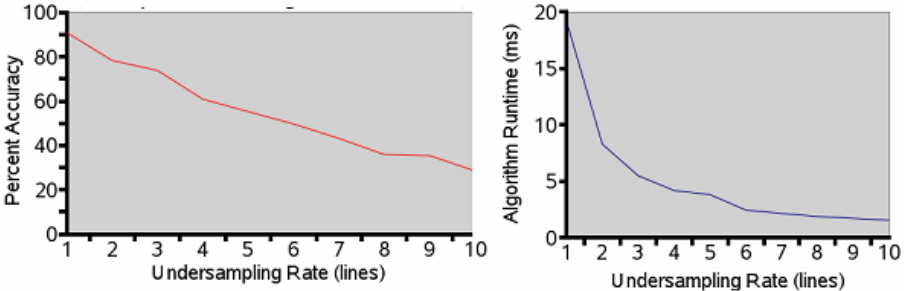


Figure 4.2: Accuracy and runtime for spots with a varying undersampling rate

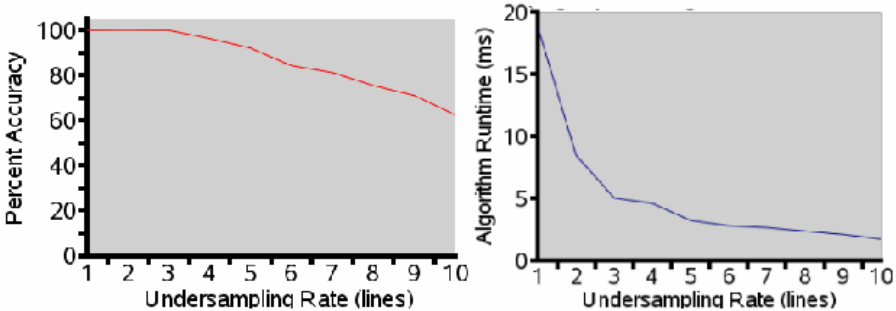


Figure 4.3: Accuracy and runtime for large spots with a varying undersampling rate

The main factor determining the efficiency and runtime of this algorithm is the undersampling rate n. The program allows the user to set the rate up to 10, which means that every 10th line is

checked. The algorithm was run one thousand times at each undersampling rate, with noise levels and spot-center locations randomized. **Figure 6.2** shows two generated images used in this testing process. The percent accuracy, or average error over the thousand runs when attempting to locate the center, and the associated runtime are shown in **Figures 4.2** and **4.3** as functions of the undersampling rate. A balance between efficiency and accuracy must be determined. Clearly, the larger the focal spot, the greater one can afford to increase the undersampling rate and still remain accurate, thereby saving CPU cycles.

4.3 Focal-measurement Algorithm

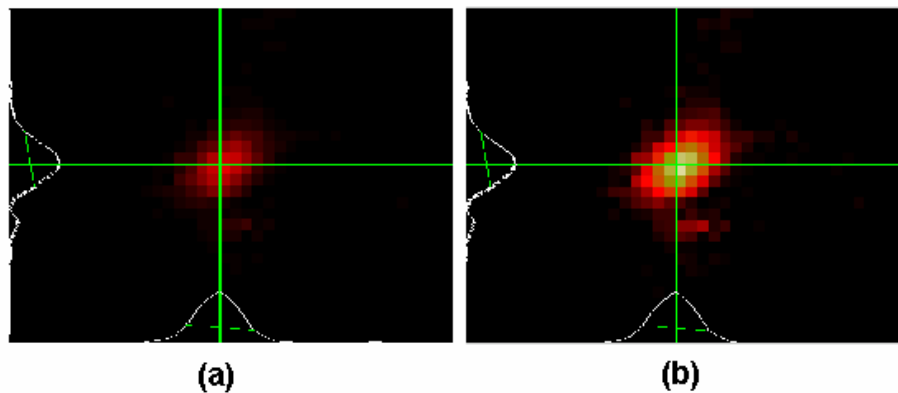


Figure 4.4(a): Experimental image of a focal spot, indicating the center of the spot and lineouts through the center of the spot in the horizontal and vertical directions

(b): Autoscaled image, with the center intensity scaled to 256.

An experimental focal spot is shown in **Figure 4.4(a)**, needing to be measured and autoscaled so that it might have a contrast that is easier to view.

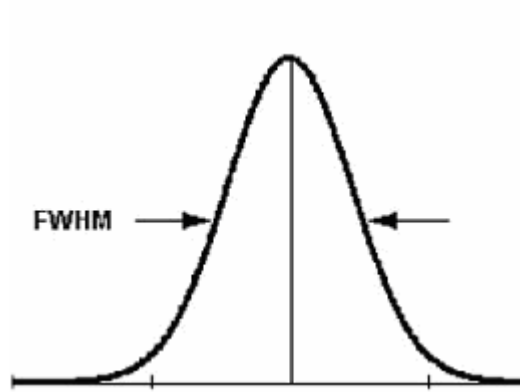


Figure 4.5: Full width at half maximum for a given curve¹⁰

When characterizing a focal point, knowledge of the full width at half maximum (FWHM) is often very useful. This value, indicated graphically in **Figure 4.5**, is the distance between two points on a curve whose value is half that of the maximum value of the curve.¹¹ The algorithm goes through the following process: First, the intensity at the located focal center is obtained and the half-maximum value is calculated. Second, the algorithm traverses through the data vertically and horizontally until the points equal to or less than the half-maximum value are found. Noise is avoided in this step by checking points beyond the point in question to see if a decrease in intensity is consistent or rather noise-induced. Third, the distance between these two located points is calculated. The thin green lines shown in **Figure 4.4** indicate the FWHM.

The ability of the program to auto-scale image data is often imperative to providing a viewable image contrast. An algorithm to auto-scale pixel intensities has been developed. It calculates the auto-scaled intensity I' as $I \cdot (256/m)$ where I is the original intensity and m is the intensity at the focal center. The auto-scaled image of **Figure 4.4(a)** is shown in **Figure 4.4(b)**.

5 Program Design

DTControl follows the object-oriented model of programming, creating various objects that carry out different tasks. **Figure 5.1** shows DTControl's class layout, subdivided into classes of similar purpose.

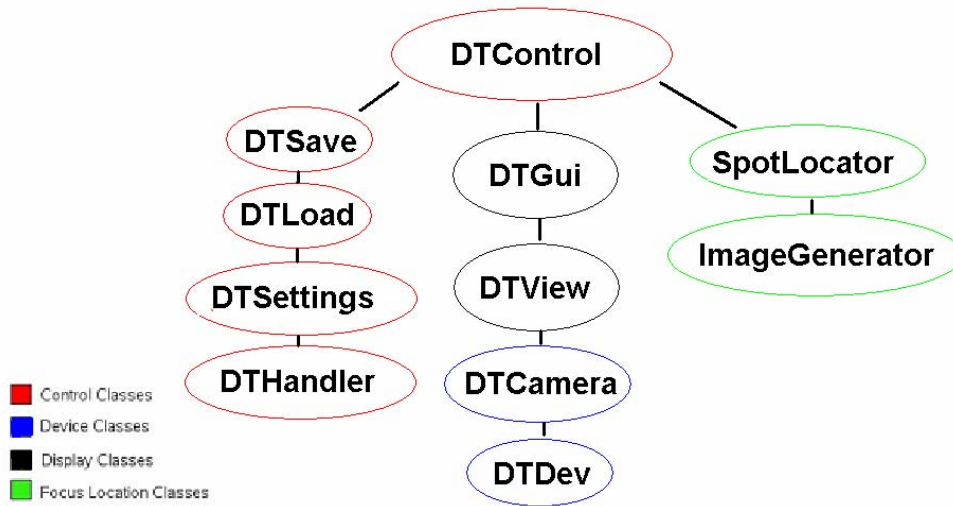


Figure 5.1: Program class hierarchy, subdivided into objects serving various purposes

The device classes provide an interface for accessing a CCD camera. They include DTCamera, which represents a CCD camera, containing data structures to hold image data and abstractions to acquire images, and DTDev, which provides access through the Java Native Interface to a C library. This library interfaces with a Linux driver that provides access to a DT3155 framegrabber.

The display classes are associated with the proper interpretation and display of data acquired from device classes. They include DTGui and DTView. DTView is responsible for displaying the information from one DTCamera. DTGui represents the entire user interface of the program, and assembles and displays a DTView and other components.

The focus location classes are responsible for the implementation of the focus location algorithm. SpotLocator provides algorithms for locating the laser spot and for calculating the FWHM values. ImageGenerator generates random images that are used to simulate laser focal spots.

The central classes control and synchronize other program features. DTSave and DTLoad save and load still images and DTSettings provides access to many program settings. Finally, DTControl controls all other classes and synchronizes GUI and camera updates.

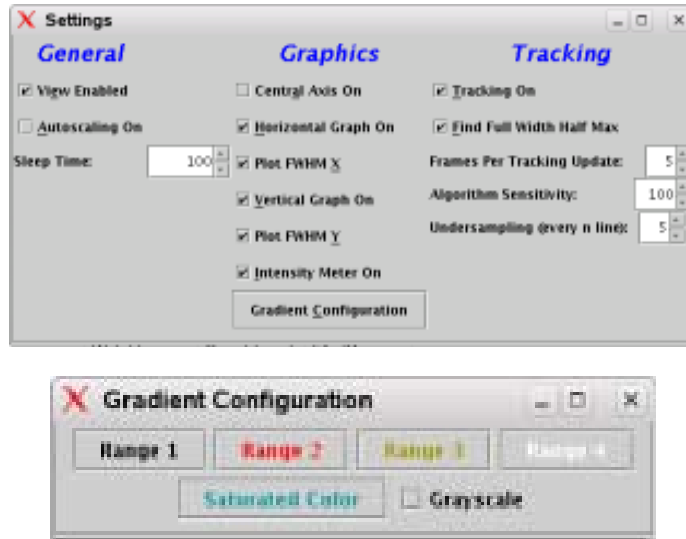


Figure 5.2: The user interface and options, designed to be self-intuitive

A user interface has been developed that allows the user to select many features. Selecting an appropriate color gradient for images such as **Figure 4.4** is important, as protective glasses used in laboratories often block certain colors. Color gradients, as well as the undersampling rate and algorithm sensitivity, can be changed by the user. Other features, such as a pixel intensity bar, displayed graphs, the calculation of FWHM values, the display of axes, and more, can also be enabled and disabled.

6 Program Testing

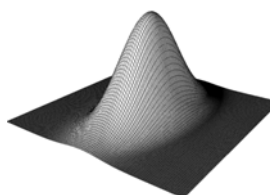
$$I = I_0 e^{-\left(\frac{(x-x_0)^2}{2\sigma_x^2} + \frac{(y-y_0)^2}{2\sigma_y^2}\right)}$$


Figure 6.1: A two-dimensional Gaussian function¹²

A process whereby the program could be tested outside the real environment was needed

because it wasn't always possible to test the program in the real environment. The program was given the capability to generate virtual images to display from a virtual CCD camera. These images were composed of a two-dimensional Gaussian function (see **Figure 6.1**) with added noise, which produces a very natural distribution that appears as an ideal focal spot. The noise was added by augmenting a random number of pixels, between 0 and 1/5 of the image's area, by a random value between 1 and 255. Examples of such images are shown in **Figure 6.2**, **6.2(a)** with tracking enabled and **6.2(b)** with tracking disabled.

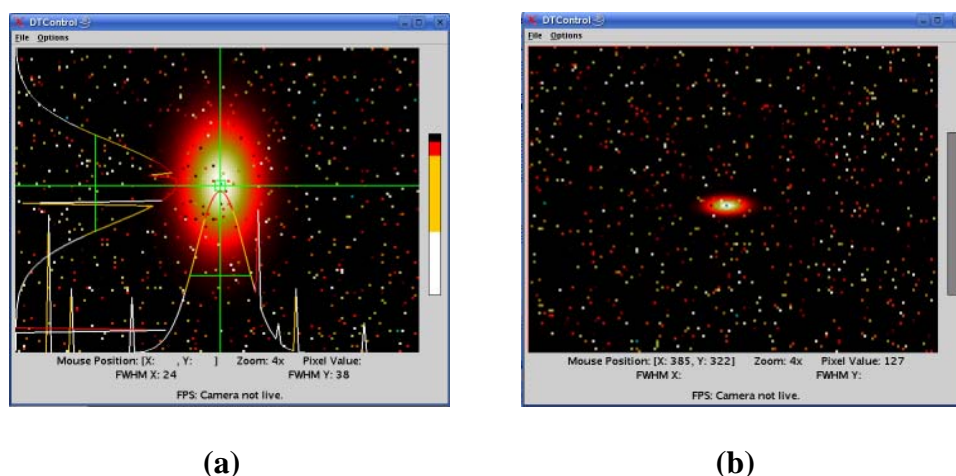


Figure 6.2: Test images produced from two-dimensional Gaussian functions with added noise.

(a) Tracking enabled; (b) tracking disabled.

7 Conclusion

Short-pulse laser plasma interaction experiments are carried out within LLE. They require a program that can locate and characterize a laser focal spot in real time. Such a program has been developed using the C and Java programming languages. The design of the program assigns different roles to various objects, creating a structured design that is easy to upgrade or alter in the future. The program and its various algorithms have been tested and proven to be accurate in both simulated and real laboratory environments. The program has already been used in the alignment and testing of lasers within LLE's Laser Development Laboratory and will continue to be used

during experiments at LLE.

8 Acknowledgments

I would like to thank my advisor Dr. Christian Stoeckl for his guidance, hints and words of advice during the progression of this project. I would also like to thank Dr. R. Stephen Craxton for providing the opportunity to pursue research at The University of Rochester's Laboratory for Laser Energetics this past summer.

9 References and Sources

1. DT3155 – Full Specification. Data Translation, Inc. 16 Aug. 2006
<http://www.datx.com/products_hardware/prod_dt3155_spec.htm>.
2. Online Image. CCD Camera. 6 Oct. 2006
<http://www.ni.com/third_party/sony/pdf/xcsT70_ce.pdf#search=%22xcst70_ce%22>.
3. DT3155 – Full Specification. Data Translation, Inc. 16 Aug. 2006
<http://www.datx.com/products_hardware/prod_dt3155_spec.htm>.
4. Online Image. Computer Clip Art. 14 Aug. 2006
<<http://www.sbac.edu/~tpl/clipart/Technology%20and%20Machines/computer%2001.jpg>>.
5. DT3155 Framegrabber Linux Device Driver. Version 1.8. <<http://sourceforge.net/projects/dt3155a>>.
6. The Linux Kernel Archives. <<http://www.kernel.org>>.
7. Kabutz, Dr. Heinz. Java History 101: Once Upon an Oak. 30 Jan., 2003. 24 Aug. 2006
<<http://www.devx.com/Java/Article/10686/0/page/1>>.
8. Aitken, Peter. Learning C. Carmel: SAMS, 1991.
9. Stearns, Beth. Trail: Java Native Interface. 21 Aug. 2006 <<http://www.iut-info.univ-lille1.fr/docs/tutorial/native1.1/index.html>>.
10. Online Image. Full-width at half-maximum. 10 Aug. 2006
<http://cfao.ucolick.org/EO/steinb/education_outreach/demoweb/home/FWHM.gif>.
11. Weisstein, Eric W. "Full Width at Half Maximum." MathWorld-A Wolfram Web Resource. 10 Aug. 2006
<<http://mathworld.wolfram.com/FullWidthatHalfMaximum.html>>.
12. Online Image. 2d gaussian. 16 Aug. 2006
<<http://local.wasp.uwa.edu.au/~pbourke/other/distributions/gaussian6.gif>>.

Neutron Transport Calculations Using Monte-Carlo Methods

Sean Lourette

Neutron Transport Calculations Using Monte-Carlo Methods

Sean Lourette
Fairport High School
Advisor: Christian Stoeckl

Laboratory for Laser Energetics
University of Rochester
Summer High School Research Program
2006

Abstract

Fusion reactions from direct-drive inertial confinement fusion experiments at the Laboratory for Laser Energetics (LLE) release large amounts of stored nuclear energy. Most of it is given off as energetic neutrons. Plastic scintillators are used as detectors for these neutrons. The neutrons that interact with the scintillator produce photons that are recorded using a photomultiplier tube on a fast oscilloscope. The detector has a lead shield used to block x-rays that would flood the detector with energy. The neutrons travel throughout the target area interacting with several structures, such as the chamber wall, that significantly affect the neutron transport. In order to understand the effects of the target chamber and lead shield on the detected neutron signal, a Monte-Carlo simulation program (Geant4) was used to simulate neutron interactions. Geant4, a toolkit designed to calculate particle interactions with matter, is used predominantly in high-energy, nuclear, and accelerator physics. By changing the geometric dimensions and material properties of the structures in the target area, effects that cannot be tested experimentally have been simulated. It was found that the lead shield and the target chamber have a minimal effect ($< 1\%$) on the full width at half maximum (FWHM) of the neutron signal.

1. Introduction

The long-term goal of fusion research is to design a sustainable fusion energy source that can produce energy cleanly from common fuel sources. The Laboratory for Laser Energetics conducts most of its experiments and research on the OMEGA laser system, which consists of 60 symmetrically oriented, high-power laser beams focused onto a target to obtain internal confinement fusion. The targets are composed of frozen hydrogen isotopes deuterium (^2H) and tritium (^3H), the most common reactants for fusion reactions. When the nanosecond laser pulse strikes the target, the outer shell rapidly expands, compressing and heating the fuel creating temperatures similar to those in the center of sun.

1.1 Neutron Production

Most of the energy from fusion reactions is given off in the form of energetic neutrons. These neutrons can be created by two distinct types of fusion reactions: deuterium-tritium (DT) and deuterium-deuterium (DD). DT reactions yield a 14.1 MeV neutron and a 3.0 MeV alpha particle, while DD reactions yield either a 2.45 MeV neutron and a 0.825 MeV helium-3 nucleus, or a 3.0 MeV proton and a 1.0 MeV triton.¹

In order for the reaction to occur, the relative velocity of the reactants must be large enough to overcome the Coulomb force and release the stored nuclear energy. This energy is distributed between the two products as given above; however, since the net momentum of the reactants is not constant, the actual distribution of the energy between the two products varies in order to conserve momentum and energy. The resulting neutrons from each type of reaction (DD, DT) have a Gaussian distribution of energy such that the mean energy is equal to either 2.45 MeV (for DD) or 14.1 MeV (for DT). The width of the energy distribution is proportional to the square root of the temperature of the reactants. This temperature is significant because a high plasma temperature is necessary for the fusion reactions to occur.

1.2 Neutron Detection

In order to measure the width of the spread of neutron energies, the OMEGA laser system uses plastic scintillators (Bicron BC-422Q²) to measure the spread in the neutron time of flight, which can be correlated to a distribution of energies. To prevent the intense bremsstrahlung that would be produced in the detector from x-rays, a lead shield is placed directly in front of the detector. The cross section between x-rays and lead is much greater than the cross section between neutrons and lead, greatly decreasing the intensity of the x-rays entering the scintillator while having a significantly smaller effect on the neutrons. Neutrons produce a photon signal in the scintillator by transferring energy to a nucleus (hydrogen or carbon), whose electrons are ionized from the energy. These ions and electrons excite and de-excite nearby atoms, emitting photons, which are converted to current in a photocathode. The current is amplified using a microchannel plate and measured with a fast oscilloscope.³ Figure 1 illustrates this process.

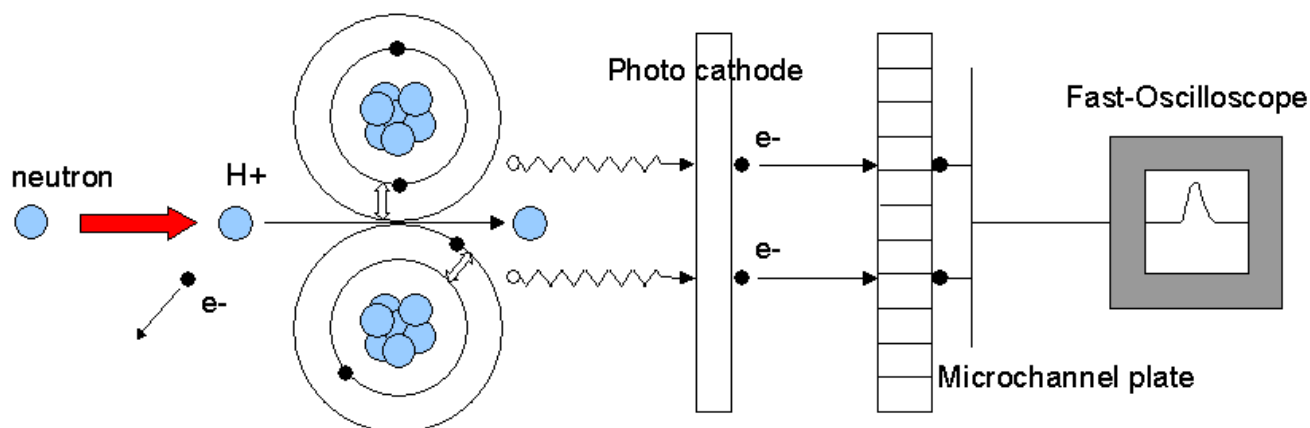


Figure 1: Scintillation process – A neutron collides with the nucleus of an atom such as hydrogen. The atom becomes ionized and excites and de-excites nearby atoms, emitting photons. The photons generate current in a photocathode. The current is amplified by a microchannel plate and read by a fast oscilloscope.

Although the lead shield reduces x-ray data, it also scatters neutrons, which could significantly alter the FWHM, used to measure the time of flight spread of the arriving neutrons. Because the detector requires the lead shield in order to collect data, the effect of the shield on the neutron signal

cannot easily be determined experimentally. It is also extremely difficult to determine theoretically. The same holds true for the aluminum target chamber, which is required to create a vacuum to ensure that the focused laser energy reaches the target with its beam quality preserved. The primary goal of this study is to model the effects of the target chamber and lead shield on the neutron time of flight spread.

1.3 Geant

Geant⁴ is a Monte-Carlo simulation toolkit for the passage of particles through matter. A Monte-Carlo simulation uses random or pseudo-random numbers and interaction probabilities to simulate an experiment. Geant tracks the energies of each particle (projectile) until it decreases below a certain value known as the “cut value.” At this point, Geant no longer tracks that energy and disperses it among the local particles, increasing the thermal energy of the volume. Any particle near a boundary is tracked below the cut value because there is a significant probability that the particle will travel into the next volume. Geant allows the user to select different physics processes, cut values, magnetic fields, material types, and many other settings in order to simulate the desired experiment. Like an experiment, Monte-Carlo simulations generate data that requires statistical analysis. The simulations also require extended runtimes in order to create meaningful data.

2. The Program

Using the Geant toolkit, a program was written to simulate the neutron transport in the target area. The LHEP⁵ physics library was used to manage the physics processes, including hadronic and electromagnetic processes. The hadronic processes model strong-force interactions between neutrons and nuclei, while the electromagnetic processes model the ionization of electrons. The conversion from electron energy to photon energy was not modeled because the conversion efficiency is known to be a constant ratio.

The program constructs geometries and their corresponding materials, representing the structures in the target area that contribute the most to neutron scattering. The dimensions and materials are shown in Figure 2. Figure 3

illustrates the structural setup. The concrete walls have a minimal effect on the neutron detection and were added for completeness. The neutrons that do scatter off the chamber walls and reach the detector arrive much later than the significant neutron signal. The scintillator was constructed as a “sensitive detector” meaning that it records energy deposited within the volume by each particle. The program records specific information for each quantity of energy deposited that can be statistically analyzed.

For all simulations, 14.1 MeV mono-energetic neutrons were projected from the center of the target chamber. Mono-energetic neutrons were used to clearly observe the extent of the neutron scattering.

Dimensions

Room Length = 30 m
Room Width = 15 m
Room Height = 15 m

Chamber Thickness = 8.89 cm
Chamber Outer Diameter = 6 m

Detector Distance
from Target = 12 m

Detector Diameter = 4 cm
Detector Height = 1 cm
Shield Diameter = 4 cm
Shield Height = 2 cm

Materials

Detector Material = Plastic
Chamber Material = Aluminum
Wall Material = Concrete
Room Material = Air
Shield Material = Lead

Figure 2: Default dimensions and materials used for the simulations.

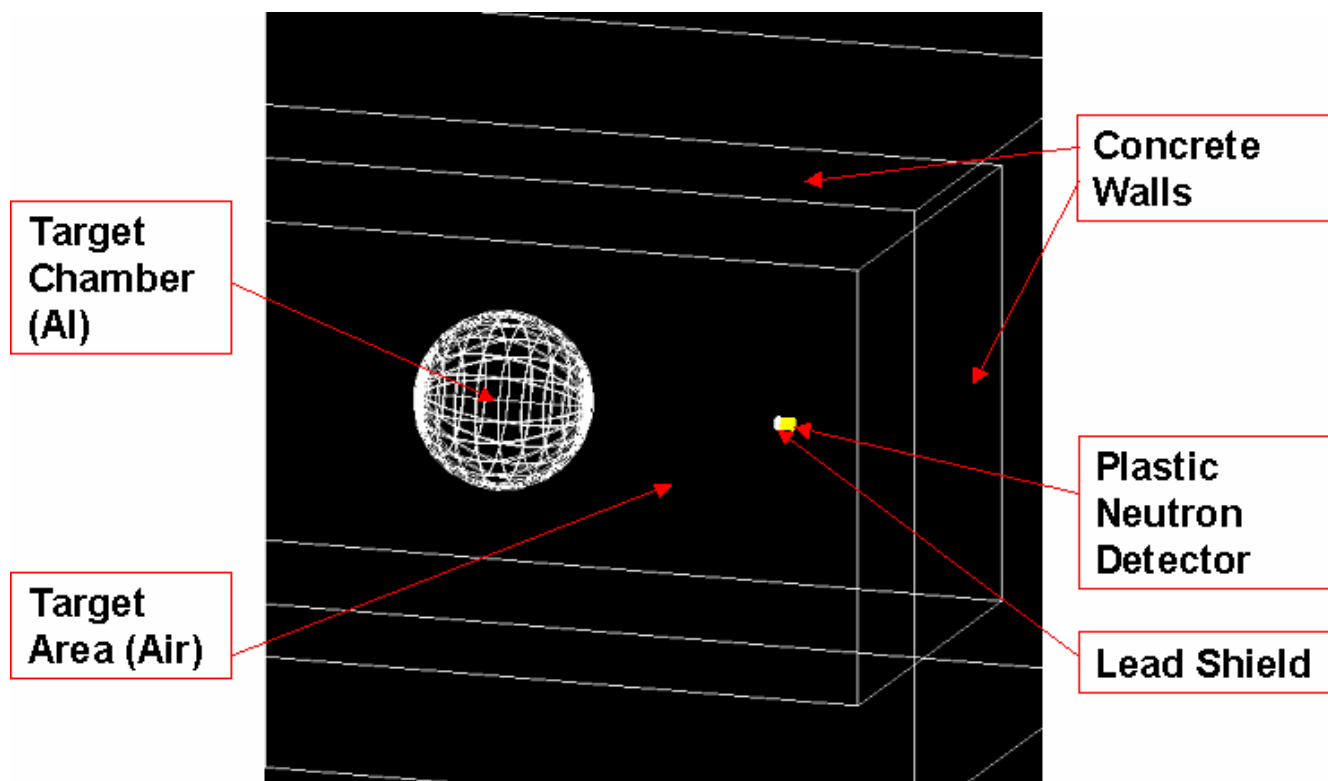


Figure 3: Materials used in the program – Each region was assigned a material with a temperature, density, and pressure.

3. Test Simulations

In order to confirm that the results produced by Geant are accurate, two simple tests were performed. In each test, all materials except the detector itself were changed to vacuum, and mono-energetic neutrons were launched directly at the detector. In the first test (Figure 4), which measured the energy deposition over time, the results were as expected. At the front of the signal, there is a very steep increase in the deposition energy. The signal then decreases exponentially over time until the neutrons reach the end of the detector, when the signal drops sharply. The remainder of the graph is background generated by neutrons that lose some of their energy near the front and deposit additional energy near the back at a time after the signal drop. The 0.8 ns FWHM correctly corresponds to the height of the 4 cm detector divided by the speed of a 14.1 MeV neutron (5.14 cm/ns).

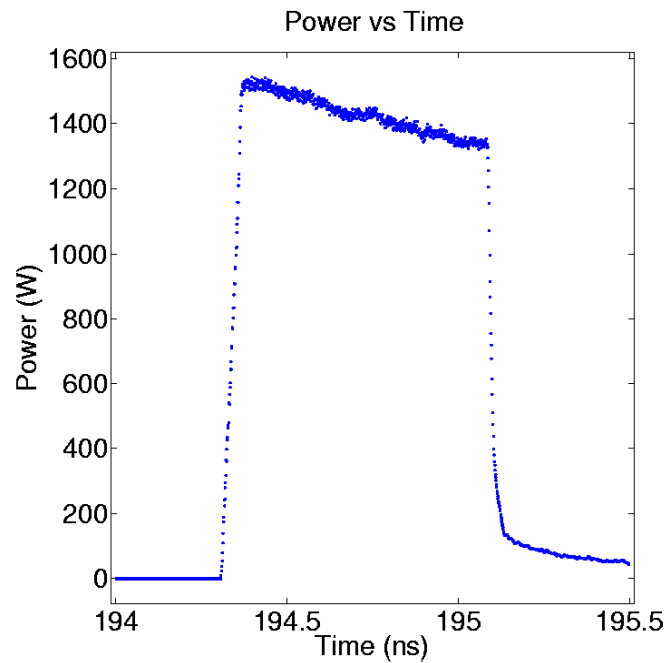


Figure 4: First Test – Energy deposition signal for 14.1 MeV neutrons through a 4 cm detector placed 10 m away from the target. The sharp rise and drop of the signal correctly correspond to the times at which the non-interacting neutrons pass through the detector. Between these times, the signal drops off exponentially.

A second test was performed to calculate the mean-free path of neutrons through a plastic scintillator. The detector was lengthened to 200 cm and all other conditions were the same as in the first test; however, instead of recording the energy deposition, the distance traveled by each neutron before its first interaction was recorded. The data was used to create a graph (Fig 5) of the percentage of non-interacting neutrons (y) versus length (x). The graph is well fit by an exponential of the form: $y = e^{-x/b}$, where b is the mean-free path. The mean-free-path value produced by Geant is 11.00 cm, while the literature value is 10 cm.⁶ This favorable comparison confirms that Geant is producing meaningful data.

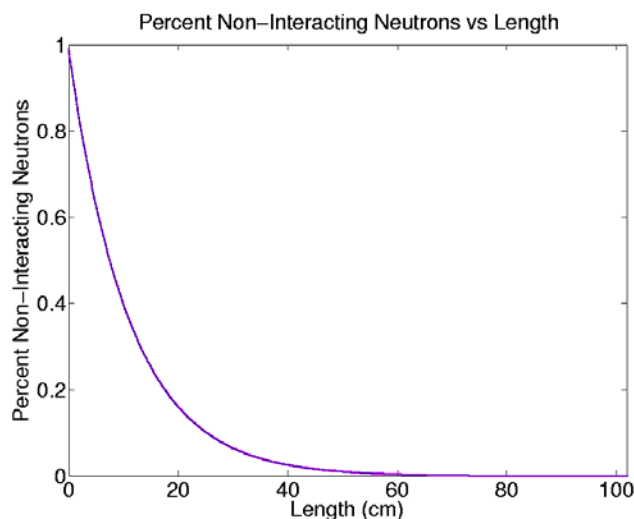


Figure 5: Second Test – The attenuation graph for 14.1 MeV neutrons in a plastic scintillator reveals the simulated mean free path to be 11.00 cm^{-1} .

4. Results

In order to accurately determine the effect of the target chamber and lead shield on the neutron signal, one must consider all angles (4π steradians) of initial trajectories; however, this would produce limited data because the detector is so far away from the neutron source. When the detector is 2 cm in radius and 12 meters from target, one out of every 1.44×10^6 neutrons will be initially launched toward the detector. Although it is clear that the average neutron traveling toward the detector will deposit much more energy than the average neutron traveling in a different initial direction, it is questionable whether the average neutron traveling toward the detector will deposit more energy than 1.44 million neutrons traveling in different directions.

Two simulations using all of the default conditions (Figure 2) were performed in order to address this question. The first simulation used neutrons with initial direction varying less than 0.1 degrees from the direction of the detector, which corresponds to a solid angle of 9.57×10^{-6} steradians (encompassing the entire detector). The second simulation used neutrons with all other initial directions. When comparing the energy deposition per neutron density (neutrons per solid angle), it was

found that the first simulation accounted for 27% of the energy deposition over all angles; however, when considering only the energy deposition occurring during times of significant signal strength (233 ns to 234 ns), the first simulation accounted for 96% of the total energy deposition. This allows simulations to be performed using a millionth of the neutrons (and one millionth of the run time) while sacrificing only 4% of the significant deposition. Figure 6 shows the visualization created by Geant of the neutron scattering.

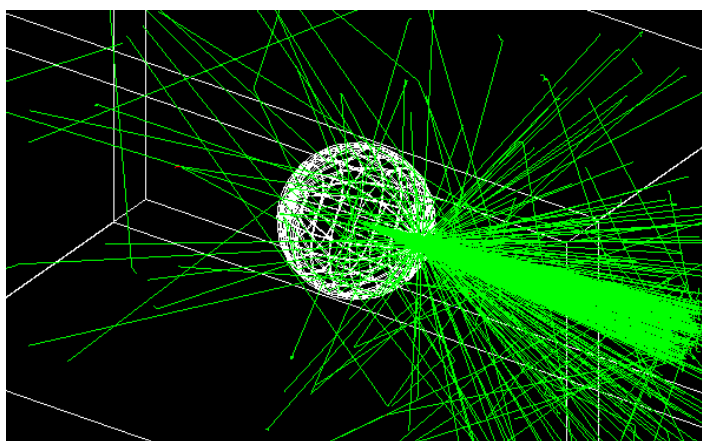


Figure 6: Neutron Scattering – Neutrons (green) with directions within a cone (increased solid angle for visualization) are scattered by the target chamber. The majority of scattered neutrons are deflected by a small angle (< 45 deg).

In order to determine the effects of the lead shield and the target chamber on the neutron signal, three simulations were performed. The first used neither the lead shield nor the target chamber, the second used the lead shield, and the third used both. Each simulation used 14.1 MeV mono-energetic neutrons with incidence angles within a 0.1-degree cone. In order to accurately compare the shapes of the signal graphs, each graph was normalized to 1 at its maximum intensity, as shown in Figure 7. Figure 8 shows the ratio of the signal graph with the specified structure to the signal graph without the specified structure. The plot for the shield and target chamber (blue) appears to have a constant value of 1 with noise at either end. From this, it can be inferred that the target chamber has a minimal effect on

the signal from neutrons with incidence angles within a 0.1-degree cone. The lead shield (green) appears to have a greater effect on the background signal. Although 4% of the neutrons that have incidence angles outside the 0.1-degree cone hit the detector between 233 ns and 234 ns, a significantly smaller percentage hit the detector between times of 233.5 ns and 233.8 ns. It can be presumed that this will not significantly alter the neutron time of flight spread. The effect of the lead shield and the target chamber on the FWHM from neutrons with incidence angles within the 0.1-degree cone is less than 1%.

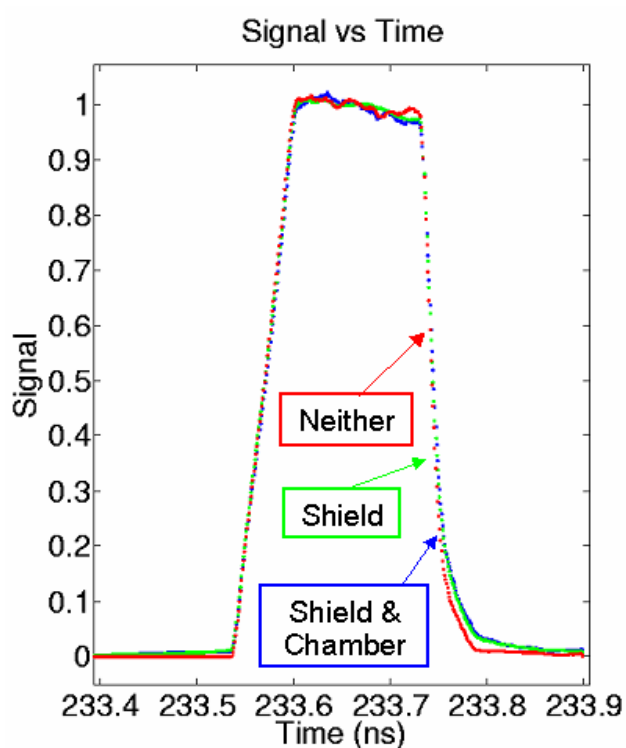


Figure 7: Relative signal strengths for 14.1 MeV neutrons in a 1-cm detector passing through various materials.

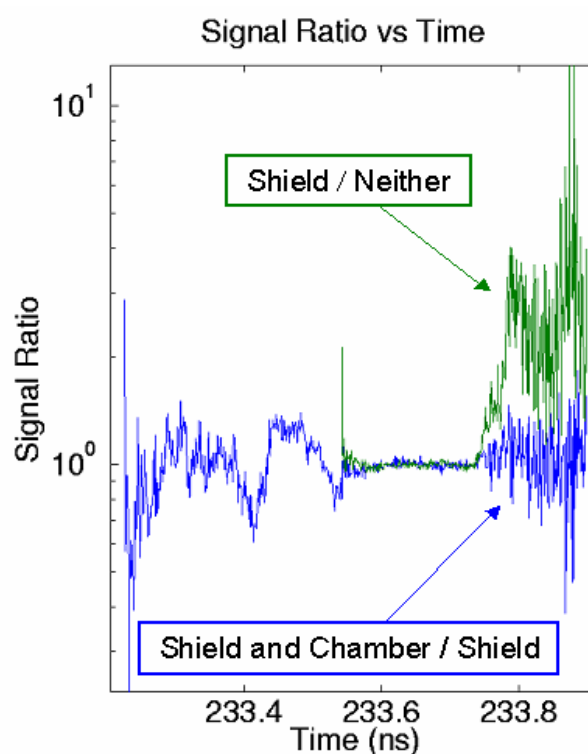


Figure 8: Ratios of signal strengths from Figure 7.

5. Conclusion

A Monte-Carlo simulation program was used to simulate neutron interactions in order to understand the effects of the target chamber and lead shield on the detected neutron signal. The neutron signal can be used to determine the initial velocities of the reacting ions or the temperatures required

for fusion. It was determined that the lead shield creates more neutron background than the target chamber creates for 14.1 MeV neutrons with initial velocities within a 0.1-degree cone. It was also determined that neither structure significantly alters ($< 1\%$) the full width at half maximum (FWHM) duration of the signal.

6. Acknowledgements

I would like to thank my advisor Dr. Christian Stoeckl for his support and guidance, which made this project possible. I would also like to thank Dr. Orlin Gotchev for teaching me how to set up and use Geant. Finally, I would like to thank Dr. Stephen Craxton, who made this entire experience possible by accepting me into the High School Summer Research Program.

7. References

- [1] Los Alamos National Laboratory, **Physics Division Progress Report**, Page 70 (1995)
- [2] Bicron Newbury, Newbury, OH 44065-9577
- [3] Wide-Dynamic-Range “Neutron Bang Time” Detector on OMEGA, **LLE Review** Volume 88, Page 171 (2001)
- [4] Geant, <http://cern.ch/geant4>
- [5] Laboratory for High Energy Physics, University of Bern, Switzerland
- [6] Dick Lerche, private communication (1997)

**Precision Flash Lamp Current Measurement—Thermal Sensitivity
and Analytic Compensation Techniques**

Ben Matthews

Precision Flash Lamp Current Measurement –Thermal Sensitivity and Analytic Compensation Techniques

2006 Summer Research Program
By Ben Matthews
Advisors: Greg Brent, David Lonobile

Abstract:

For multiple-beam direct-drive laser fusion to occur it is essential that each laser beam hits the target with the same force. To help achieve this, the pump power provided to the flash lamps within the laser amplifiers is precisely monitored using a waveform digitizer module (WDM) designed at the University of Rochester's Laboratory for Laser Energetics (LLE). Temperature changes within the WDM induce errors. In order to measure and reduce these errors a test stand has been constructed to accurately and automatically measure the effects of temperature on the digitizer. The test results provide a basis for the development of an analytic temperature compensation code for the WDM's onboard FPGA (Field Programmable Gate Array), which is expected to greatly improve the accuracy of pump power readings at varying temperatures.

Background:

All electronic devices have a certain degree of sensitivity to temperature changes, referred to as their temperature coefficient. All precise electronic measurement devices require some level of compensation for this. This applies to the precise measurement of the current provided to the flash lamps in the laser amplifiers in the Omega EP laser system (see figure 1). It is essential that each amplifier receive the same amount of pump energy so that it produces a consistent output. Without precise control of the output from each amplifier, some of the laser beams may be more powerful than others.

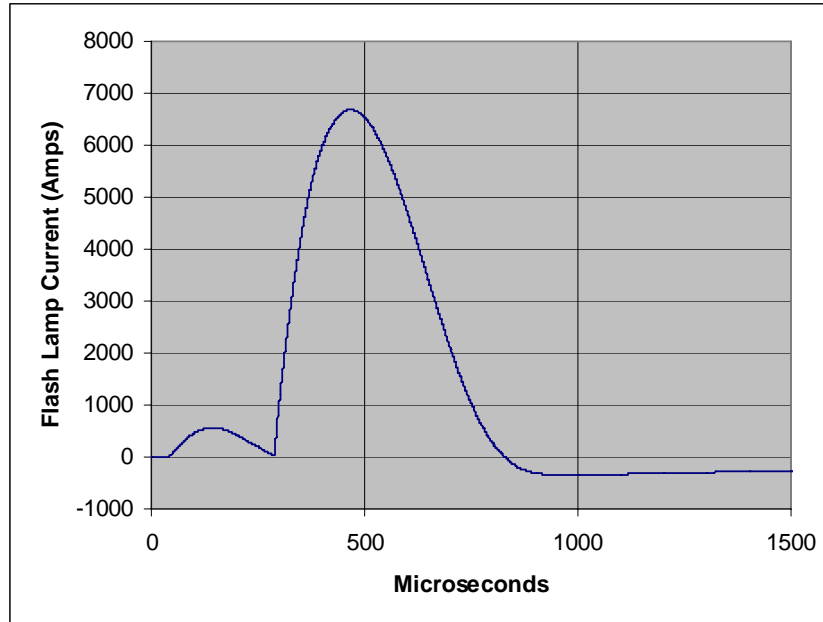


Figure 1:

A typical measurement illustrating the current waveform provided to the flash lamps.

The waveform digitizer module, or WDM (see figure 2), is the device that measures the current waveform provided by the power conditioning units (PCU's) to the flash lamps. This device comprises seventeen, fourteen-bit analog-to-digital converters which are controlled by a field-programmable gate array (FPGA). These analog-to-digital converters measure the voltage collected by current sense transformers on the flash lamp power cables in order to determine the current being supplied. The FPGA processes and records the data being collected to the memory. This data is then collected by a single board computer for later analysis. The WDM was designed to contribute no more than a 1% error in the flash lamp waveform current measurement.

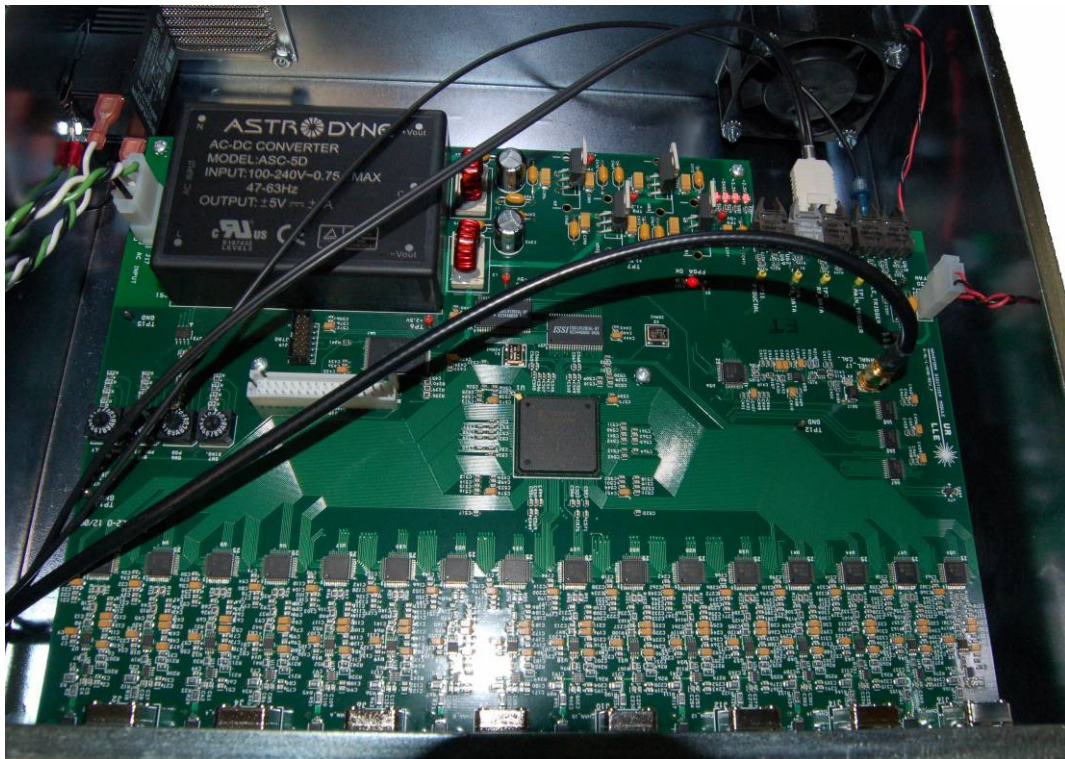


Figure 2:

The waveform digitizer module (WDM) is used to digitize and store measurements of the current provided to the laser amplifiers from the power conditioning units.

Procedure

In order to characterize and compensate the WDM for temperature changes, a test stand is needed. To develop a test stand a few major components are required: a way to regulate temperature, a test waveform, and a way of analyzing the result. In order to efficiently characterize the WDM the process also has to be automated since a large number of boards need to be tested.

The centerpiece of the test stand is a PC104 single board computer, of the same type that controls the WDMs installed in the laser system. This computer runs custom code, written in C as part of this research project, which controls the entire test without user intervention. To regulate the ambient temperature the WDM under test is placed in an environmental chamber and connected to an amplified arbitrary waveform generator output which simulates the PCU signals. The PC104 computer sets the environmental chamber to the desired temperature through an RS-232 (serial) connection. After the WDM has had time to reach thermal equilibrium, data is automatically collected from both a control WDM at room temperature and the WDM in the chamber. The arbitrary waveform generator is then turned off and the process is repeated at another temperature. The software also takes into account a correction factor to correct for environmental chamber errors. This factor was calculated early in the test stand development using a LabView program and sensors similar to those used on the WDM which were mounted throughout the chamber. In order to accurately find the effect that temperature has on the WDM it is tested at a wide range of temperatures, from about 10°C to about 70°C. It takes approximately 24 hours to test a single WDM throughout the full range of temperatures. In order to maximize the amount of thermal characterization data being collected the test waveform is a collection of sine waves with varying frequencies and amplitudes which emulate most of the possible input signals a WDM could be expected to measure.

To help troubleshoot any problems that might occur, the test stand has some built-in debugging features. While running, the PC104 computer acquires a screenshot of an oscilloscope connected to the test stand. The oscilloscope triggers off the same trigger controlling the WDMs and test waveform generator and provides an image of both the trigger and the test waveform at each side of the test waveform amplifier. While the program is running it also displays some diagnostic information on the display of the PC104 such as the current, temperature and data storage file being written.

The WDM produces a spreadsheet containing the waveform being digitized on a sixteen-bit scale. The large number of sample points makes any sort of non-graphical analysis tedious. As a result, as much analysis as possible has been automated. A C parsing program has been written to reduce the data by extracting the amplitudes of each waveform and calculating the deviation from the control data. To calculate the effect temperature has on the WDM's DC offset (measurement with no signal), a script was written for the UNIX utility GAWK.

Results:

While additional WDM's need to be tested, there are some encouraging early results shown in figure 3. In terms of both DC offset and gain, the WDM's error seems to change linearly. On average, the DC offset changes by 1.35 amps per degree Celsius.

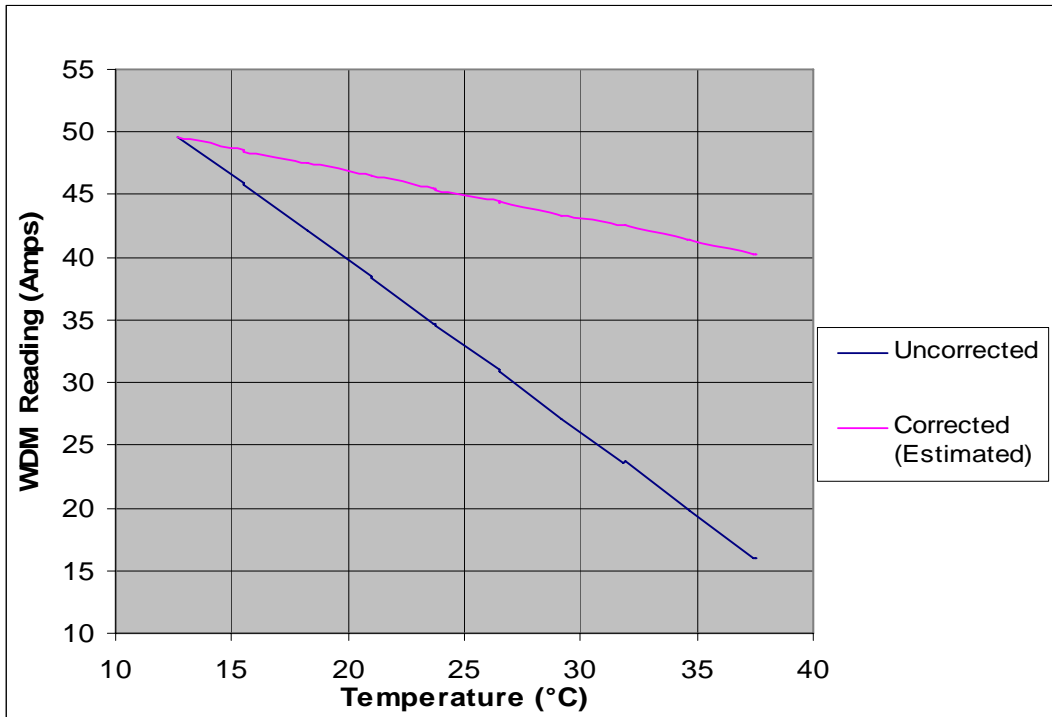


Figure 3:

This graph shows the WDM's DC offset at different temperatures. The pink line shows the WDM corrected with an average correction factor. The average correction factor is not perfect due to variations between boards.

Similarly, the signal sensitivity of the WDM when it is driven with sine waves (based on peak amplitude), is a linear result, with a slope of about -1.5 amps per degree Celsius (see figure 4).

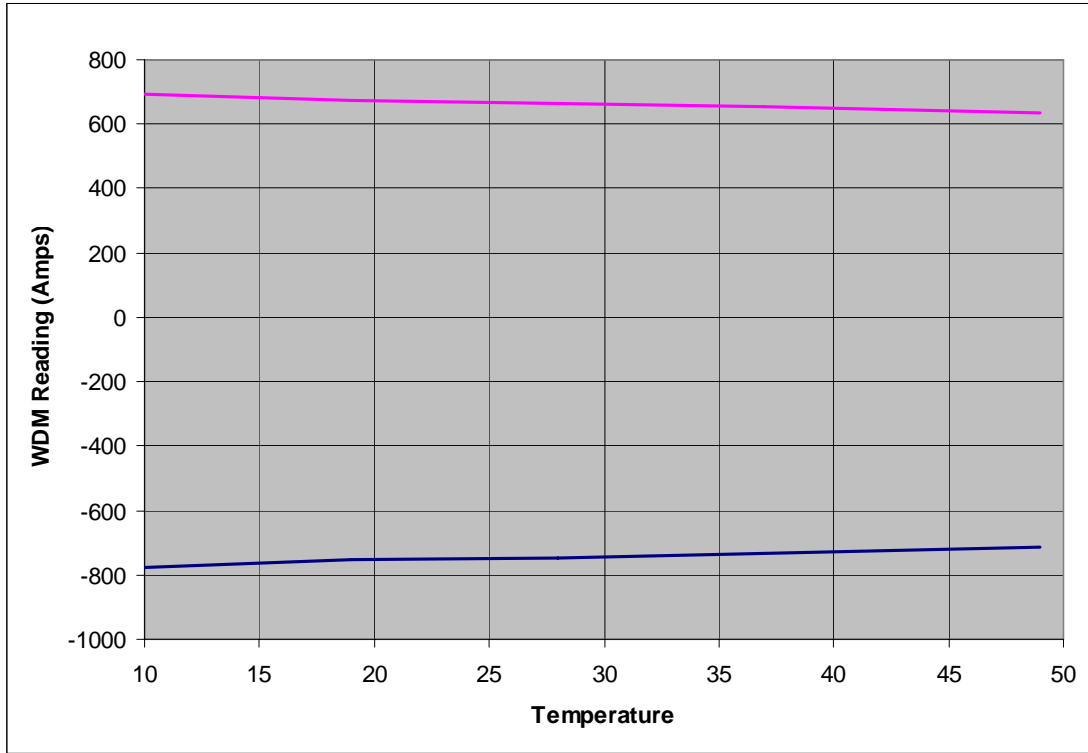


Figure 4:

This graph shows the amplitude measurement deviation of the test WDM from a room temperature WDM at both positive and negative peaks. The large deviation is caused by differences in calibration between the two devices. The slope of the lines is all that is of concern.

Compensation:

Since the temperature-induced error experienced by the WDM is linear with temperature, it is easy to correct for. To correct for DC offset drift, a code module has been written for the WDM's onboard FPGA. The algorithm is simply to add to the current reading the product of a calibration coefficient and the difference between the actual and calibration temperatures. Because an FPGA is used instead of a microcontroller this compensation can be performed in real time, needing to be computed only once per laser shot. The code to implement this compensation routine was written in the high level description language VHDL.

An algorithm and code for correction of gain changes versus temperature that affect the precise measurement of time varying waveforms by the WDM has not yet been written. This should be straightforward resulting from the linear nature of

this thermal effect on the WDM. This will likely be a C program run by the PC104 PCU control computer to post-process the data coming from the WDM.

The WDM assemblies tested as part of this project seem to behave similarly with respect to thermal dependence. However the number of boards sampled is small, making it difficult to know whether a single compensation constant can be used or whether it will be necessary to test and compensate each board individually. If it turns out that each board must be compensated individually, it is possible to compute a correction factor for each board and store it in the PCU control PC104 computer's storage for correction during post-processing after laser shots.

Discussion:

Prior to the start of this project, the effect that temperature would have on the WDM was uncharacterized. The WDM is required to have no more than 1% error, making its thermal characterization of great importance. While the temperature in the capacitor bays, where the WDMs are located, rarely changes more than a few degrees, the WDMs can not be calibrated in place. The room where they are calibrated may be at a different temperature. Thus characterization and compensation of the WDM thermal effects is required. Thermal effect correction also has the potential to reduce the thermal stabilization time required for the WDMs to be within specification. Even though the error caused by temperature turned out to be only a fraction of a percent as determined in this project, it combines with other factors increasing the total error. As a result, it is important that the WDMs be characterized and compensated for any temperature effects that may occur.

Conclusion:

The waveform digitizer, or WDM, is a highly precise current measurement device. It is absolutely necessary that the flash lamp current measured by the WDM is accurate in order to achieve uniform laser energy and pressure on the target. One factor contributing to errors in the WDM measurements is the effect of temperature. In this project it was determined that the DC offset linearly drifts with temperature by as much as 1.3 amps per degree Celsius in addition to the 1.5 amps per degree Celsius of drift measured on a time varying waveform. As a result, it is important to take temperature effects into account, either as data is being collected or in post processing. A compensation routine was successfully written to correct DC offset drift in collected data within the WDM FPGA.

**Evaluation of Confocal Microscopy for Measurement of the Roughness
of Deuterium Ice**

Ryan Menezes

**Evaluation of Confocal Microscopy
for Measurement of the Roughness of Deuterium Ice**

Ryan Menezes

Webster Schroeder High School

Webster, NY

Advisor: Dr. David Harding

Senior Scientist

Laboratory for Laser Energetics

University of Rochester

Rochester, NY

Abstract:

In the direct-drive inertial fusion energy (IFE) concept, fusion targets at around 18 K are rapidly injected into a chamber filled with low-pressure Xe gas at temperatures over 3000 K. In experiments being carried out on OMEGA under the inertial confinement fusion (ICF) program, similar targets are exposed to room temperature conditions prior to being irradiated. Because it is necessary (for both IFE and ICF) that the deuterium (or deuterium-tritium) ice shell within each target remains uniform until implosion, studies characterizing damage to the layer of deuterium fuel are underway. One of these studies plans to use confocal microscopy to obtain 3-dimensional images of the ice before and during heating. In preparation for cryogenic measurements, a confocal microscope has been set up at room temperature to evaluate parameters needed for this study. Several image degradations (arcs, noise, and reflection) have been identified and investigated, and the scan parameters (image size, measurements per second, measurements per pixel, and filter settings) have been optimized for the image clarity of a 40-second scan. These parameters are required for future experiments.

1. Introduction:

In the future, fusion reactions could potentially yield clean and inexpensive electricity. The production of this energy would occur when deuterium (^2H) and tritium (^3H) react to form a helium atom and a neutron containing 14.1 MeV of energy ($^4\text{He} + ^1\text{n}$) [1]. For the energy in the neutrons to be harnessed to run steam-powered turbines in a profitable power plant, the deuterium and tritium fuel must be contained in targets which can be quickly and rapidly heated and compressed to the intense conditions required for fusion. One method that could achieve these conditions is direct-drive laser-induced inertial confinement fusion (ICF), under which

fusion targets are (in the case of direct-drive) uniformly and directly irradiated with a short laser pulse.

ICF targets contain deuterium vapor within a shell of deuterium ice. (Tritium, which is radioactive, is not usually used in experiments.)

Fig. 1 presents the structure of the targets used in OMEGA experiments at the University of Rochester Laboratory for Laser Energetics. The solid deuterium fuel helps achieve the high densities needed for fusion.

The targets must be cryogenic, since hydrogen freezes at temperatures below 20 K. Fig. 2 shows that, in comparison to ICF targets, inertial fusion energy (IFE) targets (which are designed for use in power plant situations) are larger and more complex. The ice shells in both targets must remain uniform until implosion, or hydrodynamic instabilities will prevent the target from properly imploding [2].

Both ICF and IFE target designs are subjected to heat fluxes (indicated by the symbol Q in Figs. 1 and 2). ICF targets, which are initially protected by heat shrouds, are exposed to room temperature for 0.05 to 6.0 seconds after the shrouds are removed, and before irradiation [3]. IFE targets, which are shot into the chamber (not placed in it), have a thin palladium layer that reduces blackbody radiation absorbed in the target to insignificant levels. IFE targets experience heat flux from collisions with xenon gas, which protects the chamber walls from the energy created by fusion reactions [4]. The xenon gas is at low pressures, but at very high temperatures (over 3000 °C). In both ICF and

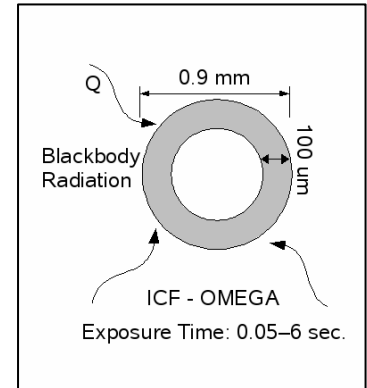


Figure 1: Schematic of a cryogenic target currently used on OMEGA

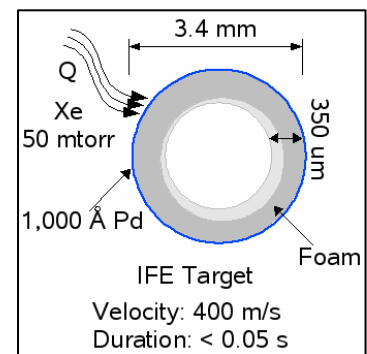


Figure 2: Schematic of a cryogenic target used for inertial fusion energy, injected at 400 m/s through 50 mtorr of Xenon

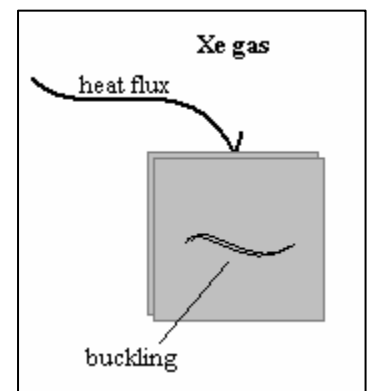


Figure 3: Diagram of buckling in heated Deuterium ice

IFE designs, the heat striking the outside of the target spreads inward, causing the deuterium ice to expand, bend, and buckle (see Fig. 3). It is necessary to understand this buckling in order to create and maintain smooth fusion targets.

Because it is difficult to image the interior of actual targets, a cryogenic setup was earlier designed to simulate heat flow and buckling. Fig. 4 is a schematic of this setup. The entire system is in a vacuum chamber, allowing for control of temperature and pressure. Within the vacuum chamber is a smaller cell, which contains 160 torr of deuterium gas and a confocal microscope (CFM) positioned to image the window at the front of the cell. This window should be cooled to 18.7 K, while the rest of the cell, including the microscope, should reach 91 K. Since the saturated vapor pressure of deuterium gas is 160 torr at 18.7 K, the deuterium condenses and freezes onto the back surface of the window, and not on the rest of the cell or on the microscope, which it could damage. Under the planned future experiment, a jet of hot xenon gas heats the front of the window. Simultaneously, the microscope images the back surface of the ice before and during buckling. A photograph of the smaller cell is shown in Fig. 5.

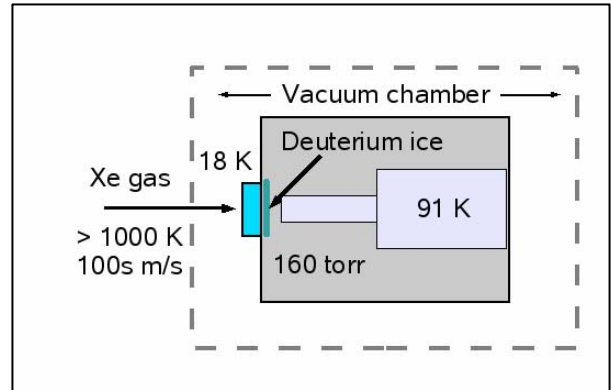


Figure 4: Schematic of the confocal microscope (light blue) within the experimental setup

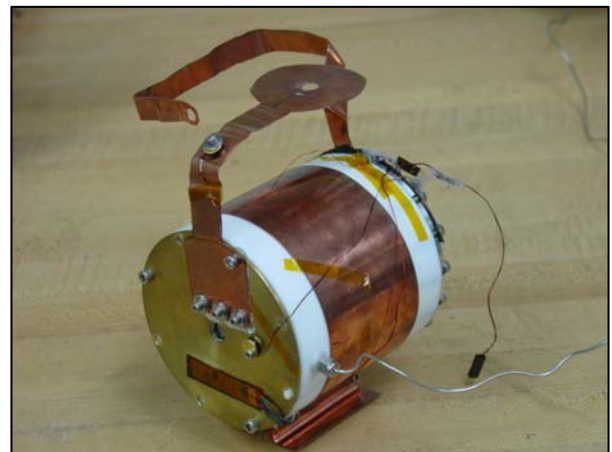


Figure 5: Photograph of the smaller cell of the experimental setup

microscope, which it could damage. Under the planned future experiment, a jet of hot xenon gas heats the front of the window. Simultaneously, the microscope images the back surface of the ice before and during buckling. A photograph of the smaller cell is shown in Fig. 5.

2. Confocal Microscope:

Fig. 6 illustrates the principle of confocal microscopy. A focused laser beam (red)

illuminates a small point on the sample. The reflected light (green) travels back through the lens.

All of the light passing through the lens that originates from the point on the sample enters the end of the optical fiber, while any out-of-focus light does not enter the optical fiber. A detector then measures the in-focus light. (The strength of this signal corresponds to the height of the point on the sample directly below the fiber.) Fig. 7 is a photograph of the microscope that will be used in the planned experiment. The piezoelectric scanner, which can be seen at the bottom of the microscope stack, is a key component of the microscope. Instead of using the scanner to move the sample under the objective, as is traditionally done, this microscope moves the objective over the sample.

The scanner's customized placement makes this possible. Fig. 8 shows the scan pattern used by the software that controls the scanner. Directions sent to the scanner cause it to image a line (purple), then image the same line, backward (red), and then step up to the next line (pink) before repeating the process. Note that each of the line scans is composed of steps as small as those between lines, and that readings are taken after each step. After the scan, the scanning software takes the data from the forward lines and combines them to create a forward image, and does the same with the backward lines.

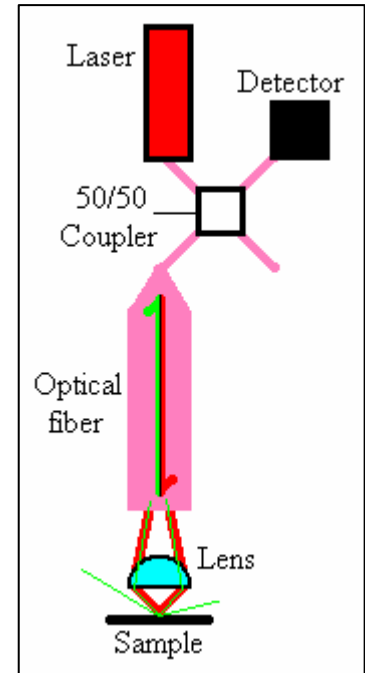


Figure 6: Diagram of the principle of confocal microscopy

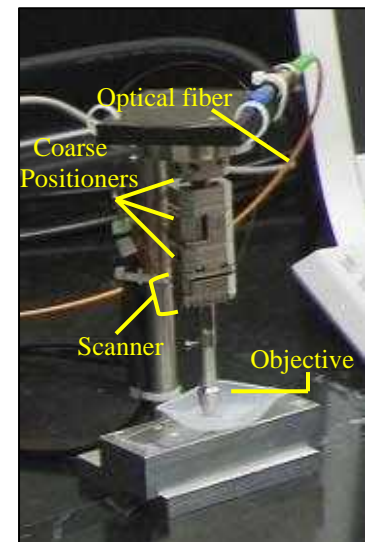


Figure 7: Photograph of the confocal microscope

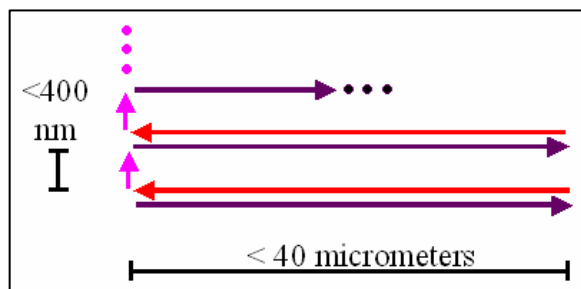


Figure 8: Diagram of the microscope's scan pattern

Basic operation of the microscope comprises 3 steps:

1. Using an oscilloscope, bring the microscope into the focal plane.

In addition to the scanner, the microscope stack contains three piezoelectric motors for coarse positioning of the objective (see Fig. 7). These motors move in the x, y, and z directions. To find the focal plane, the z motor brings the objective close to the sample (less than 2 mm away). Then, the laser is turned on. The detector sends the return signal to the computer as a voltage, which can be measured using an oscilloscope program. After this program is running, the z motor slowly takes the objective farther away. The voltage return shows a sharp peak at the focal plane, which is approximately 2.9 mm away from the objective.

2. Set the scanning parameters

Fig. 9 shows a screenshot of AttoScan, the program used to set the scanning parameters and take the image. AttoScan allows the user to change several parameters:

- Pixels (Side Length) (Range: 1 to 10,000)
- Maximum Voltage (Range: 0 to 4) ¹
- Scan Rate (measurements / s) (Range: 1 to 50,000) ²
- Average Rate (measurements / pixel)

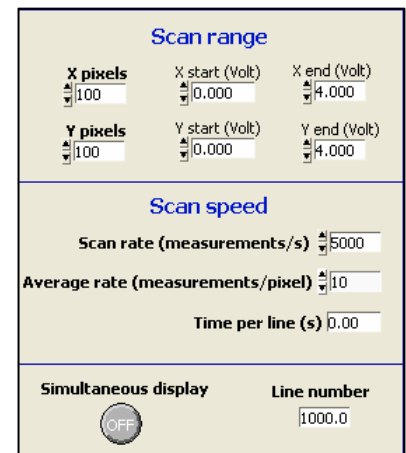


Figure 9: AttoScan screenshot

There is also an option to run the current traveling to the scanner through a low-pass filter with a cutoff frequency of 16, 160, or 1600 Hz.

¹ These voltages are amplified 15 times before delivery to the scanner, as are all other voltage values identified.

² The CFM manual was unclear. Within this project, the upper bound was considered to be 5,000.

3. Begin the scan

Multiple scans can now be taken without interruption.

3. Experimental Results:

The microscope was set up at room temperature for test scans and to identify appropriate scanning parameters. Images were initially taken to illustrate functionality, and to verify the specified scan size of approximately 40 micrometers. Fig. 11 shows images of a piece of copper which was polished with sandpaper, using perpendicular strokes. The diagonal lines, which probably did not result from mechanical effects or from noise, illustrate the functionality of the CFM. Fig. 10 is an image of a copper grid whose dimensions are known. The holes are ~30 micrometers across, while the bars are ~10 micrometers thick. This image verified the specified scan size of approximately 40 micrometers.

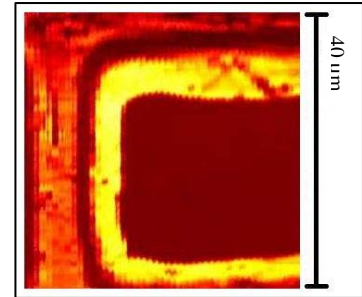
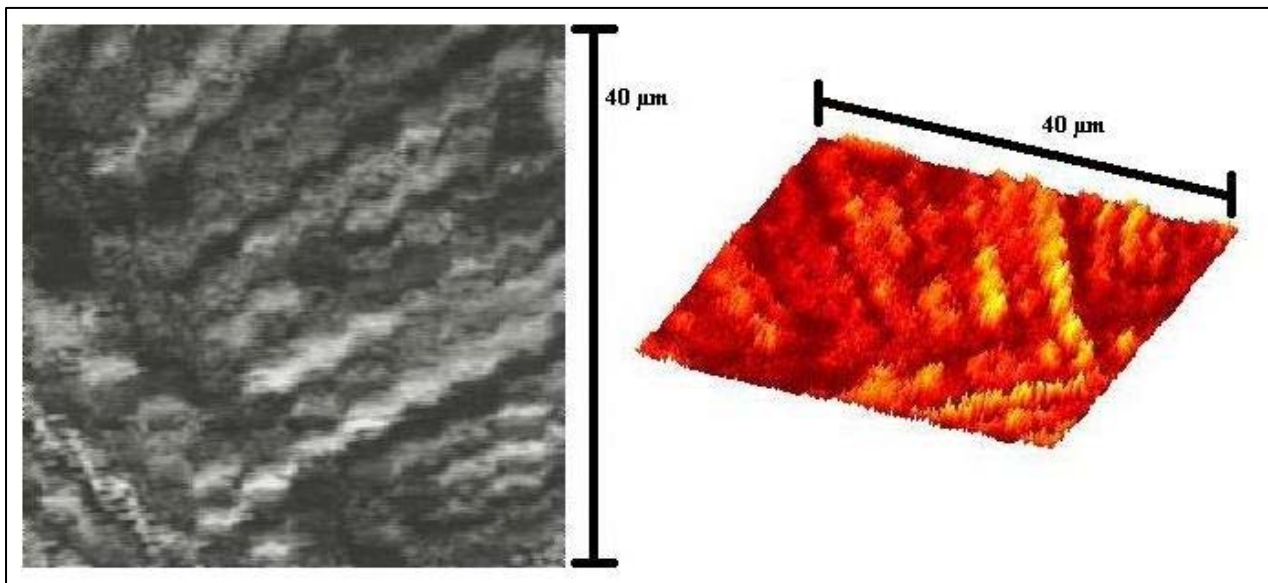


Figure 10: CFM image of a standardized copper grid

The diagonal lines, which probably did not result from mechanical effects or from noise, illustrate the functionality of the CFM. Fig. 10 is an image of a copper grid whose dimensions are known. The holes are ~30 micrometers across, while the bars are ~10 micrometers thick. This image verified the specified scan size of approximately 40 micrometers.

Figure 11: CFM image of a polished copper piece



In order to evaluate image quality, standardized scans of an atomic force microscopy (AFM) standard were taken. Fig. 12 illustrates the pattern on this standard and its dimensions. The pitch is 10 μm , and the depth of the pattern is 200 nm. Preliminary scans with this pattern showed several types of image degradation (arcs, “reflection,” and noise).

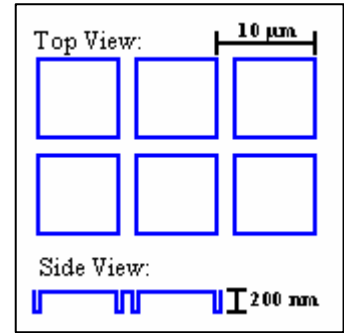


Figure 12: Dimensions of the AFM standard

In Fig. 13, arc-like distortions are observed, especially on the right side of the image. In Fig. 14, a “reflection” effect is observed on the left side of the image. In Fig. 15, three images were taken of a piece of plastic with small perturbations to show that the reflection is not a real feature. Between each scan, the objective was moved to the left over the sample. As the symmetrical feature in Fig. 15 moves toward the center of the scan area, it becomes evident that it is not actually symmetrical. The reflection effect most probably results from a time lag in the scanning software, which causes the software to add part of the backward image onto the forward image, and part of the forward image onto the backward image. Fig. 16 provides evidence of this explanation.

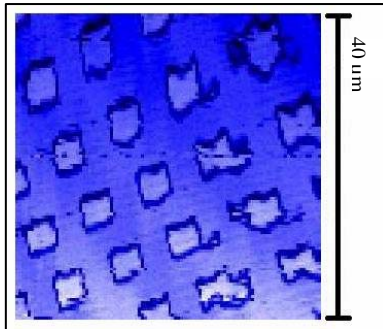


Figure 13: CFM image with arc-like distortions

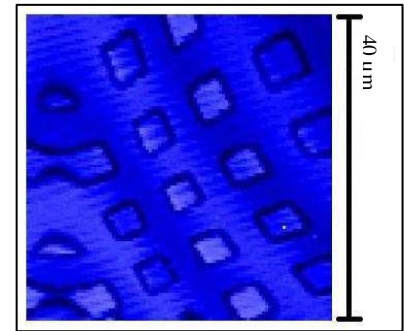


Figure 14: CFM image with the “reflection” effect

The final type of image degradation is observed in Fig. 17, which shows noise in the signal to the detector. Instability in the laser is believed to cause this effect. This belief is based on two facts: First,

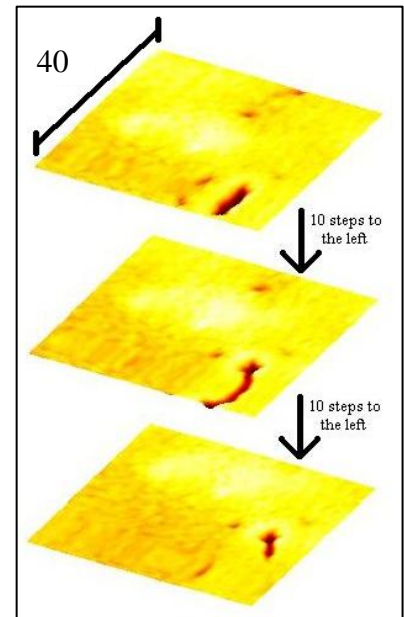


Figure 15: Multiple CFM scans showing that the symmetrical image is not a real feature

the noise in Fig. 17 stops approximately three quarters of the way through the scan, so the scanning parameters are not responsible for the effect; and Second, as Fig. 18 shows, wide and transient variation occurs in the return signal even when no adjustments are made. Nevertheless, there is a possibility that the noise is caused by uncontrolled vibrations.

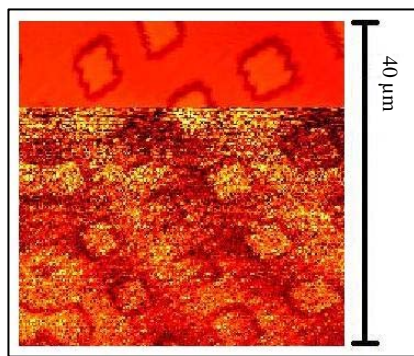


Figure 17: CFM image with noise that stops partway through the scan

The AFM standard shown in Fig. 12 was scanned many times to determine how different scan parameters affect the image.

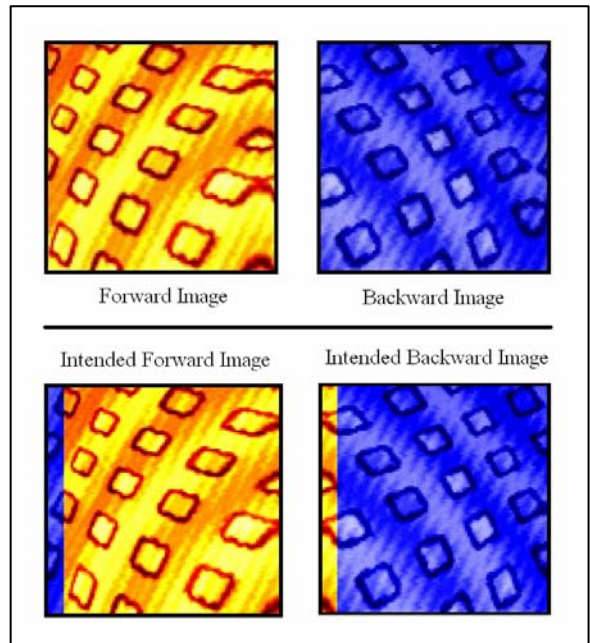


Figure 16: Actual and intended CFM images for forward and backward scans

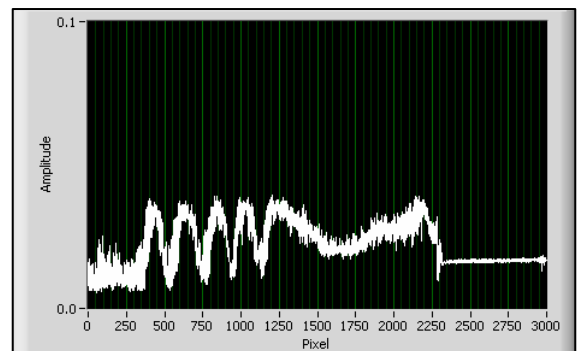


Figure 18: Variation in the CFM's return signal

a) Filter

(16, 160, or 1600 Hz)

Fig. 19 shows that lowering the frequency of the filter reduces the arc effect, while raising the frequency reduces the reflection effect.

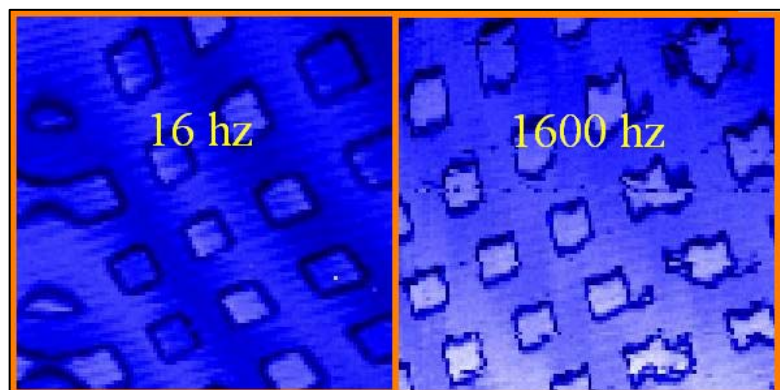


Figure 19: CFM images showing the result of changing the frequency of the filter

b) Pixels (Side Length)

(Range: 1 to 10,000)

Fig. 20 shows that increasing the number of pixels improves image quality by reducing reflection.

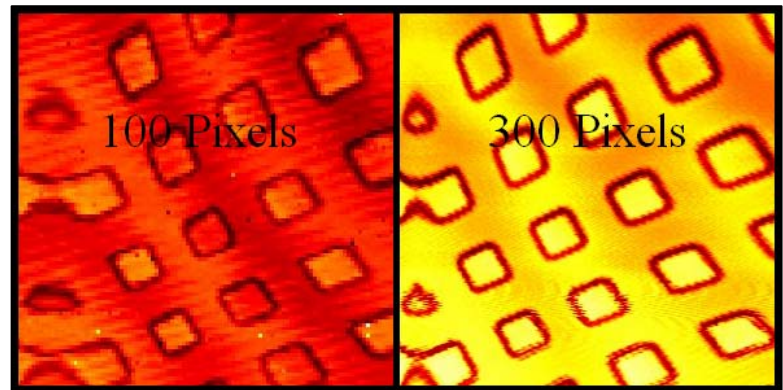


Figure 20: CFM images showing the result of changing the size of the image

c) Maximum Voltage

(Range: 0 to 4)

Fig. 21 shows that decreasing the voltage applied to the piezoelectric scanner decreases the actual dimensions of the scanned image.

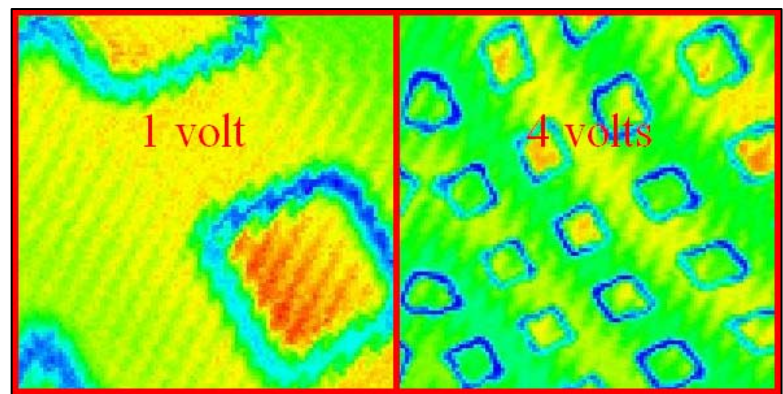


Figure 21: CFM images showing the result of changing the voltage applied to the piezoelectric scanner

d) Scan Rate (measurements / s)

(Range: 1 to 5,000)

Fig. 22 shows that increasing the scan rate increases reflection.

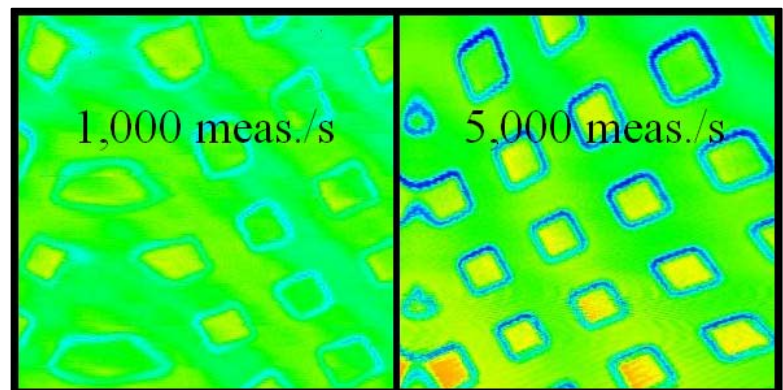


Figure 22: CFM images showing the result of changing the scan rate

e) Average Rate

(measurements / pixel)

Fig. 23 shows that increasing the average rate decreases the reflection effect.

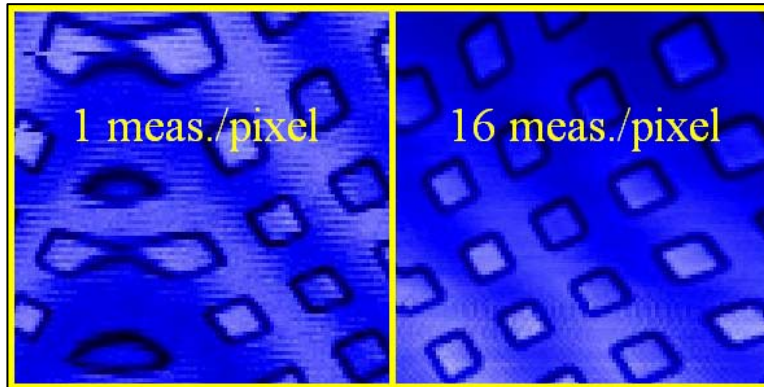


Figure 23: CFM images showing the result of changing the average rate

The time needed to scan an image is given by:

$$Time = (meas. \text{ per pixel}) * (pixels \text{ per side})^2 / (meas. \text{ per } s)$$

or, $Time = Average \text{ Rate} * Pixels^2 / Scan \text{ Rate}$

Since the microscope takes two images per scan (forward and backward), the time must be set to 20 seconds to optimize parameters for a 40-second scan. (The scanning software takes ~8 seconds to prepare before beginning the scan. This added time was ignored.) Based on earlier scans, 100 was determined to be the lowest value for Pixels that still preserved image quality. (Increasing Pixels above 100 increases scanning time quickly because time varies directly with the square of side length.) Under these conditions,

$$20 = Average \text{ Rate} * 100 * 100 / Scan \text{ Rate},$$

so $Average \text{ Rate} / Scan \text{ Rate} = 1 / 500.$

The images in Fig. 24 show that the best image results from the highest average rate, even though this increases the scan rate as well.

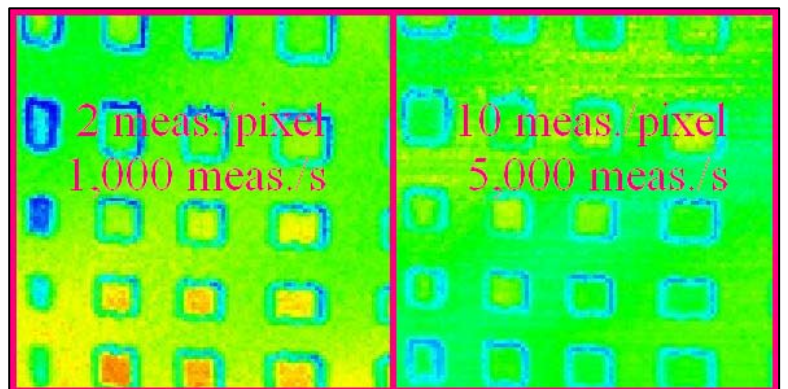


Figure 24: CFM images showing the result of simultaneously changing the scan rate and the average rate

4. Summary:

The effects of different parameters, evident in Figs. 17 through 24 and in other scanned images, are summarized in Fig. 25.

Figure 25: Summary of results

For	Set	<u>Pixels in the X Direction</u>	<u>Filter (Hz)</u>	<u>Measurements per Second</u>	<u>Measurements per Pixel</u>
Fewer Arcs		Higher	Lower	Lower	Higher
Less "Reflection"		Higher	Higher	Lower	Higher
Shorter Scan Time		Lower	~	Higher	Lower
40 Second Scan		100	16	5,000	10

It was also found that the voltage applied to the piezoelectric scanner, while affecting the scan size, has no noticeable effect on the image quality.

4. Conclusion:

The confocal microscope can demonstrably image a 40 by 40 micrometer area every 40 seconds. The optimal scanning parameters for this time goal are:

- Pixels (Side Length) = 100
- Maximum Voltage = 4
- Filter = 16 Hz
- Scan Rate = 5,000 measurements / s
- Average Rate = 10 measurements / s

The microscope is now ready to be incorporated into the cryogenic setup. The 40-second

scan parameters will be used in the experiment, and the heat flow will be adjusted to accommodate image size and resolution. However, many factors will change at cryogenic temperatures. At low temperatures, more voltage must be applied to the piezoelectric scanner for it to move the same distance, but higher voltages can be applied without causing damage (up to 10 V before amplification). Also, if the noise observed in Fig. 17 is due to vibration, it may disappear at cryogenic temperatures.

Two possibilities which should be explored in the future are the possibility of increasing the Scan Rate past 5,000 (and increasing the Average Rate proportionally) and of replacing the 16 Hz filter with the 1600 Hz filter combined with a computed low-pass filter. Both of these may result in better image quality.

5. Acknowledgements:

Dr. R. Stephen Craxton, without whose invitation I would not have had the opportunity to participate in this program.

Dr. David Harding, who helped me obtain samples to image and whose advice and encouragement improved the project and this report.

Ms Mariana Bobeica, who designed and built the cryogenic setup and who will carry out the planned experiment.

References

- [1] V.N. Goncharov, *Basic Principles of Direct Drive Ignition Target Design*, **LLE Review** Vol. 106, p. 83 (2006).
- [2] R.W. Petzoldt, *Direct Drive Target Survival During Injection in an Inertial Fusion Power Plant*, **Nuclear Fusion** Vol. 42, p. 1 (2002).
- [3] D. Harding, private communication (2007).
- [4] D.T. Goodin, et al., *Developing Target Injection and Tracking for Inertial Fusion Energy Power Plants*, **Nuclear Fusion** Vol. 41, p. 527 (2001).

Computational Modeling of Spectral Properties of Nickel Dithiolene Dyes

Rui Wang

Computational Modeling of Spectral Properties of Nickel Dithiolenes

Rui Wang

Fairport High School
Fairport, NY

Advisor: Kenneth Marshall

Laboratory for Laser Energetics
University of Rochester
Rochester, NY

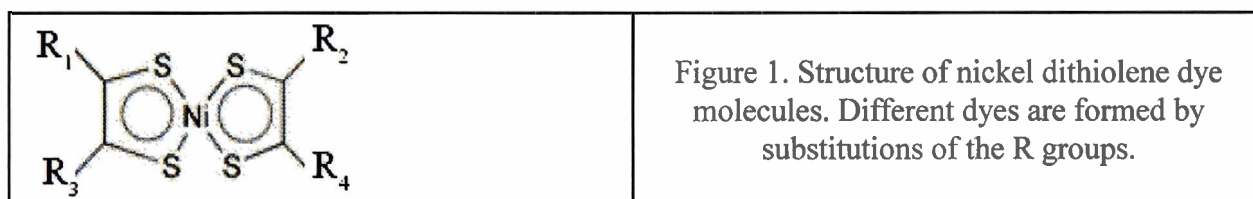
November 2006

Abstract

Nickel dithiolene dyes, noted for their intense long-wavelength electronic transitions, have been notoriously difficult molecules to model. This study has investigated the use of time-dependent density functional theory (TDDFT) to model these dyes. The absorption spectra of an extensive set of near-infrared nickel dithiolene dyes have been evaluated for the first time using TDDFT. Bulk solvent effects have also been accounted for. Excellent agreement between theoretical and experimental maximum absorption wavelengths has demonstrated the high accuracy of TDDFT. Successful prediction of the physical properties of proposed nickel dithiolene dyes leads to informed selection of candidates for future synthesis, significantly reducing the time and cost of materials development. Calculations for new nickel dithiolene dyes predict that the addition of sulfur atoms to the side chains will increase the maximum absorption wavelength by up to 160 nm. These results can aid in the further development of nickel dithiolene dyes in applications including near-infrared lasers, telecommunications, and sensor protection.

1. Introduction

Nickel dithiolenes were first synthesized in the 1960s and were noted for their intense absorption over a broad range of near-infrared (IR) wavelengths. These organometallic dyes contain a zerovalent planar core with dithiolene rings surrounding a nickel atom (Figure 1).



Nickel dithiolene dyes have characteristics that can be useful in an array of applications. Their intense long wavelength absorption is a result of the low-energy π - π^* transition between

the highest occupied molecular orbital (HOMO) and the lowest unoccupied molecular orbital (LUMO)¹. In addition, this class of dyes exhibits an auxochromic shift (shift in absorption spectra) depending on the R groups attached². This property makes nickel dithiolenes useful as near-IR dyes for optical applications. The zerovalent nature of the dithiolene core imparts relatively high solubility in nonpolar solvents, including liquid crystal hosts, and makes these dyes useful for near-IR liquid crystal device applications³. Some metal dithiolenes have an inherent liquid crystal phase⁴ and thus can be dissolved in a liquid crystal host in relatively large quantities without changing the characteristics of the host fluid.

Transition-metal dithiolenes are of interest for many applications. First, the inherent solubility and stability of these materials lead to their use in photodetectors⁵, which are used by the fiber-optic telecommunications market as components that detect laser light in fiber-optic systems and transform that light into electrical current. The primary wavelengths of interest for this application are 1300 nm and 1550 nm. They can be used for both long-haul transport and telecommunications receiver systems carrying high-speed voice and data/Internet traffic⁵. Second, nickel dithiolene dyes are used in Q-switching saturable absorbers to produce short intense pulses for IR lasers because of their high thermal and optical stability.² A dye with an absorption maximum near the laser wavelength will absorb the laser radiation and the electrons of the dye molecules will be boosted into the excited state as the energy level in the lasing medium increases. When the dye is optically “saturated” (most of the dye molecules are in the excited state) the dye no longer absorbs the laser radiation and a short, intense laser pulse is released. These lasers generally operate at wavelengths between 950 and 1100 nm. Third, because nickel dithiolenes absorb in the near-IR range, they are of interest for IR sensor protection for the military. For this application, the electronic absorption band is tunable from

around 600 nm to 1600 nm by changing either the dye structure (through synthesis), or the helical pitch length of the dye (if it is chiral).³ The Air Force is currently investigating the application of transition metal dithiolenes absorbing in the 700-900 nm region as part of a liquid crystal electro-optical device for night vision and avionics applications.³

The synthesis of nickel dithiolenes is a multi-step, low-yield process and is thus costly and time-consuming. Conventional trial-and-error synthesis approaches result in the need to synthesize a large number of compounds to establish physical properties trends. As has been previously demonstrated in the pharmaceutical industry, computational chemistry can be used to predict the most promising materials for synthesis, thus resulting in substantial savings in time, resources, and cost.

Although computational methods are well established for organic compounds, very little work has been done in modeling the electron interactions in transition metal organometallic molecules. The most recent attempt at computing the structures and properties of nickel dithiolene dyes was performed by C. Lauterbach and J. Fabian.⁶ Because of computational limitations and data availability, only a few nickel dithiolene molecules were modeled using an older method known as single configuration interaction (CIS).⁷ More recently, D. Jacquemin et al.^{8, 9, 10} predicted the optical properties of other classes of organic dyes such as indigo and nitro-diphenylamine derivatives using a newer method known as time dependent density functional theory (TDDFT)¹¹. Their methodology produced relatively high computational accuracy for absorption spectra calculations. Thus, TDDFT seems a promising solution to the computational difficulties of nickel dithiolenes, which are also optical dyes.

In this study, the computational approach of TDDFT has been applied for the first time to predict the absorption spectra of nickel dithiolene systems. The maximum absorption

wavelengths have been accurately predicted for a large number of nickel dithiolene dyes and four new dyes have been proposed that extend the maximum absorption wavelength further into the IR. This improved computational method can lead to advances not only in near-IR devices, but also in applications of optical dyes across the electromagnetic spectrum.

2. Previous Research

There are three common methods for excited state computation: (1) semiempirical and Zerner's Intermediate Neglect of Differential Overlap (ZINDO);¹² (2) Hartree-Fock and single configuration interaction (CIS);⁷ and (3) density functional theory (DFT) and time-dependent density functional theory (TDDFT).¹¹

The first calculations of nickel dithiolene properties used the early semiempirical quantum chemical models.^{13, 14} These models save computational time by using experimental data to fit the calculation according to known parameters. Using approximations, this method decreases the computational time but at the cost of accuracy. ZINDO is one type of semiempirical algorithm for studying excited state and spectroscopic properties of molecules. This method is limited in accuracy, as all semiempirical models are, by the degree of similarity between the molecule being studied and known molecules from which parameters are taken.

In the Hartree-Fock method, all nuclei are assumed motionless with respect to the electrons, electron orbitals are expressed as one-electron functions centered on each atom, and the multi-electron calculation of the model is assumed to be given by the sum of all single-electron calculations of the molecule.¹⁵ Relativistic effects and electron correlation effects (electron-electron interactions) are mostly neglected. The Hartree-Fock method becomes decreasingly accurate with increasing molecular size.¹⁵ This method is used for approximating the ground state energy of a molecular system. Post-Hartree-Fock methods have been developed

to improve on the Hartree-Fock method by approximating the electron correlation of a system.¹⁶ This gives more accurate results but at a greater computational cost. The single configuration interaction (CIS) is one example of a post-Hartree-Fock method limited to single excitations. This method is expanded from the Hartree-Fock calculations to incorporate electronic excitation and changing shell levels. However, known results using this method indicate that its accuracy is not high for larger molecules.^{15, 17}

Previous work done on modeling nickel dithiolene dyes by Lauterbach and Fabian utilized the CIS method for excited-state absorption spectra calculations.⁶ Their study calculated the structure, electron distribution, electron bonding, and spectral properties of transition-metal molecules including nickel dithiolenes. Other transition metal compounds investigated included metal diiminolenes, dioxylenes, and diselenolenes utilizing nickel, palladium, and platinum as the central metal. Lauterbach and Fabian performed all calculations in the gas phase and thus omitted all effects associated with the solvents that host the dyes during experimental measurements of the absorption spectrum. Their analysis of the structure focused mostly on the effect of substitutions for the nickel and sulfur atoms in Figure 1.

More recently, density functional theory has emerged as a useful computational method for ground state properties. Unlike the Hartree-Fock method, DFT uses the electron density as the foundation of its calculations instead of the many-electron wavefunction.¹⁶ The main advantage is that the wavefunction, a complex function in multi-dimensional space that takes into account individual electrons, is replaced by a density function in three spatial dimensions, which greatly lowers the computational cost. DFT has been extended to time-dependent density functional theory (TDDFT), which models the evolution of the system in time in response to an external disturbance, as described below. Jacquemin used TDDFT extensively to model the absorption

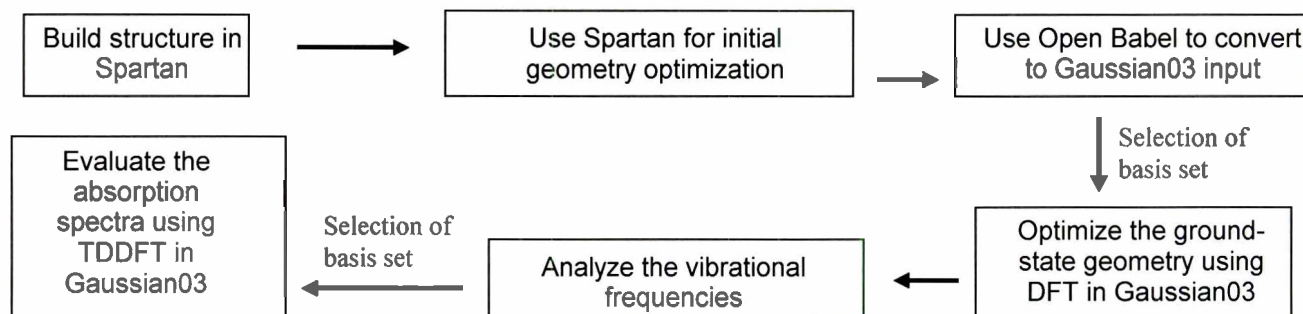
spectra of other optical dyes including indigo and anthraquinones-based dyes,^{8, 9, 10} and consistently demonstrated the high accuracy of TDDFT for these dyes. DFT and TDDFT were selected for this study for their improved accuracy over other methods and comparable computational cost.

3. Methodology

This study used the Gaussian03 program¹⁸ by Gaussian Inc. to carry out the quantum chemical calculations using DFT and TDDFT. Gaussian03 predicts the energies, molecular structures, vibrational frequencies, and excited-state transitions of molecular systems along with other physical properties derived from these calculations.¹⁸

The methodology shown in Figure 2 was developed for this study. First, the atoms, bonds,

Figure 2. An overview of the methodology developed.



and arrangement of each molecule are entered into a molecular modeling program, Spartan (Wavefunction Inc.), which is used to roughly approximate the initial geometry and output the Cartesian coordinates of each atom.¹⁹ Spartan checks the bond lengths and angles with known molecules but does not optimize the geometry using energy minimization. Using OpenBabel, the coordinates are converted into a format that can be read by Gaussian03, which rigorously optimizes the ground state geometry through energy minimization, using DFT and a carefully selected basis set. Figure 3 shows the electron density map of the nickel dithiolene core in the

ground state calculated by Gaussian03.

Basis sets play an important role in these calculations. The electron density function of the given molecule is calculated using a linear combination of spatially dependent elementary functions contained in the basis sets. The potential function is calculated as the sum of the external potential (interactions with ions), the Hartree potential (classical electron-electron interactions), and the “exchange-correlation” potential (complex many-body effects that have to be approximated).²⁰ The basic concept of DFT is to vary the coefficients in the basis functions

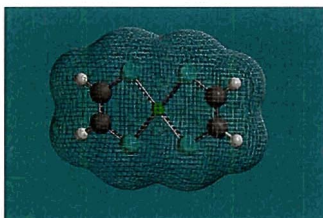


Figure 3. The ground-state electron density of the nickel dithiolene core (R=H).

and the coordinates of all the ions until a

stationary point with minimum energy is

found. The geometry at the point of the

energy minimum is given as the optimized

geometry. The choice of basis sets is important because enough functions are needed to give sufficient accuracy, yet too many or inappropriate functions may cause convergence problems that result in the program failing to find the lowest-energy minimum.

The vibrational spectrum is then analyzed to check the computed geometry, since the accuracy of the absorption spectra depends on the accuracy of the structure. The substantial computational time for the larger molecules leads to the omission of this step unless an anomaly in the absorption maximum warrants investigation of the vibrational frequencies.

Finally, the transition energy to the excited state is calculated using TDDFT. TDDFT disturbs the ground state density calculated by DFT by applying an impulse potential. This impulse potential contains all frequencies so that the frequency-dependent time evolution of the electron density allows the absorption spectrum and the wavelength of maximum absorption to be calculated.²⁰

Since all reported experimental maximum absorption wavelengths of nickel dithiolene dyes were measured in solution, solvent effects are taken into account for both DFT and TDDFT calculations. The potential function is adjusted for the presence of solvents using the polarizable continuum model (PCM).²¹ The PCM divides the calculation into a solute part (the nickel dithiolene molecule) and a solvent part (the surrounding solvent molecules), which is characterized by its dielectric constant, radius and other macro-scale properties.

4. Optimization Of Basis Sets

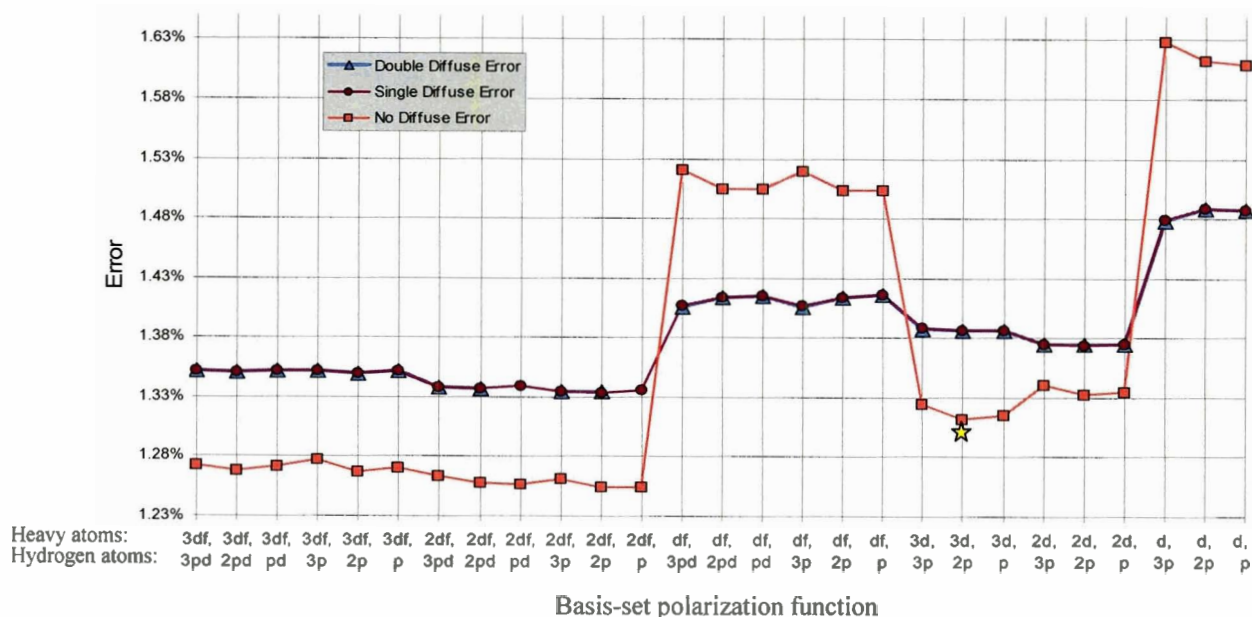
4.1 Basis Sets For Energy Minimization

To evaluate the density function using Gaussian03, the exchange-correlation portion of the potential function was approximated using the hybrid functional PBE1PBE (25% electron-exchange and 75% electron-correlation).²² This was done for both DFT and TDDFT calculations.

It was important to choose an appropriate basis set. A large number of basis sets are commonly used, which are clarified with standard notation. For instance, in 6-311++G(d, p), '6-311' indicates 11 functions (6+3+1+1) for the s-orbital and 5 functions (3+1+1) for the p-orbital in large atoms, and 5 functions (3+1+1) for the s-orbital in hydrogen, while G denotes this as a Gaussian basis set. The notation '++' indicates the addition of "double diffuse" functions (designed to model more accurately electrons farther from the nucleus of an atom) for all atoms; single diffuse, '+', treats only nonhydrogen atoms. The notation '(d, p)' indicates the addition of "polarization" functions (describing more orbitals, in this case one function for the d-orbital in larger atoms and one function for the p-orbital in hydrogen).²³ Eighty-one Gaussian basis sets, with combinations of polarization and diffuse functions supplementing the basic 6-311G set, were systematically analyzed with the nickel dithiolene core (R = H in Figure 1). The polarization functions, which aid in the modeling of bonding interactions, ranged from (d, p) to

(3df, 3pd). Each polarization function variation was evaluated with double diffuse, single diffuse, and no diffuse functions. The core structure was chosen for this study because it is the part of the overall nickel dithiolene molecule that affects the absorption spectra the most.²⁴ Because no extensive R groups are attached, the computational time was relatively short (~30 minutes). If a basis set failed to converge on the nickel dithiolene core, it was avoided for calculations of structures with R groups attached. This problem was sometimes encountered for relatively large basis sets. For each optimized geometry derived from a specific basis set, measurements were taken and compared with experimental values²⁵ for the bond lengths of Ni-S, S-C, and C-C, and for the bond angles of S-Ni-S, Ni-S-C, and S-C-C of the nickel core. The error is reported in Figure 4 as a percentage error averaged over all measurements for each basis set. The errors for all basis sets are graphed with groups of double, single, and no diffuse functions. Larger basis sets generally require greater computational time because more polarization functions are used. The results in Figure 4 are arranged from the most extended to the least extended basis sets so that the trade-off between accuracy and computational time can be assessed. Because the

Figure 4. Mean absolute error of selected bond lengths and angles using various basis sets, which are labeled by polarization and diffuse functions. (Double and single diffuse errors overlap.) The star indicates the chosen basis set.



difference in accuracy between double and single diffuse functions is minimal, it was determined that adding double diffuse functions is not necessary. The underlying assumption for this choice was that hydrogen does not play a significant role in the modeling of these compounds. The line graphs for the basis sets with diffuse functions follow a general trend upward in percent error as smaller basis sets are used. In Figure 4, the polarization functions for the heavy atoms seem to affect the error more than the polarization functions for hydrogen atoms. This observation is also true for basis sets without diffuse functions, though more fluctuation occurs.

Recognizing that even with the fluctuations shown on the graph, the difference between the highest point and the lowest point on the entire graph is only an error of 0.38%, the goal was to find the least time-consuming basis set with a reasonably small error. The focus is on the right side of the graph with relatively small basis sets since convergence problems sometimes arise with the larger basis sets and the addition of more polarization functions does not seem to produce better results. Therefore, the basis set 6-311G(3d, 2p) (star on the graph) was chosen for the geometry optimization since it produced a local minimum in error for a reasonable computational time. In the previous study by Lauterbach and Fabian,⁶ though the list of molecules investigated was more extensive than in previous studies, the experimental absorption maximum value cited was for the nickel dithiolene with H as each of the four R groups. This compound thus provides the only useful error comparison between this study and theirs. Table 1 compares the structural data from this study and data obtained by Lauterbach and Fabian along with the experimental data. The average error obtained by Lauterbach and Fabian, 1.77%, is higher than the 1.31% error obtained here.

Table 1. Comparison between theoretical and experimental bond lengths [\AA] and angles [$^\circ$]			
Bond lengths:	Experimental ^[a]	This work ^[b]	Lauterbach and Fabian ^[c]
Ni(1)-S(1)	2.100	2.123	2.178
S(1)-C(1)	1.687	1.685	1.705
C(1)-C(2)	1.353	1.372	1.374
Bond angles:			
S(1)-Ni(1)-S(2)	88.5	92.5	92.1
Ni(1)-S(1)-C(1)	107.8	103.5	102.9
S(2)-C(2)-C(1)	117.9	120.2	121.1
Average % Error		1.31%	1.77%
[a] Ref. 25 — [b] Calculated using 6-311G(3d, 2p) — [c] Ref. 6 Calculated using 6-311+G*			

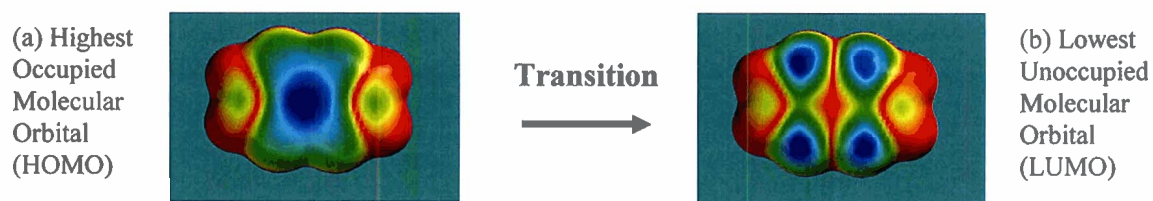
The choice of basis set in these calculations was verified by computing the vibrational frequencies using the chosen basis set, 6-311G(3d, 2p). Using DFT, Gaussian03 computes force constants and the resulting vibrational frequencies of the molecule, along with the intensities at those frequencies.¹⁸ The major frequencies, (799 cm^{-1} and 1132 cm^{-1} for C=S bonds; 1399 cm^{-1} for the C=C bond; and around 3175 cm^{-1} for C-H bonds) all agreed with experimental data,²⁶ confirming the accuracy of both the molecular structure and the computed absorption spectra.

When the procedure developed for the nickel dithiolene core was applied to larger nickel dithiolene dye molecules using DFT, the basis set 6-311G(3d, 2p) was found to produce convergence errors and the computational time increased dramatically. The basis sets may have been too restricting, and often no stationary energy minimum could be found within computational limits. Several smaller basis sets were then tested, and 6-311G(d, p) was found to satisfactorily produce the geometry optimization.

4.2 Basis Sets For Time-Dependent Absorption Wavelength Calculations

The next step is the excited state, time-dependent calculations. Figure 5 shows the electron density shift in the nickel dithiolene core when the molecule transitions from the ground state (HOMO) to the excited state (LUMO). The blue area indicates the most electron-rich region, while the red area indicates the electron-deficient region. The electron density shifts from

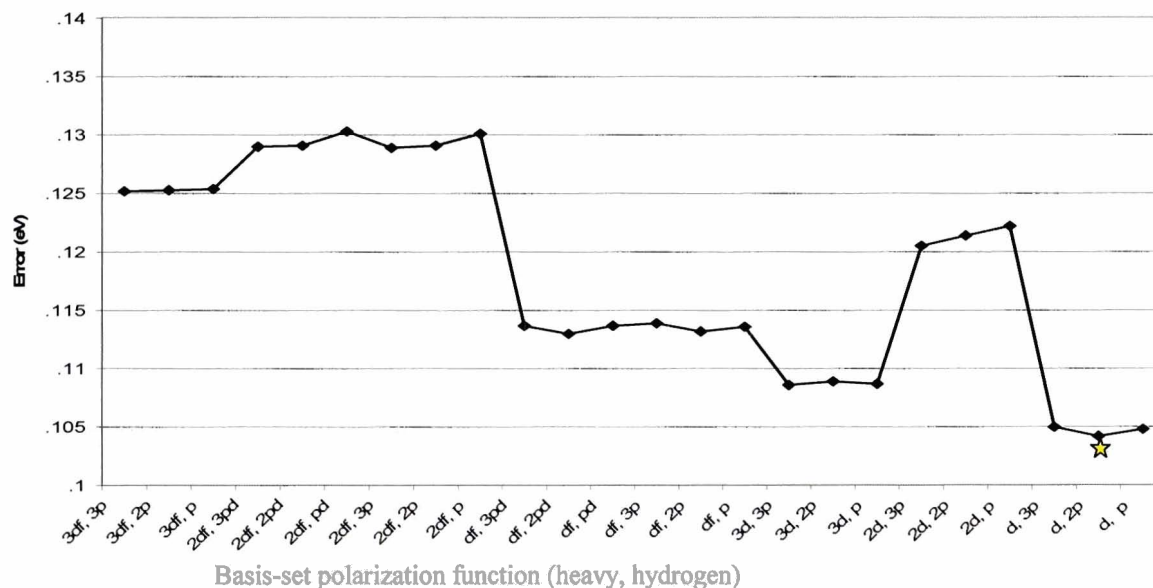
Figure 5. Electron density maps of the electronic transition modeled by TDDFT for the nickel core (Figure 1). Blue indicates high electron density.



the center of the molecule to the four sulfur ligands during this energy transition.

A new basis set was needed, as the TDDFT calculations differ from the geometry calculations. First, TDDFT calculations were performed using basis sets without diffuse functions, but the errors in the resulting absorption spectra were not acceptable and the focus turned to basis sets with single-diffuse functions. Therefore, a systematic test was run in which all the single-diffuse basis sets were used to calculate the absorption spectra of the core, holding the optimized structure constant (Figure 6). The graph again demonstrates that the polarization functions for heavy atoms are more important in determining the errors in the calculation. From the global minimum of this graph, the 6-311+G(d, 2p) basis set was chosen for the TDDFT calculations of all the remaining nickel dithiolene dyes under investigation.

Figure 6. Error in the absorption-maximum photon energy of the nickel dithiolene core using different single diffuse (+) basis sets for the excited state calculations. The ground-state geometry was optimized using the 6-311G(3d, 2p) basis set.



5. Determination of Maximum Absorption Wavelengths

The main purpose of this study was to investigate the accuracy of TDDFT in predicting the maximum absorption wavelengths λ_{\max} of various nickel dithiolene dyes. The computed λ_{\max} for all investigated nickel dithiolene dyes are reported in Table 2 along with experimental data. The graph in Figure 7(a) provides a comparison of the theoretical λ_{\max} with experimental results. The electron energy transition responsible for producing these maximum absorption wavelengths was between the ground state and the first excited state (see Figure 5), which confirms both experimental and previous computational findings.^{25, 27} Only systems with solvents that are parameterized in Gaussian03 were selected so that a fair comparison could be performed. The computational time for each molecule on eight processors running on a 1.6 GHz Itanium II SGI Altix supercomputer ranged from hours to days, depending on the complexity of the structure and the properties of the solvent.

As a measure of accuracy, the maximum absorption wavelength calculated for the nickel dithiolene core in this study was compared with that of a previous study.⁶ The absorption wavelength is 678.92 nm, an error of 0.10 eV (all errors are compared in eV for consistency and convention) from the experimental value of 720 nm.² This result is a substantial improvement from the previous result of 623 nm determined with the CIS method⁶ (an error of 0.27 eV).

Since TDDFT is to be used as a predictive tool for determining the maximum absorption wavelength of optical dyes, the data collected in this study was statistically treated to provide a more direct prediction of experimental values. It is clear from Figure 7(a) that the raw wavelengths calculated here consistently underestimate the experimental values. Such data are usually subjected to statistical treatment¹⁰ using simple linear regression. The data plotted in Figure 7(a) were fit with the equation: $\lambda_{\max, \text{exp.}} = 64.84 + 1.0021 \lambda_{\max, \text{raw theory}}$, with a Pearson

R-Groups		Solvent	Theory (raw) λ_{\max} (nm)	Theory (treated) λ_{\max} (nm)	Experiment λ_{\max} (nm)	Ref.
R1, R4	R2, R3					
H	H	Hexane	678.9*	745.7*	720	2
Methyl	Methyl	Chloroform	704.3	771.2	774	2
Methyl	Methyl	Dichloromethane	702.7	769.6	770	28
Butylthio	Butylthio	Acetone	893.4	961.0	1002	4
Butylthio	Butylthio	Chloroform	900.7	968.3	1004	2
Phenyl	Phenyl	Chloroform	809.9	877.2	866	2
2-Naphthyl	2-Naphthyl	Chloroform	852.2	919.7	905	2
H	Phenyl	Dichloromethane	774.8	841.9	810	28
Ethyl	Ethyl	Dichloromethane	680.2	747.0	770	28
Phenyl	Methyl	Dichloromethane	731.7	798.7	795	28
Phenyl	Ethyl	Dichloromethane	719.0	786.0	795	28
Phenyl	Phenyl	Dichloromethane	811.9	878.4	865	28
4-octylphenyl	H	Dichloromethane	776.3	843.5	865	28
4-octylphenyl	H	Hexane	764.8	832.0	850	2
4-bromophenyl	4-bromophenyl	Dichloromethane	830.9	898.2	870	28
4-methylphenyl	4-methylphenyl	Dichloromethane	854.1	921.6	900	28
Pentylthio	Pentylthio	Acetone	905.2	972.9	1002	4
2-thienyl	2-thienyl	Chloroform	957.4	1025.3	982	2

*This geometry was calculated using 6-311G(3d, 2p). The geometry for all other structures was calculated using 6-311G(d,p).

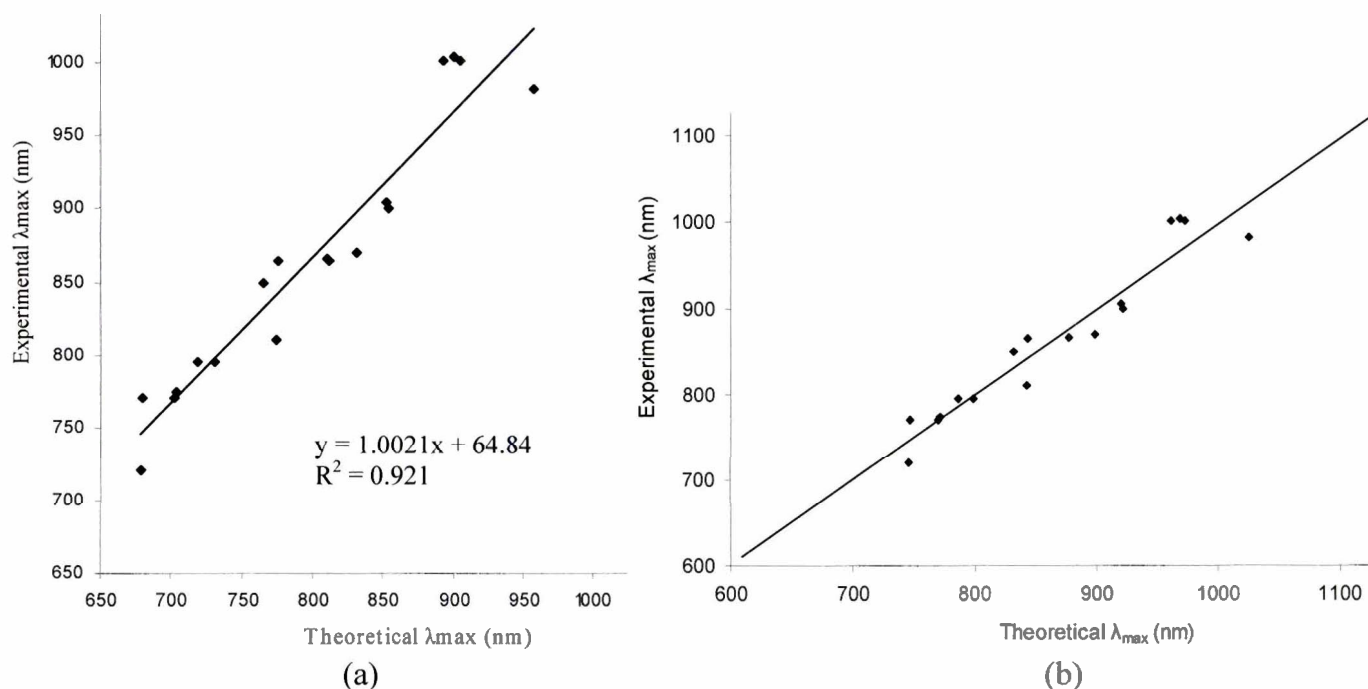


Figure 7.

(a) Comparison between the raw theoretical λ_{\max} and the experimental λ_{\max} . The line shows linear regression.

(b) Comparison between the statistically treated theoretical λ_{\max} and the experimental λ_{\max} . The line indicates $\lambda_{\max, \text{theory}} = \lambda_{\max, \text{exp}}$.

correlation coefficient R^2 of 0.921. All the raw values were then adjusted using this equation, giving the treated theoretical wavelengths of Figure 7(b), which can then be used to improve the theoretical predictions.

These predictions of the maximum absorption wavelength of the nickel dithiolene core are the most accurate to date. For the entire group of nickel dithiolene dyes investigated, the mean unsigned error is 0.033 eV. This translates to an absolute difference of 20.8 nm between experimental values and treated theoretical values on average. These errors are much smaller than previously reported errors; even studies using TDDFT typically report errors ranging from 0.2 to 0.4 eV for transition-metal molecules.^{29, 30}

The trends among various nickel dithiolene dyes are correctly modeled. The structures with terminal groups containing sulfur or phenyl rings are found to have longer-wavelength absorption maxima. The solvatochromatic effects (solvent effects on the λ_{max}) are also reasonably predicted. For the structure $R_1R_4 = 4\text{-octylphenyl}$ and $R_2R_3 = \text{H}$, the experimental values show a hypsochromic shift (blue shift) of 15 nm, when the solvent changes from dichloromethane to hexane, while the theoretical values give a shift of 11.5 nm. Similarly, the solvatochromatic effects on the nickel dithiolene dye with $R = \text{methyl}$ and the dye with $R = \text{butylthio}$ are modeled accurately. These further demonstrate the validity of TDDFT for the quantitative evaluation of the maximum absorption wavelength of various nickel dithiolene dyes.

With the accuracy of the methodology validated, several new nickel dithiolene dyes were designed and modeled using DFT and TDDFT in an attempt to extend the measured absorption wavelength into the IR. Since sulfur seems to effect a bathochromic shift (red shift) when included as part of the R groups, and sulfur-containing structures have traditionally been more soluble than phenyl-containing structures³¹ (which also effect a bathochromic shift), the new

dyes were designed with sulfur added to the R groups. The results shown in Table 3 confirm this hypothesis in each of three groups, with significant red shifts in the maximum absorption wavelength of up to 160 nm. It is anticipated that this work will allow more nickel dithiolene dyes to be synthesized with maximum absorption wavelengths further into the infrared region.

R ₁ R ₄	R ₂ R ₃	Solvent	Predicted λ_{\max} (nm)	Exp. λ_{\max} (nm)
4-phenyl-Br	4-phenyl-Br	DiChloroMethane	895.2	870
SBr	SBr	DiChloroMethane	975.2	-
SF	SF	DiChloroMethane	971.6	-
Methyl	Methyl	Chloroform	772.0	774
S-methyl	S-methyl	Acetone	845.8	-
H	H	Hexane	745.7	720
SH	SH	Hexane	907.5	-

6. Discussion/Conclusions

The absorption spectra of an extensive set of nickel dithiolene dyes have been studied using TDDFT to compute excited state energies, with bulk solvent effects taken into account. A hybrid functional and two basis set combinations, 6-311G(d, p) for the ground state geometry and 6-311+G(d, 2p) for the excited state energies, were used in this study. Close agreement between the theoretical and experimental λ_{\max} has been achieved for 18 known dyes, with a mean absolute error limited to 0.033 eV. A methodology has been used for nickel dithiolene dyes that can be adapted to future studies of these and other optical dyes.

This study provides a significant step forward in advancing the science of computational chemistry in organometallics, especially shown by the low error in this study as compared with those currently reported in the literature. Four new nickel dithiolene molecules have been designed and modeled, with findings that indicate that adding sulfur to the R groups will increase the λ_{\max} by up to 160 nm. Future work will seek to extend the λ_{\max} further into the infrared region, by making additional modifications to the terminal R groups. The success of this method

will greatly assist the development and synthesis of new transition metal dithiolenes and will aid in the use of nickel dithiolenes as near-IR dyes in applications such as telecommunications, sensor protection, and liquid crystal devices in laser systems.

Acknowledgements

I would like to thank my advisor Mr. Kenneth Marshall for his guidance and support in my research, as well as Dr. R Stephen Craxton for not only providing the opportunity to work at the University of Rochester's Laboratory for Laser Energetics but also helping me during the final stage of my project. In addition, I would like to thank Anthony Noto for mentoring me on the applications and limitations of the Gaussian03 program.

References

1. Mueller-Westerhoff, U. T.; Vance, B. Dithiolenes and Related Species. In *Comprehensive Coordination Chemistry*; Wilkinson, G., Gillard, R. D., McCleverty, J. A., Eds.; Pergamon: Oxford, 1987; Vol. 2, pp 595-631.
2. Mueller-Westerhoff, U. T.; Vance, B.; Yoon, D. I. *Tetrahedron* 1991, *47*, 909-932.
3. Marshall, K. L.; Schudel, B.; Lipka, I. A. *Proc. SPIE* 2003, *5213*, 201-212.
4. Marshall, K. L.; Klehn, B.; Watson, B.; Griffin, D. W. *Proc. SPIE* 2003, *5188*, 48-60.
5. Caironi, M.; Natali, D.; Sampietro, M.; Ward, M.; Meacham, A. P.; Devillanova, F. A.; Arca, M.; Denotti, C. *Proc. SPIE* 2004, *5464*, 165-175.
6. Lauterbach, C.; Fabian, J. *Eur. J. Inorg. Chem.* 1999, *11*, 1995-2004.
7. Stanton, J. F.; Gauss, J.; Ishikawa, N.; Head-Gordon, M. *J. Chem. Phys.* 1995, *103*, 4160-4174.
8. Jacquemin, D.; Preat, J.; Wathélet, V.; Perpète, E. A. *J. Chem. Phys.* 2006, *124*, 074104.
9. Jacquemin, D.; Preat, J.; Charlot, M.; Wathélet, V.; André, J.; Perpète, E. A. *J. Chem. Phys.* 2004, *121*(4), 1736-1743.

10. Perpète, E. A.; Wathélet, V.; Preat, J.; Lambert, C.; Jacquemin, D. *J. Chem. Theory Comput.* 2006, 2, 434-440.
11. Runge, E.; Gross, E. K. U. *Phys. Rev. Lett.* 1984, 52, 997-1000.
12. M.C. Zerner, ZINDO, A Semiempirical Quantum Chemistry Program, Quantum Theory Project, University of Florida, Gainesville, FL, 1996.
13. Schrauzer, G. N.; Mayweg, V. P. *J. Am. Chem. Soc.* 1965, 87, 3585-3592.
14. Schrauzer, G. N. *Acc. Chem. Res.* 1969, 2, 72-80.
15. Corsello, S. *Student Research Reports, 1998 Summer Research Program for High School Juniors at the University of Rochester's Laboratory for Laser Energetics*, 1998.
16. Hehre, W. J. *Ab Initio Molecular Orbital Theory* 1986 (Wiley, New York).
17. Jacquemin, D., private communication, 2006.
18. Frisch, M.J. et al., Gaussian03, Gaussian, Inc., Pittsburgh, PA, 2004.
19. SPARTAN '04, Wavefunction, Inc., 18401 Von Karman Ave., #370, Irvine, CA 92715, 2003.
20. Marques, M. A. L.; Gross, E. K. U. *Annu. Rev. Phys. Chem.* 2004, 55, 427-455.
21. Amovilli, C.; Barone, V.; Cammi, R.; Cancès, E.; Cossi, M.; Mennucci, B.; Pomelli, C. S.; Tomasi, J. *Adv. Quantum Chem.* 1998, 32, 227.
22. J. P. Perdew, K. Burke, and M. Ernzerhof, *Phys. Rev. Lett.* 1996, 77, 3865.
23. Ahlrichs, R.; Taylor, P. R. *J. Chem. Phys.* 1981, 78, 315-324.
24. Eisenberg, R. *Prog. Inorg. Chem.* 1970, 12, 295-369.
25. Herman, Z. S.; Kirchner, R. F.; Loew, G. H.; Mueller-Westerhoff, U. T.; Nazzari, A.; Zerner, M. *Inorg. Chem.* 1982, 21, 46-56.
26. Schlapfer, C. W.; Nakamoto, K. *Inorg. Chem.* 1975, 14, 1338-1344.
27. Hill, C. A. S.; Charlton, A.; Underhill, A. E.; Malik, K. M. A.; Hursthouse, M. B.; Karaulov, A. I.; Oliver, S. N.; Kershaw, S. V. *J. Chem. Soc. Dalton Trans.* 1995, 4, 587-594.
28. Winter, C. S.; Oliver, S. N.; Manning, R. J.; Rush, J. D.; Hill, C. A. S.; Underhill, A. E. *J. Mater. Chem.* 1992, 2, 443-447.

29. Petit, L.; Makdivi, P.; Adamo, C. *J. Chem. Theory Comput.* 2005, *1*, 953-962.
30. Adamo, C.; Barone, V. *Theor. Chem. Acc.* 2000, *105*, 169-172.
31. Marshall, K. L., Painter, G. Lotito, K., Noto, A.G., Chang, P., *Mol. Cryst. Liq. Cryst.* 2006, *454*, 47[449] – 79 [481].

Dynamic Energy Grouping in Multigroup Radiation Transport Calculations

Nicholas Whiting

Dynamic Energy Grouping in Multigroup Radiation Transport Calculations

Nick Whiting

Bloomfield High School

Advisor: Dr. Reuben Epstein

University of Rochester

Laboratory for Laser Energetics

2006 Summer High School Research Program

Abstract

During an OMEGA inertial confinement fusion (ICF) implosion, some of the absorbed laser energy is reemitted by the shell of the target as thermal radiation. In order to simulate the radiative heating of the core of the target and other radiative effects, numerical models of radiation transport are included in ICF simulation codes. These models typically divide the radiation spectrum into many energy groups. Unfortunately, these simulations can take a long time to run if the radiation transport calculation is repeated for each of a large number (e.g. 40) of energy groups. A new strategy for reducing the number of groups has been evaluated using a simple radiation program. A common technique for reducing the time needed for the radiation simulation is to regroup a large number of energy groups into fewer, larger groups in a way that avoids too great a loss of precision. The novel feature of the new strategy is adjust the boundaries of these few energy groups automatically at regular time intervals, each time optimizing the resolution of the spectrum, thus improving the accuracy of the calculations without significantly lengthening the processing time. My program, based on an earlier version by Brian MacPherson,¹ has been used to develop and analyze this method for radiation transport test cases. I will show results demonstrating this method and how it can compensate for the inaccuracies due to the reduced spectral resolution of four-group calculations.

1-Introduction

The numerical simulation of hydrodynamics is very important at the Laboratory for Laser Energetics in designing ICF experiments and in testing our understanding of the outcomes of these experiments. At the moment, these simulations may take hours, or even days, to complete. This long simulation time stems from the complexity and number of the arithmetic operations that must be completed to simulate the hydrodynamics of laser-driven implosions, including the transport of radiation through the target material. These calculations involve collecting all possible photon energies ($h\nu$) into some number of intervals or “groups,” and perform the transport calculation on each of these groups. This number of groups is usually 48, 12, or 4 in the simulations used at LLE. The accuracy and time required for calculation are directly related to each other. The time required in this simulation can be reduced by regrouping those photon energy groups into a smaller number of groups.

This project worked with a model problem in which a 1 keV blackbody spectrum was incident on a planar slab of material. The time evolution of the temperature profile in the slab, which depends on radiation transport in the slab, was calculated. In the case of the program I worked with, we chose to use 40 intervals and 4 regrouped intervals of photon energy, which cut the time required to simulate the radiation transport by a significant amount (ideally, a factor of 10). Unfortunately, this time-saving measure loses accuracy when compared with its many-group counterpart due to the relative lack of spectral resolution. A proposed remedy for this inaccuracy is “dynamic regrouping,” in which this regrouping is repeated periodically over the course of the simulation so that the boundaries of the four energy groups change, adapting to the radiation spectral energy density at any given point in time. If this method works as intended, it would retain the time-efficiency of static regrouping while retaining much of the accuracy of the many-group calculations. In order to test this method, a program was written in 2005 by Brian MacPherson.¹ This program only took the method as far as “static regrouping,” where the same 4 groups are kept fixed throughout the calculation. I wrote a dynamic regrouping section of code into this program. I also addressed a number of problems associated with the length of the time steps, the calculation of the new groupings, and various other sections of the program. I processed my results using the PV Wave

Advantage programming environment.²

2-Method

2.1 Radiation Transport

In simulating radiation transport and demonstrating dynamic regrouping, the program must calculate numerous properties and radiative effects experienced by the material. The most important quantities are opacity κ_ν , emissivity ε_ν , intensity I_ν , radiation spectral energy density U_ν , and matter temperature T . All energy quantities, such as kT and $h\nu$ are expressed in units of keV.

2.1.1 Opacity

Opacity is the material property that determines the rate at which the material absorbs radiation. This may be dependent on a number of properties, such as the temperature, density, and composition of the material, and also on the frequency (or photon energy) of the incident radiation. In my program, I used simple opacity expressions chosen by Fleck and Cummings³ for their standard test problems. The opacity κ_ν is equal to:

$$\kappa_\nu = \frac{27(1 - e^{-h\nu/kT})}{[h\nu(\text{keV})]^3} \text{cm}^{-1}, \quad (1)$$

where $(1 - e^{-h\nu/kT})$ is a correction for stimulated emission. The subscript ν denotes photon frequency or energy dependence. In this equation, the opacity is inversely related to the cube of the photon energy, so higher-energy photons will penetrate farther into the slab. This opacity is not strongly temperature dependent, but I did work with a strongly temperature dependent opacity at one point,

$$\kappa_\nu = \frac{27(1 - e^{-h\nu/kT})}{[h\nu(\text{keV})]^3 [kT(\text{keV})]} \text{cm}^{-1}, \quad (2)$$

Here, the opacity is also inversely related to temperature kT . This program and these opacity expressions are needed only for the analysis of the dynamic regrouping method, and more complicated and quantitatively accurate representations of real material

opacities are not required.

2.1.2 Emissivity

Emissivity is the rate at which a material emits radiation. This rate is determined by the properties of the material (temperature, composition, and density). For my program, Kirchoff's law was used for the calculation of emissivity:

$$\varepsilon_{\nu} = \kappa_{\nu} B_{\nu}(T). \quad (3)$$

This equation relates emissivity ε_{ν} directly to opacity κ_{ν} by the Planck function of temperature $B_{\nu}(T)$. In this program, the Planck function is:

$$B_{\nu}(T) = 4\pi \frac{5.04 \times 10^{22} [h\nu(\text{keV})]^3}{(e^{h\nu/kT} - 1)} \frac{\text{erg}}{\text{cm}^2 \text{keV sec}}. \quad (4)$$

2.1.3 Intensity

As radiation travels through the slab, it is both absorbed and emitted. This produces an intensity I_{ν} of radiation, given by the equation of radiative transfer, where dI_{ν}/ds , the rate of change of I_{ν} with distance s along the propagation path, is:

$$\frac{dI_{\nu}}{ds} = \frac{\varepsilon_{\nu}}{4\pi} - \kappa_{\nu} I_{\nu}. \quad (5)$$

In its calculation of intensity, the program uses the solution to Eq.5 giving the intensity at any given distance s and for any given photon energy $h\nu$. The solution for a slab of uniform opacity κ_{ν} and emissivity ε_{ν} for the intensity $I_{\nu}(s)$ along a straight line path starting from $s=0$, where $I_{\nu}(0) = I_{\nu 0}$ is

$$I_{\nu}(s) = \frac{\varepsilon_{\nu}}{4\pi\kappa_{\nu}} + \left(I_{\nu 0} - \frac{\varepsilon_{\nu}}{4\pi\kappa_{\nu}} \right) e^{-\kappa_{\nu}s}. \quad (6)$$

2.1.4 Radiation Energy Density

The radiation spectral energy density is the spatial density of radiation energy within a unit range of photon energy at some distance s into the slab. The

radiation spectral energy density is given by:

$$U_\nu(s) = 2\pi \int_{-1}^1 I_\nu(s) d(\cos\theta). \quad (7)$$

In this equation, the intensity values are integrated over all path angles θ , where θ specifies the photon path direction relative to the slab normal direction $\theta = 0$. This is to account for radiation being emitted in all directions. The intensity is independent of the azimuthal angle ϕ due to the planar symmetry of the problem. In calculating the intensity over the full 180° range of θ , the program splits 180° into 16 segments of equal solid angle. The radiation energy density is of particular importance in calculating and understanding the matter temperature results.

2.1.5 Matter Temperature

The evolution of the matter temperature is dependent on the rate of energy absorption determined by the opacity κ_ν , the cooling rate determined by the emissivity ε_ν , and the intensity I_ν of the radiation at that distance into the slab:

$$C_V \frac{dT}{dt} = \iint \kappa_\nu I_\nu d\Omega d(h\nu) - \int \varepsilon_\nu d(h\nu). \quad (8)$$

Here, C_V is the specific heat of the material that is being simulated. In the test problems, it is a constant set to $C_V = 0.5917aT_0^3$, where a is the radiation energy density constant, $a = 1.37 \times 10^{14} \frac{\text{erg}}{\text{cm}^3 \text{keV}^4}$. The matter temperature equation gives two important terms: the absorption rate and the emission rate. The absorption rate is given by the opacity multiplied by the intensity $\kappa_\nu I_\nu$ integrated over all angles $\int d\Omega = 2\pi \int d(\cos\theta)$ and over all photon energy values $\int d(h\nu)$. The emission rate is the emissivity of the material ε_ν integrated over all photon energy values $h\nu$. These values are used to find the matter temperature after a finite time step Δt :

$$T = \frac{T_0 \left[C_V T_0 + \iint \kappa_\nu I_\nu d\Omega d(h\nu) \Delta t + (\alpha - 1) \int \varepsilon_\nu d(h\nu) \Delta t \right]}{C_V T_0 + \alpha \int \varepsilon_\nu d(h\nu) \Delta t}. \quad (9)$$

Eq.9 expresses the temperature T at the end of the time step as an “explicit,” “implicit,” or intermediate solution of Eq.8, depending on the value of the parameter α being 0, 1, or an intermediate value.³ When Eq.8 is solved explicitly ($\alpha = 0$) for T , the T -dependent terms on the right-hand side of Eq.8 are first written entirely in terms of the initial T value, T_0 . The implicit solution ($\alpha = 1$) is the opposite, in the sense that the right-hand side of Eq.8 is first written in terms of the final value of T , which is T itself. The implicit formulation of Eq.8, expressed as Eq.9 with $\alpha = 1$, is used by the program to determine the matter temperature.

2.2 Existing Simulation

At the Laboratory for Laser Energetics, two main hydrocodes are used. These are the DRACO (2D hydrodynamics modeling) and LILAC (1D hydrodynamics modeling) codes. These codes can calculate radiation transport by grouping all photon energy values into a relatively large number of groups in order to preserve accuracy. This entails a large number of calculations and is extremely time consuming. In handling the angle-dependent aspect of radiation transport, the hydrocodes almost always use the diffusion approximation, a more approximate method than we used in this program. Some effort has been taken to shorten the time needed for these simulations to run by gathering photon energy values into a smaller number of groups, but no automated dynamic regrouping strategy has yet been implemented. These simulations are needed for the researchers at the lab to simulate ICF implosions in order to better design experiments. Reducing the amount of time necessary to run a simulation without losing a significant amount of precision would prove extremely valuable to the researchers at the LLE.

2.3 Static Regrouping

Static regrouping was implemented by consolidating a large number of small groups into a smaller number of larger groups that remain fixed throughout the calculation. In my work, I used a test problem of Fleck and Cummings where a 4 cm-thick slab is irradiated by a 1-keV blackbody spectrum. Figure 1 is a contour plot of the spectral energy density of the slab of material at 50 ps (20 time steps). This is the point at which the photon energy groups are first recalculated. Before this, the values are collected into 40 photon energy groups, each of which was 0.25 keV wide. Then, these

groups are regrouped into 4 groups. The boundaries of these new groups are shown in Fig. 1 as horizontal lines. After this, the calculation continues, using only these 4 groups. An inaccuracy in the spectral energy density is caused by the relatively poor spectral resolution resulting from using only 4 groups. The inaccuracy produced by the regrouping remains throughout the course of the calculation and builds upon itself. The time at which the many-group calculation is converted to the few-group calculation also has a significant impact on the accuracy of the calculation. Also, the program represents conditions at a finite number of distances into the slab. The slab is divided into 10 finite distance intervals, as is done in the Fleck-Cummings test problems,³ giving only quantities defined at ten spatial points throughout the slab. The program uses finite difference integrations in time, distance, angle, and energy to handle these calculations.

2.4 Dynamic Regrouping

Dynamic regrouping was suggested^{4,1} as a possible solution to the difficulties presented by static regrouping. This method involves the successive recalculation of the boundaries of the four large groups at regular time intervals. This regrouping is repeated periodically using spectral energy density values calculated with the same 40 groups used in determining where the boundaries of the four large groups were to be placed in the first regrouping. The simulation then continues for the following predetermined cycling time interval using only the four new groups. Once the cycling time has expired, the simulation goes on to perform yet another 40-group time step to produce a smooth spectrum with a smoothness similar to that of the spectral energy density shown earlier in Fig. 1. Then, a new set of 4-group boundaries is obtained from the smooth 40-group spectral energy density, and the program cycles again. All of this is done automatically by the program. Overall, this method of simulation improves upon the approximation of a low-resolution 4-group spectral grid without adding a significant amount of calculation time.

The contour plots of radiation spectral energy density produced during the simulation provide a good illustration of dynamic regrouping. Originally, the spectral energy density is smooth and accurate (Fig. 1). The contours of the 4-group spectrum can be seen from the contour plots produced during the 4-group calculations, such as Fig. 2 and Fig. 3. These spectra are seen to be very approximate, due to the relatively poor

spectral resolution, compared with the smoothness of the spectra produced early in the simulation. Figure 4 is an example of a spectral energy density produced from a 40-group calculation later in the simulation (447.5 ps). This plot illustrates the point in the dynamic regrouping cycle when the simulation returns to a more accurate representation of the spectral energy density for one time step in order to allow new group boundaries to be obtained for the 4-group time steps to be done next. This is the key detail in the dynamic regrouping cycle.

2.5 The Program

Dynamic regrouping has been incorporated into the radiation transfer program originally written by Brian MacPherson.¹ This program consists primarily of a time-stepping loop where the length of the time step is controlled. In each time step, the opacity and the emissivity are calculated for each of the 10 slab spatial zones. Then, the program obtains the intensity by numerically integrating Eq.5 and then uses Eq.7 to obtain the radiation energy density. The program goes on to calculate the change in matter temperature with Eq.9, which is the solution to Eq.8. At the regrouping time, new boundaries are calculated for the four large energy groups. Then, the program repeats this process in the next regrouping cycle.

2.5.1 Opacity and Emissivity Calculations

The program uses Eq.1 and Eq.3 to calculate the opacity and emissivity, respectively. Equation 2 was also used as an alternative temperature-dependent opacity in another Fleck-Cummings test problem.³ The opacity and emissivity functions are evaluated at each increment of distance into the material and at each of the 40 photon energy values. These stored values are used later in the calculation of intensity and in the calculation of the matter temperature. The emissivity and opacity are recalculated at every time step.

2.5.2 Intensity and Radiation Energy Density

The program first calculates the intensity values at all distances s along each of the 8 paths spaced equally in solid-angle intervals from 0° to 90° , relative to the forward direction ($\theta=0^\circ$), away from the blackbody source, and for each photon energy value.

These integrations are initialized with $I_{\nu 0}$ equal to the blackbody spectrum at $T = 1$ keV. The program uses Eq.6 to perform the integration along s . The final intensity at the end of each distance increment is used to evaluate the contribution to the absorption rate term in Eq.9 for each distance step, for each photon energy, and for each angle. This calculation is also performed in an identical fashion for the intensities along the remaining 8 paths from 90° to 180° , except that each of these rays are initialized with $I_{\nu 0} = 0$ at the outer boundary. All these values of intensity are then used to determine the radiation spectral energy density using Eq.7. These values of radiation energy density can then be displayed in contour plots so that the radiation energy density can be compared at different points in time. Figure 1 and Fig. 4 show plots of radiation energy density at two different points in time. It can be seen that early in the simulation, higher energy photons penetrate deeper into the material, but that later in the simulation the distribution of low and high energy photons deep in the material is more even.

2.5.3 Matter Temperature

The matter temperature evolution is obtained from Eq.8 after calculating the radiation absorption and emission rates. The opacity is multiplied by intensity and integrated over all angles and all photon energies to give the absorption rate. The emissivity is integrated over all photon energies to give the emission rate. The absorption and emission rates are used in Eq.9 to find the matter temperature. The program solves this equation implicitly, setting α equal to 1. Figure 5 is plotted with respect to distance into the slab at one specific time (750 ps) in the simulation. Figure 6 is the temperature at one distance into the slab (1.2 cm) over the entire time that the slab is exposed to the incident 1 keV blackbody spectrum.

2.5.4 Regrouping

Regrouping is performed automatically after a certain number of time steps. This number can be set to any value, but I chose to have it perform the first regrouping after 20 time steps (50 ps), and then regroup at intervals of 40 time steps (100 ps). In the calculation of the new 4-group boundaries, the program uses the 40-group radiation spectral energy density and places one boundary at the maximum of the spectral energy density integrated over the whole volume, one boundary at each of the 50%-maximum

value points, and one boundary each at the lowest and highest photon energy values. This regrouping reduces the number of calculations performed, but it also creates radiation energy density contour plots that are more approximate due to the loss of spectral resolution.

3-Results

3.1 Dynamic Regrouping vs. Static Regrouping

In the first 60 time steps (150 ps), through the end of the first dynamic regrouping cycle, the dynamic and static regrouping results are the same, since both methods use the same 4 groups during this time. Figure 6 shows this with the 40-group calculation as a solid line, dynamic regrouping as a heavy-dotted line, and static regrouping as a light-dotted line. The dynamic regrouping result deviates from the static regrouping result after the 60th time step (150 ps). Immediately after this time step, the dynamic regrouping performs a single 40-group calculation of the radiation spectral energy density to use in determining a new set of 4-group boundaries. Since these 4 new groups allow better resolution of the spectrum at this point in time, the temperature results begin to more closely follow the results of a full 40-group calculation. This improvement is very slight and is not clearly visible in Fig. 6 at this depth (1.2 cm) until after the next regrouping cycle at the 100th step (250 ps). Figure 7 also illustrates these results, showing the effects of dynamic regrouping on the temperature deeper (2.7 cm) into the slab. Here, the dynamic regrouping results deviate visibly toward the 40-group results after the second regrouping at the 60th time step (150 ps). This simulation also has produced temperature profiles that are similar to those that were obtained in test problems by Fleck and Cummings.³ Figure 5 is a good example of these temperature profiles, and again shows improvement over static regrouping when dynamic regrouping is used. This improvement is probably the most important result of my work.

3.2 Time step Variation

The size of the time step also had some effect on the accuracy of both static and dynamic regrouping. If the time step was too large, the temperature profile errors at early times could be excessive, as is illustrated by the example in Fig. 8. As the time step comes closer and closer to zero, the accuracy of the results increases because the

difference equation becomes a better approximation of the differential equation. Figure 9 shows the accuracy produced by using a time step that is fairly small. Unfortunately, with a significantly smaller time step, the time required to run the program increases by a factor that is inversely related to that time step. I had to choose a time step that was small enough to produce relatively accurate results, but that did not require an especially large amount of time to compute. After experimenting with a few other values, I chose a 2.5 ps time step as the most efficient. As can be seen from Figure 10, this time step still provides improved accuracy over static regrouping, while at the same time not being too small to undo the efficiencies gained by using regrouping. With any significant change to the test-case problem (such as adding strongly temperature-dependent opacity), the size of the time step may have to be adjusted to maintain accuracy. For example, a strongly temperature-dependent opacity can greatly increase the heating rate, causing the matter temperature values to jump up to many times the 1 keV source radiation temperature if the time step is too large, which is physically impossible. In order to run the calculation for the same amount of simulated time, the number of time steps increases, and the computation time begins to become a problem once more. A different method of calculation may allow for a larger time step to be taken, but at present, the time step has a very large effect on the accuracy (and so, the usefulness) of dynamic regrouping.

3.3 Boundary Variation

In the regrouping process, boundary values for the larger energy groupings are chosen based on a calculation of the space-integrated spectral energy density. Boundaries are placed at the highest and lowest photon energy values (10.0 keV and 0.25 keV in the case of this program). A boundary is also placed at the photon energy with the highest spectral energy density. Then, two more boundaries are placed, each at the photon energies with 50% of the maximum radiation energy density. This percentage was chosen because it would distribute the energy in the groupings fairly evenly. However, I experimented with varying this percentage, and found that different percentages produced results with different accuracy. I determined this by comparing the temperature profiles produced by static and dynamic regrouping with these percentage changes to a full 40-group calculation and to the profiles produced by the default 50%

calculations (Fig.7). I raised the boundaries to 60% of the maximum, and found that static regrouping lost accuracy (Fig.11), but that dynamic regrouping regained a small amount of accuracy. I also lowered the boundaries to 40% of the maximum and found that static regrouping gained accuracy and followed dynamic regrouping more closely. Experimentation with the boundary selection strategy appears to benefit both the static and dynamic regrouping results to some degree. The boundary calculations in this regrouping strategy must be analyzed in more detail before any definite conclusions can be drawn from the results, but, at the moment, this seems to be a step in the right direction.

4-Conclusions/Future Work

In researching dynamic regrouping as an effective method for accurately and efficiently simulating radiation transfer, I have found that the dynamic regrouping retains the efficiency of static regrouping while, at the same time, more closely follows the results of a full 40-group calculation. A nearly ten-fold improvement in time efficiency was observed, as well as the improvement of accuracy, over that of static regrouping. I have also found that adjusting the regrouping method affects the accuracy of results produced by this program. By continuing to experiment with this strategy, the accuracy of dynamic regrouping may be further improved. Among the adjustable aspects are the time step length and the group boundary selection method. The time step appears to have the greatest effect on the results obtained. If it is too small, efficiency is lost, but if it is too big, accuracy is lost. The boundary calculations have a less drastic affect on the accuracy of dynamic regrouping, but they appear to have a larger effect on the accuracy of static regrouping. During further testing, this method will have to be exposed to many more test problems to determine its potential benefits or limitations. At present, dynamic regrouping has only been tested against one test problem. However, with much work remaining to be done, dynamic regrouping still appears to be a promising method of improving the efficiency of radiation transfer simulations.

5-References

- [1] Brian MacPherson, "Dynamic Energy Grouping in Multigroup Radiation Transport Calculations," 2005 Summer Research Program for High School

Juniors, Student Research Reports LLE Laboratory Report #343.

[2] PV-Wave Advantage Programming Environment

[3] J. A. Fleck, Jr. and J. D. Cummings, “An implicit Monte Carlo scheme for calculating time and frequency dependent nonlinear radiation transport,” *Journal of Computational Physics*, vol. 8, pp. 313-342, 1971.

[4] R. Epstein, private communication, Jul-Aug. 2006.

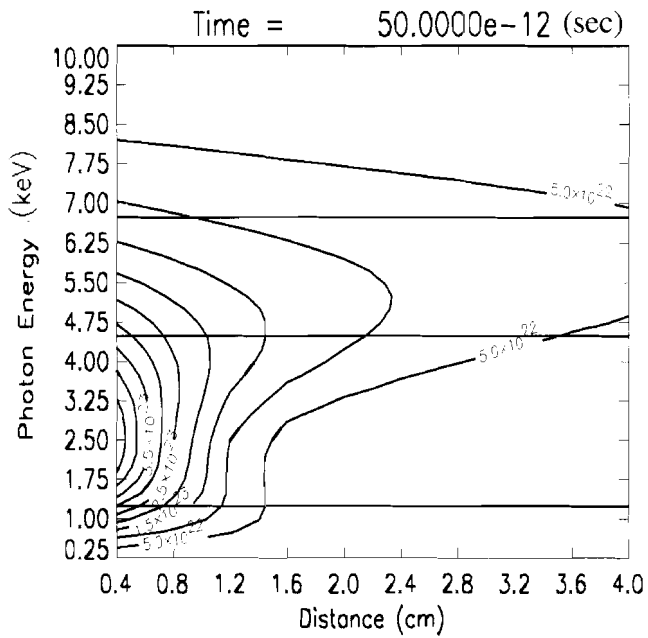


Fig.1: Contour plot of the radiation spectral energy density as a function of distance into the slab and photon energy using 40 energy groups. The boundaries selected for the 4-group calculation in Fig.2 are shown as horizontal lines.

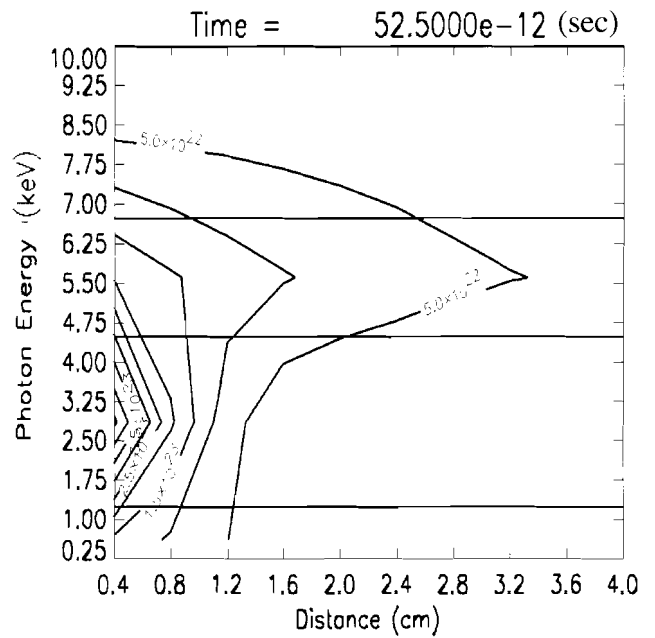


Fig.2: Same as Fig.1, except that the radiation spectral energy density is calculated using only 4 groups.

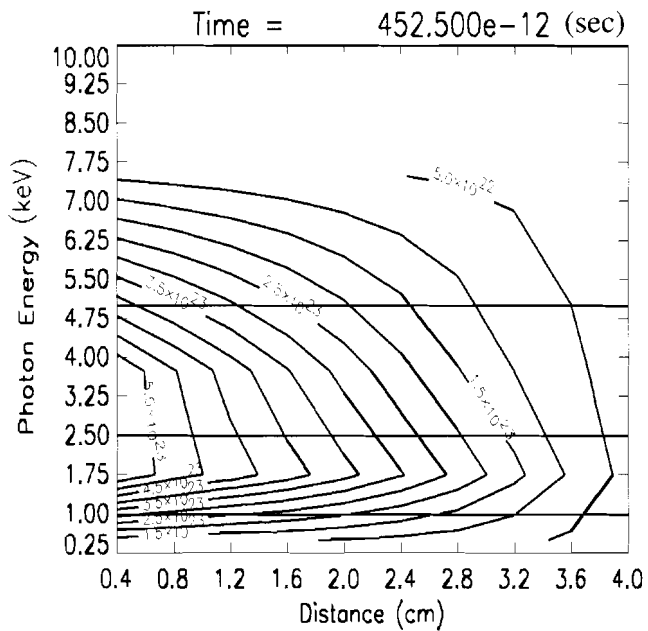


Fig.3: Same as Fig.2, but 160 time steps (400 ps) later.

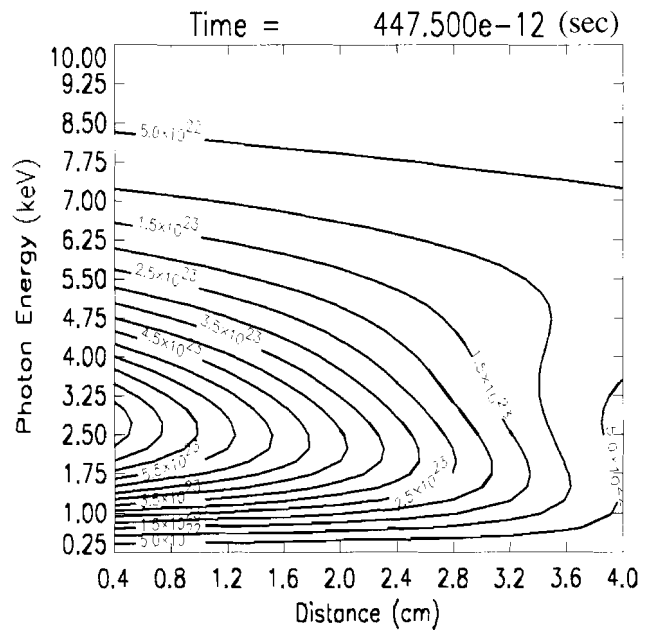


Fig.4: Same as Fig.1, but 159 time steps (397.5 ps) later when the smoother 40-group spectrum is obtained. This plot shows the deeper penetration of lower energy photons than at earlier times in the simulation, such as is shown in Fig. 1.

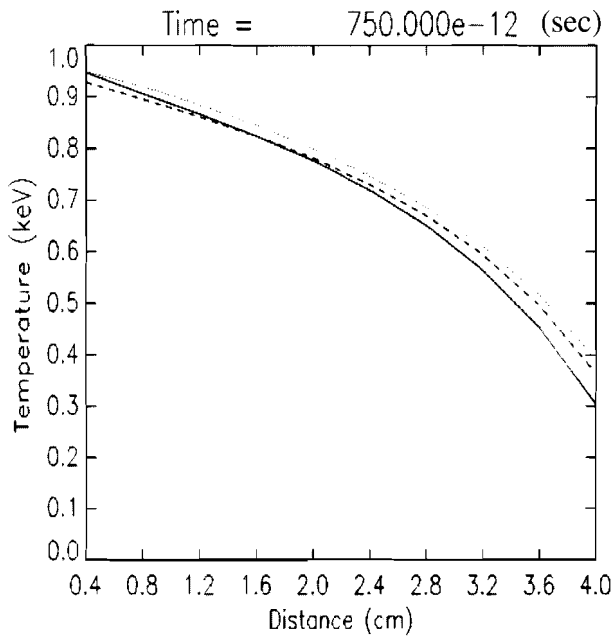


Fig.5: Matter temperature profiles similar to those produced by Fleck and Cummings.³ A full 40-group calculation is represented by the solid line. Static regrouping is the dotted line, and dynamic regrouping is the dashed line.

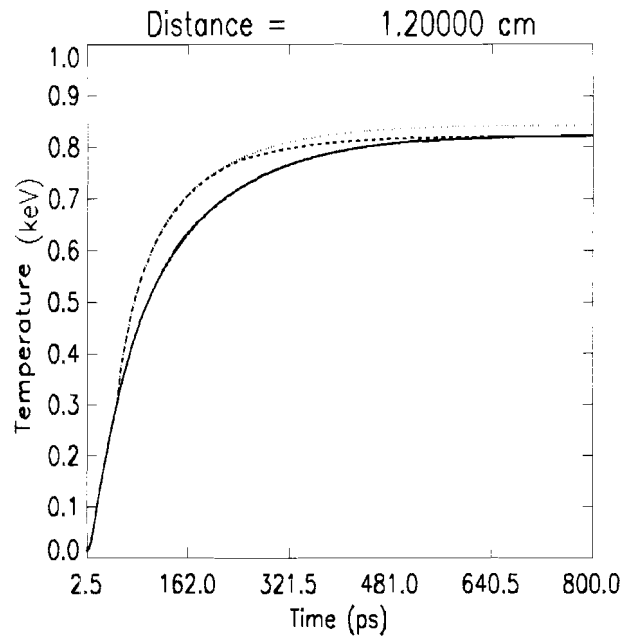


Fig.6: Matter temperature profile in a single zone (at a distance 1.2 cm) with respect to time. The solid line is a 40-group calculation, the dashed line is dynamically regrouped, and the dotted line is static regrouping.

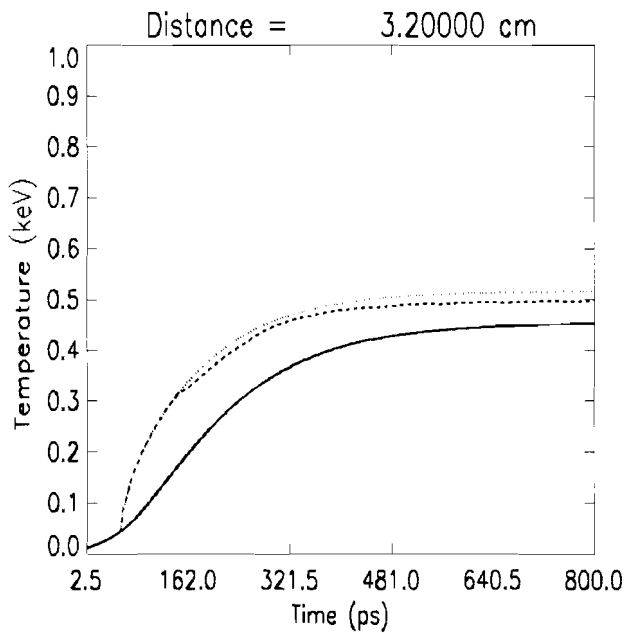


Fig.7: Same as Fig.6, but at a zone that is 3.2 cm into the slab of material. The photon energy boundaries are at 50% of the maximum photon energy density value for this calculation.

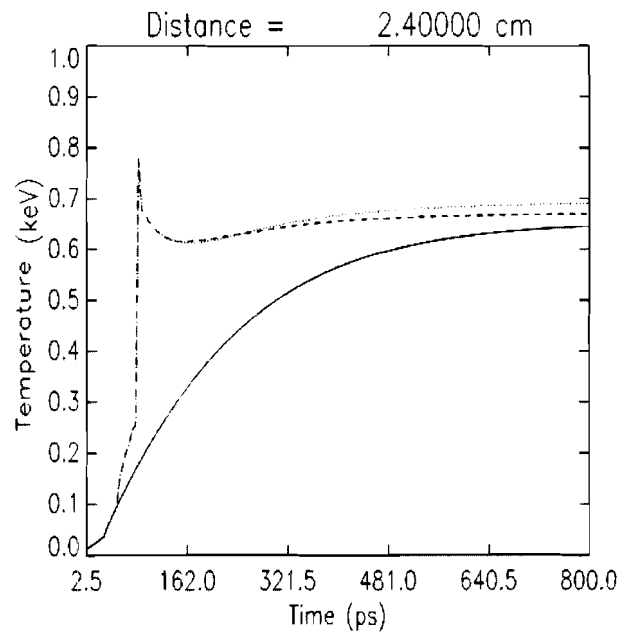


Fig.8: Same temperature history as shown in Fig.7, but at a zone 2.4 cm into the slab and calculated using a 5.0 ps time step.

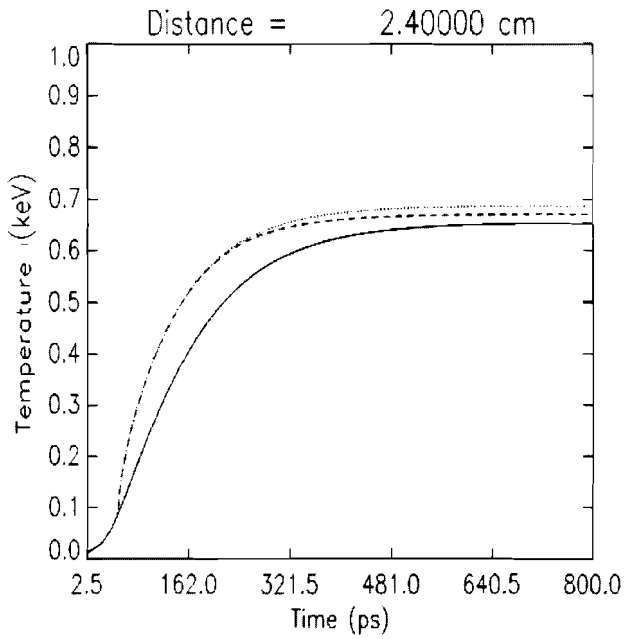


Fig.9: Same as Fig.8, but calculated with a 1.25 ps time step.

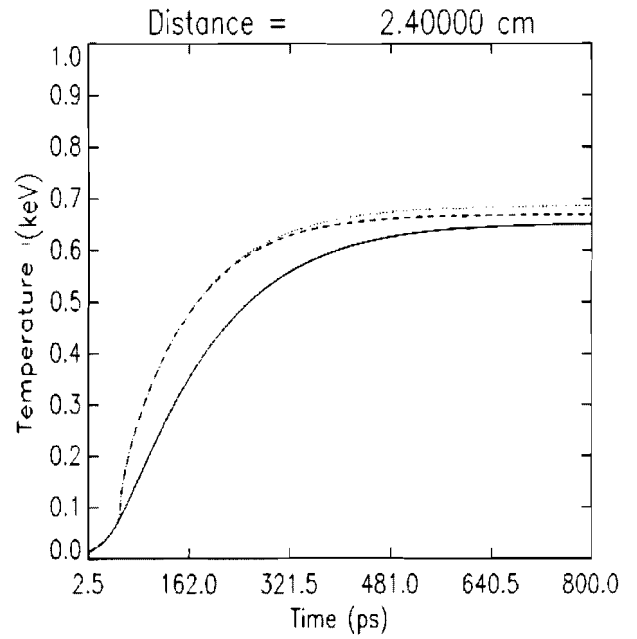


Fig.10: Same as Fig.8, but calculated using a 2.5 ps time step.

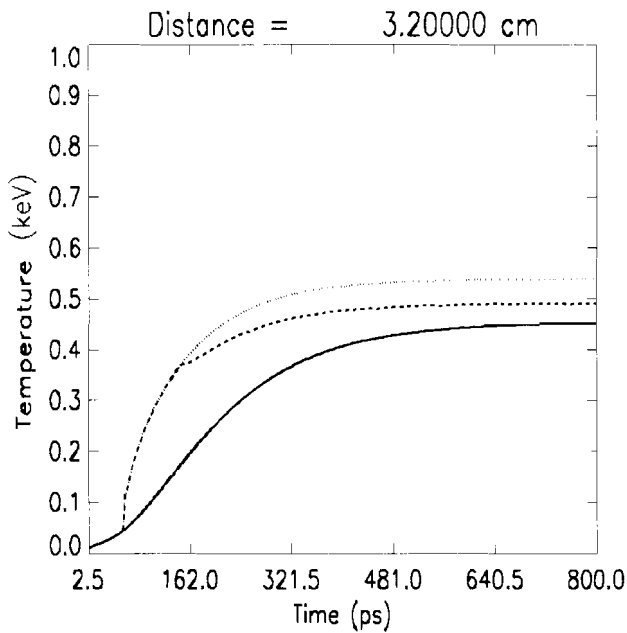


Fig.11: Same as Fig.7, except the photon energy boundaries were set at 60% of maximum photon energy density value for this calculation.

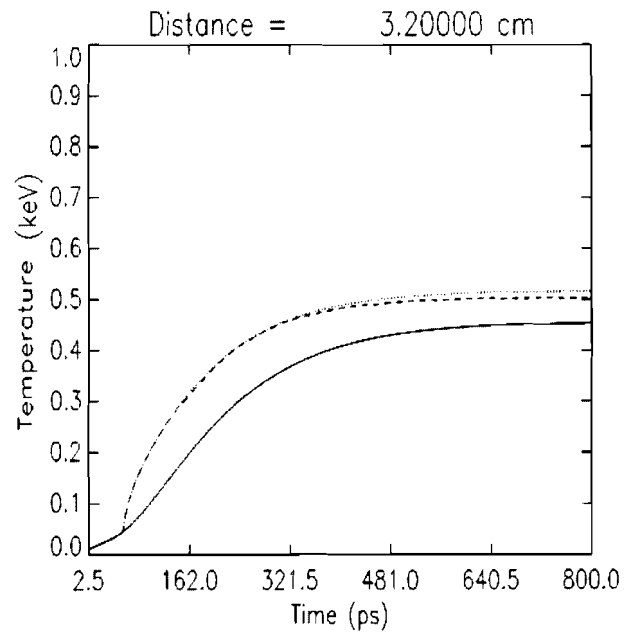


Fig.12: Same as Fig. 7, but the photon energy boundaries were set at 40% of maximum photon energy density value for this calculation.